

Laser manipulation of metastable neon by isotropic light

Citation for published version (APA):

Aardema, T. G. (1995). *Laser manipulation of metastable neon by isotropic light*. [Phd Thesis 1 (Research TU/e / Graduation TU/e), Applied Physics and Science Education]. Technische Universiteit Eindhoven.
<https://doi.org/10.6100/IR438425>

DOI:

[10.6100/IR438425](https://doi.org/10.6100/IR438425)

Document status and date:

Published: 01/01/1995

Document Version:

Publisher's PDF, also known as Version of Record (includes final page, issue and volume numbers)

Please check the document version of this publication:

- A submitted manuscript is the version of the article upon submission and before peer-review. There can be important differences between the submitted version and the official published version of record. People interested in the research are advised to contact the author for the final version of the publication, or visit the DOI to the publisher's website.
- The final author version and the galley proof are versions of the publication after peer review.
- The final published version features the final layout of the paper including the volume, issue and page numbers.

[Link to publication](#)

General rights

Copyright and moral rights for the publications made accessible in the public portal are retained by the authors and/or other copyright owners and it is a condition of accessing publications that users recognise and abide by the legal requirements associated with these rights.

- Users may download and print one copy of any publication from the public portal for the purpose of private study or research.
- You may not further distribute the material or use it for any profit-making activity or commercial gain
- You may freely distribute the URL identifying the publication in the public portal.

If the publication is distributed under the terms of Article 25fa of the Dutch Copyright Act, indicated by the "Taverne" license above, please follow below link for the End User Agreement:

www.tue.nl/taverne

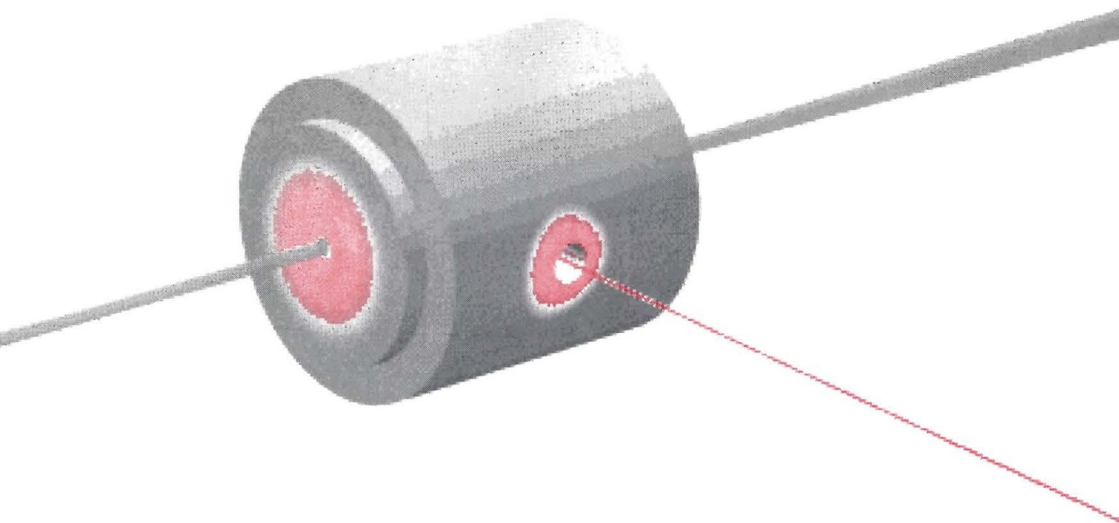
Take down policy

If you believe that this document breaches copyright please contact us at:

openaccess@tue.nl

providing details and we will investigate your claim.

Laser Manipulation of Metastable Neon by Isotropic Light



T.G. Aardema

LASER MANIPULATION OF METASTABLE NEON
BY ISOTROPIC LIGHT

PROEFSCHRIFT

TER VERKRIJGING VAN DE GRAAD VAN DOCTOR AAN
DE TECHNISCHE UNIVERSITEIT EINDHOVEN, OP GEZAG
VAN DE RECTOR MAGNIFICUS, PROF.DR. J.H. VAN LINT,
VOOR EEN COMMISSIE AANGEWEEZEN DOOR HET COLLEGE
VAN DEKANEN IN HET OPENBAAR TE VERDEDIGEN OP
DINSDAG 20 JUNI 1995 OM 14.00 UUR

DOOR

TABE GEERT AARDEMA

GEBOREN TE EINDHOVEN



DIT PROEFSCHRIFT IS GOEDGEKEURD
DOOR DE PROMOTOREN
PROF.DR. H.C.W. BEIJERINCK
EN
PROF.DR.IR. H.L. HAGEDOORN

COPROMOTOR:
DR.IR. J.P.J. DRIESSEN

The work described in this thesis was carried out at the Physics Department of the Eindhoven University of Technology and has been supported by the Foundation for Fundamental Research on Matter (FOM)

Contents

I	Introduction	3
1	Laser manipulation of atomic beams	4
2	Atomic state preparation	5
3	Laser cooling: velocity manipulation	6
	3.1 Slowing techniques	7
	3.2 Diffusely reflecting cavities	8
4	This thesis	10
II	Isotropic light slowing of $\text{Ne}^*(^3\text{P}_2)$ atoms: cavity design and applications	13
1	Introduction	14
2	Slowing by isotropic light	16
3	Isotropic light cavity	17
	3.1 Wall reflection density $W(z)$	17
	3.2 Spectral density $\mathcal{U}(\omega)$	19
4	Monte Carlo simulation of $W(z)$	21
	4.1 Geometry dependence of the reflectance	21
5	Monte Carlo simulation of slowing	22
	5.1 Numerical implementation	24
6	Axial slowing and diffusion	26
7	Transverse diffusion	29
8	Comparison of experiment and simulation	31
9	Spherical cavity	33
10	Post-Zeeman slower	36
11	Concluding remarks	39
III	Transverse diffusion in isotropic light [submitted to Phys. Rev. Lett.]	43
IV	Slowing of $\text{Ne}^*(^3\text{P}_2)$ in Spectralon cavities: experiments	55
1	Introduction	56
2	Isotropic slowing	58
3	Experimental setup	59
	3.1 Beam machine	59
	3.2 Isotropic light cavity	60

3.3	Laser equipment	63
4	Position-dependent detector	63
4.1	Hardware	63
4.2	Measuring routine	64
4.3	Beam measurements	64
5	Cylindrical cavity	66
5.1	Varying the laser power P	66
5.2	Varying the resonance velocity v_6	69
5.3	Simulated TOF distribution	71
5.4	Transverse diffusion exclusively, $\delta = 0$	73
6	Spherical cavity	74
7	Multiple cavities	76
8	Special features	79
8.1	Multiple frequency slowing	79
8.2	Acceleration	81
9	Concluding remarks	82
V Excitation transfer for $\text{Xe}^*(^3\text{P}_2) + \text{N}_2$ in the eV energy range: double potential crossing for $\text{N}_2(\text{B}, v^2=5)$ [Chem. Phys. 184, 273 (1994)]		85
1	Introduction	86
2	Experimental	86
3	Experimental cross sections	87
4	Multiple curve crossings	91
5	Analysis of cross section	94
6	Concluding remarks	98
VI Excitation transfer of $\text{Kr}\{4p^55p; ^3\text{D}_3\}$ in collisions with N_2 molecules		101
1	Introduction	102
2	Experimental setup	104
2.1	Crossed beam apparatus	104
2.2	Laser excitation	105
3	Results and data analysis	108
4	Model analysis	110
5	Concluding remarks	115
Summary		119
Samenvatting		121
Dankwoord		124
Curriculum vitae		124

Chapter I

Introduction

1 Laser manipulation of atomic beams

The field of Atomic Physics has evolved tremendously over the last two decades since laser systems have become a common commodity. Thus far, the major impact has been the opportunity to prepare atoms in specific excited states. By using one or multiple laser beams, a single electron can be promoted to higher levels (up to the Rydberg levels) or the atom can even be ionized. Exciting two or more electrons simultaneously results in yet more possible excited states, even auto-ionizing states. The field of atomic spectroscopy studies state-specific features of these excited states such as lifetimes, energy levels, and level splittings. The results are used to test quantum mechanical models of the coupling schemes of the orbital and spin angular momenta of the electrons and the nucleus. In the field of atomic collisions, the preparation of these laser-excited species in crossed-beam apparatuses enables the study of inelastic and reactive collisions, which play an important role in plasmas and gas discharges [1, 2, 3].

Currently, the field of Atomic Physics is subject to a yet more drastic change. Laser cooling techniques enable experimentalists to control and manipulate the velocity of neutral atoms, which cannot be affected by electro-magnetic forces. Since the demonstration of slowing an atomic beam within a distance of one meter and capturing and cooling atoms in a trap [4], research in the field of Laser and Atomic Physics literally exploded. The number of available techniques to manipulate atomic beams is growing steadily. It is now possible to study atomic collisions in atomic traps at much lower collision energies. Crossed-beam apparatuses are being constructed employing 'laser-cooled' atomic beams. In these pioneering collision experiments it will be possible to vary the collision energy from the classical thermal regime (K) to the cold (mK) and ultra-cold (μ K) regime. The quantum mechanical 'deBroglie' wave length, $\lambda = \hbar/mv$, which characterizes the size of the atomic wave packets, becomes comparable to the typical interaction ranges ($\approx 10a_0$) at these lower collision energies.

This thesis deals with atomic beam experiments which employ the above mentioned laser manipulation techniques: atomic state preparation and laser cooling. A substantial part of the work concerns basic research into a novel technique for axial slowing of an atomic beam. The remaining part of the thesis covers experimental work focussing on the electronic and rovibrational energy transfer in $\text{Xe}^* + \text{N}_2$ and $\text{Kr}^{**} + \text{N}_2$ collisions in the thermal collision-energy range. In these traditional collision experiments electronically excited rare gas states [$\text{Kr}\{(4p)^55s\}$, $\text{Kr}\{(4p)^55p\}$, $\text{Xe}\{(5p)^56s\}$] are prepared (or modulated) by laser excitation.

2 Atomic state preparation

The interaction of a resonant laser beam with an atom can result in absorption or stimulated emission of a photon. In case of absorption, an electron is promoted to a higher orbital state, whereas a lower state is reached in case of stimulated emission. Laser excited rare-gas atoms decay spontaneously by emitting a photon in a random direction after a short lifetime (typically tens of nanoseconds). In Fig. 1 the energy level diagram for the neon atom is given as an example for the rare-gas atoms. Two

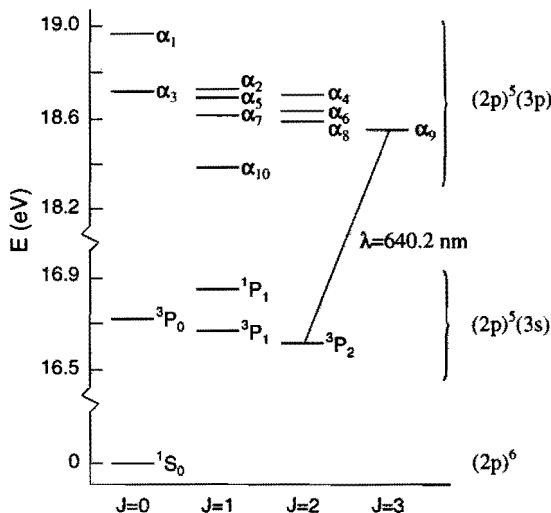


Figure 1: Energy-level diagram of the $\text{Ne}^*\{(2p)^53s\}$ (Russell-Saunders notation) and $\text{Ne}^{**}\{(2p)^53p\}$ (Paschen numbering) excited states, grouped by their electronic angular momentum quantum number J . The closed two-level transition at $\lambda = 640$ nm employed for laser excitation has been indicated.

levels ($3P_0$ and $3P_2$) can be distinguished in the $\text{Ne}\{(2p)^53s\}$ multiplet which have weak decay transitions to the ground-state (electric dipole forbidden). The resulting long lifetimes ($\tau > 1s$) enable atomic beam experiments with these so-called metastable states, which can be produced in discharge-excited beam sources. In a crossed-beam setup one can study inelastic and reactive collisions of atoms in these states. In such experiments, laser beams have been used to deplete one metastable level and to obtain state-dependent collision information with modulation techniques. Moreover, tuning the laser frequency into resonance with different isotopes makes it possible to extract isotopic dependencies of the collision process [5].

Apart from using the laser beam as a modulator for populating levels, it can also be used for exploring collision processes of the laser-excited states. For this purpose, the laser photons need to be absorbed at the intersection of the two atomic beams. To ensure collisional interaction within the short lifetime of the laser-excited states, high beam densities are required. Furthermore, it is possible to control the shape of the wave function of the excited state through the laser polarization vector. Thus,

alignment and orientation dependencies of atomic interaction processes can be studied by varying the laser polarization with respect to the relative velocity vector.

Over the last 20 years the application of laser excitation in Atomic Physics has grown immensely. Nowadays one can study atomic collisions in almost ultimate detail. Through time-of-flight techniques the energy dependence can be resolved. Using more resonant photons (or laser beams) can lead to the preparation of arbitrary atomic states; *e.g.*, collision experiments with Rydberg atoms are being performed as a function of principal quantum number 'n' [6, 7]. It is even possible to probe the scattered states with additional laser beams. And finally, with femto-second laser pulses the time evolution of a collision process can be monitored giving more or less 'real-time' collision dynamics.

3 Laser cooling: velocity manipulation

In sharp contrast with the precise control to prepare certain atomic states is the lack of control over the geometric characteristics of an atomic beam (deflection, compression, velocity). Neutral atomic species are not affected by electromagnetic forces, and for a long time there was no tool to manipulate these atoms. Resonant laser light, however, can exert a large force on neutral atoms. Over the past decade research into the fundamental aspects of these so-called laser cooling processes has grown immensely. Now that many of the basic aspects are known, there is an increasing interest in developing applications for these laser cooling techniques.

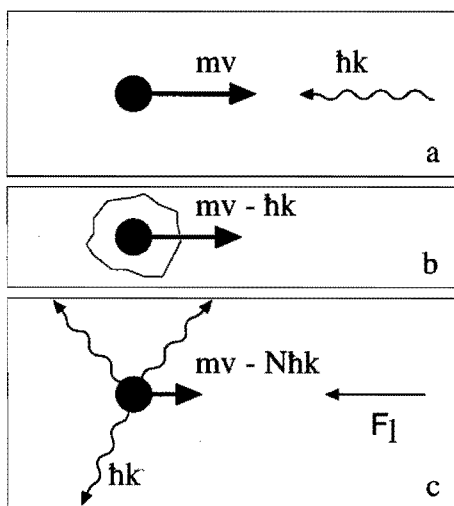


Figure 2: An atom which is excited by a photon will also absorb the photon momentum $\hbar k$ (panel a). The atom will decelerate if the photons come from the opposite direction (panel b). The atom can return to the lower level by spontaneous emission of a photon. In this case the atom experiences another recoil $\hbar k$, but in a random direction. The spontaneous photon recoils average out to zero over several of these cycles, whereas the absorption recoils do not. The net result is a resonant light force F_l in the direction of the laser beam (panel c).

The nature of resonant light forces is illustrated in Fig. 2. When an atom that is initially not moving absorbs a photon from a well-defined laser beam, it will be excited

from the ground state to the excited state. Simultaneously, it absorbs the photon momentum $\hbar k$, with k the wave vector. Accordingly, the atom gains a velocity $\hbar k/m$ in the direction of the laser beam, with m the mass of the atom. When, after some time, the atom emits a photon spontaneously in a random direction, the atom again receives a momentum recoil. If this process is repeated several times for this two-level system, the spontaneous photon recoils will average to zero. Therefore, the atom will gain momentum in the direction of the laser beam due to the absorption. Apart from spontaneous emission, the upper level can decay by stimulated emission. In contrast to the absorption-spontaneous emission cycle, the momentum changes of the atom cancel in the case of an absorption-stimulated emission cycle. Therefore, stimulated emission can be neglected in conventional laser cooling techniques.

The maximum force that can be exerted on the atom is $F = \hbar k \Gamma / 2$, with Γ the decay rate of the atom in the excited state. For $\text{Ne}\{(2p)^5 3p, {}^3D_3 = \alpha_9\}$, with atomic mass $m=20$ a.m.u. and $\Gamma=8.2$ (2π) MHz, this results in an acceleration of $a = F/m = 1.3 \cdot 10^5 \text{ ms}^{-2}$. This large acceleration enables manipulation of atomic beams into so-called 'bright beams', with an increase in beam density n (or beam flux $n \cdot v$) by a factor 10^3 to 10^4 . The rate at which collisions take place (proportional to n^2) increases by a factor 10^6 up to 10^8 , thus a measuring time of 4 years is reduced into a range of 1 to 100 second [8].

An excellent introduction to laser cooling aspects is given by Aspect et al. [9], providing an overview of the present work on laser cooling. The fields of Atom Optics, Quantum Optics, and Atom Physics are now open to many new experiments which may entail a more detailed picture of collision processes through improved signal-to-noise ratios, more precise atomic clocks, atomic lattices, and collisions between cold atoms. Especially in view of this last prospect, there is a growing desire to be able to control atomic beams for collision experiments. The Atomic Collisions and Spectroscopy group in Eindhoven, is interested in creating 'slowed' (single-velocity) and 'intensified' (non-diverging) atomic beams, also referred to as 'bright beam'. Such a beam will drastically broaden the field of Atomic Physics, analogous to the introduction of lasers in the field of Optical Physics. Part of the thesis work deals with a pioneering study into beam slowing techniques, using an isotropic light field to cool the atomic beam. Short light cavities with low intensity fields result in a remarkable deceleration of the atomic beam. However, as a consequence of the isotropic photon distribution, the momentum recoils of the photons in an absorption-stimulated emission cycle do not necessarily cancel. Therefore, stimulated emission processes can no longer be neglected in our study.

3.1 Slowing techniques

The problem with slowing and/or cooling of a thermal atomic beam is that as the atoms are decelerated, they are tuned out of resonance due to the Doppler shift. For neon a

velocity change on the order of $\Delta v = \Gamma/k \approx 5 \text{ ms}^{-1}$ will shift the atom out of resonance. To slow the atoms over a large velocity range, *e.g.*, $\Delta v = v_{\text{final}} - v_{\text{initial}} = 500 \text{ ms}^{-1}$, the atom needs to be kept in resonance over a range of $\Delta\omega \approx 100\Gamma = 800 (2\pi)\text{MHz}$.

A possible solution is to chirp the laser frequency, using a laser beam counterpropagating with the atomic beam [10, 11]. The final velocity is determined by the range of the laser frequency sweep. However, a disadvantage of this technique is that the atomic beam becomes pulsed. Another drawback is the on-axis laser beam which necessarily intersects the crossing point of the atomic beams downstream.

An alternative setup is a so-called Zeeman-slower. In this approach the atomic frequency of the decelerating atom is kept in resonance by tuning the atoms through the Zeeman effect in a spatially varying magnetic field [4, 12, 13]. A counterpropagating laser beam compresses and slows the axial velocity distribution continuously. In addition to the on-axis laser beam, the stray magnetic fields may also constitute a disadvantage, since they may affect the atomic collisions that are studied with this ‘slowed’ and ‘cold’ beam.

To overcome the problem of a residual magnetic field and still have a continuous atomic beam, slowing with broadband laser light is an interesting option [14, 15]. The required on-axis laser beam has a broad frequency range, with a cut-off frequency characterizing the final velocity of the cooled atomic beam.

All of the above slowing techniques employ a counterpropagating laser beam, which can be disadvantageous if used in a crossed-beam setup. Since the transverse velocity components are ‘heated’ through spontaneous emission, the final beam velocity cannot be slowed below $v_{\text{final}} \approx 100 \text{ ms}^{-1}$ without incurring substantial losses due to transverse diffusion. Additionally, the laser demands on the performance are rather high in most of the cases. In view of these drawbacks, a simple alternative technique was developed recently, which appears to be promising. This technique consists of slowing and cooling in a monochromatic and isotropic light field [16, 17]. It is comparable to an ‘angle-tuned’ laser beam. The Doppler effect is compensated by selecting a ‘resonant angle’ of the incoming light. By means of newly developed materials, *e.g.*, Spectralon [18], we can create an isotropic light field in an optical cavity. The high overall reflectance results in large enhancement factors, which can cut down the laser power demands by an order of magnitude or even more. Presently, this new slowing technique is still in a research phase. Nevertheless, it may be a promising technique for a setup where a Zeeman-slowed atomic beam is ‘post-slowed’ to even lower axial velocities, $10 \text{ ms}^{-1} < v_{\text{final}} < 100 \text{ ms}^{-1}$.

3.2 Diffusely reflecting cavities

To create an isotropic light field from a well-directed laser beam, we need a diffusely reflecting material to construct an optical cavity. A high reflectance is desirable to

minimize the required laser power and obtain the desired isotropy. The commercially available material Spectralon [18, 19] satisfies the above demands. It can be considered as a porous stack of reflecting spheres. Photons diffuse into the stack and lose information of their initial direction. After several reflections, they may enter the cavity again in a random direction. This isotropic character is described by a Lambertian

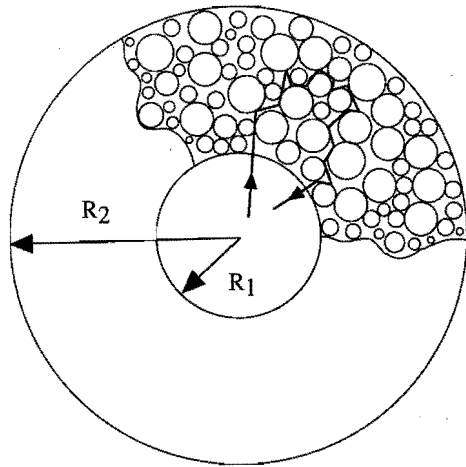


Figure 3: Schematic figure of a cylindrical slice of Spectralon. A photon penetrates into the material, with a certain probability of returning into the cavity in a random direction.

probability distribution $I(\text{s}^{-1}\text{sr}^{-1})$ for the reflected photons,

$$\begin{aligned} I(\Omega)d\Omega &= \frac{1}{\pi} \cos\theta \, d\Omega, \\ \int I(\Omega)d\Omega &= 1 \end{aligned} \quad (1)$$

with $d\Omega = \sin\theta d\theta d\phi$ the solid angle and $(0 < \theta < \pi/2, 0 < \phi < 2\pi)$ the polar angles with respect to the axis perpendicular to the wall. This distribution function is also called ‘cosine’ distribution.

The cavity geometry strongly determines the reflectance. Firstly, a minimum thickness of the cavity wall is required to ensure a reflection and a random direction because of the volume reflector effect (see Fig.3). Secondly, the ratio of the cavity volume and the Spectralon volume also influences the reflectance. A photon can be lost in the Spectralon material.

To show the influence of the geometry, the total probability for reflection back into the cavity can be calculated [20]. For a cylindrical cavity the reflectance as a function of the inner radius R_1 is depicted in Fig. 4. The thickness of the cavity wall, given by $R_2 - R_1$ with R_2 the outer radius, is kept constant. The calculation of the curve is based on $l_{\text{photon}} = 0.02 \text{ mm}$, which is the mean-free path of a photon between two reflections within the material, determined from available data for a rectangular slab of Spectralon with a thickness of 6 mm and a reflectance of $\mathcal{R} = 0.992$ [19]. For a

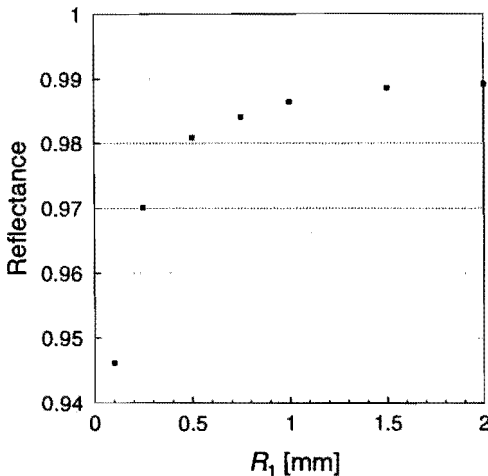


Figure 4: Reflectance as a function of the inner radius R_1 of a cylindrical cavity of Spectralon. The thickness of the wall $R_2 - R_1 = 15.25$ mm is kept constant and the length of the cavity is supposed to be infinite.

curved surface (as encountered in a cylindrical cavity) the effective reflectance depends on the radius of curvature divided by l_{photon} . As seen from Fig.4, a typical values of the reflectance range from 0.97 up to 0.99. Because the factor $(1 - \mathcal{R})^{-1}$ determines the recycling efficiency of the laser power this variation of \mathcal{R} has a large influence on the distribution of light in the cavity [21, 22].

4 This thesis

This thesis is based upon five papers. Chapter 2,3 and 4 relate to the deceleration of an atomic beam in an isotropic light field. The last two chapters, describe thermal collision experiments of electronically excited rare gas atoms in metastable (Xe^*) and shortlived (Kr^{**}) states, with $\text{N}_2(\text{X})$ as a collision partner.

Chapter 2 gives a theoretical description of the isotropic slowing effect. Apart from a numerical approach, the design of various isotropic light field cavities is discussed. Finally, simulations and a typical experiment are compared in order to check whether this application can be used in a bright beam configuration.

Chapter 3 discusses the effect of an isotropic light field on the spatial characteristics of an atomic beam. Stimulated emission causes a blow up of the beam in the transverse direction.

Chapter 4 includes a variety of experiments. Not only the deceleration of the atomic beam is measured but also its spatial characteristics. By using a 1-dimensional readout of a multi-channel plate detector, the deflection of the beam can be investigated. In addition, the comparison between model and experiment as described in chapter 2 is examined in detail.

Chapter 5 describes a thermal collision experiment between metastable $\text{Xe}(6p, {}^3\text{P}_2)$

and a ground state N_2 molecule. Analysis of the experiments by using a Landau Zener model confirms the existence of a double potential crossing between the initial and final state potentials.

Chapter 6 shows a collision experiment between the shortlived state $Kr(5p, {}^3D_3)$ and a ground state N_2 molecule. The final state results in a ground state Kr and an electronically and rovibrationally excited target molecule $N_2(C,v')$. The results are compared to the $Kr(5s, {}^3P_2)+N_2$ system [23].

The systems in chapter 5 and 6 demonstrate the different classes of both resonant and non-resonant processes. Moreover, they show the role of both electronic and kinetic energy as a mediator of the inelastic process.

Since this thesis has the format of a collection of papers, a certain amount of overlap between the various papers is inevitable, although kept to a minimum. Each paper stands for itself and clearly addresses a different aspect of the study of isotropic slowing and inelastic collisions of electronically excited atoms.

References

- [1] H. Beijerinck, *At. Mol. Phys.* **19**, 227 (1987).
- [2] J. Driessen and S. Leone, *J. Phys. Chem.* **96**, 6136 (1992).
- [3] E. Campbell, H. Schmidt, and I. Hertel, *Adv. Chem. Phys.* **72**, 37 (1988).
- [4] J. Prodan, W. Phillips, and H. Metcalf, *Phys. Rev. Lett.* **49**, 1149 (1982).
- [5] M. Manders, W. Boom, H. Beijerinck, and B. Verhaar, *Phys. Rev. A* **39**, 5021 (1989).
- [6] E. Spain, M. Dalberth, P. Kleiber, S. Leone, S. Op de Beek, and J. Driessen, (1995), accepted for publication in *J. Chem. Phys.*
- [7] R. Stebbings and F. Dunning, *Rydberg States of Atoms and Molecules* (Cambridge University Press, Cambridge, 1983).
- [8] H. Beijerinck, *Bull. Am. Phys. Soc.* **39**, 1116 (1994).
- [9] A. Aspect, R. Kaiser, N. Vansteenkiste, and C. Westbrook, (1994), submitted to *Phys. Scripta*.
- [10] V. Balykin, V. Letokhov, and V. Mishin, *Sov. Phys. JETP* **51**, 692 (1980).
- [11] W. Ertmer, R. Blatt, J. Hall, and M. Zhu, *Phys. Rev. Lett.* **54**, 996 (1985).
- [12] W. Phillips, J. Prodan, and H. Metcalf, *J. Opt. Soc. Am. B.* **2**, 1751 (1985).

-
- [13] T. Barrett, S. Dapore-Schwartz, M. D. Ray, and G. Lafyatis, *Phys. Rev. Lett.* **67**, 3483 (1991).
 - [14] M. Zhu, C. Oates, and J. Hall, *Phys. Rev. Lett.* **67**, 46 (1991).
 - [15] I. Littler, H.-M. Keller, U. Gaubatz, and K. Bergmann, *Z. Phys. D* **18**, 307 (1991).
 - [16] W. Ketterle, A. Martin, M. Joffe, and E. Pritchard, *Phys. Rev. Lett.* **69**, 2483 (1992).
 - [17] H. Batelaan, S. Padua, D. Yang, C. Xie, R. Gupta, and H. Metcalf, *Phys. Rev. A* **49**, 2780 (1994).
 - [18] polytetrafluoroethylene.
 - [19] Labsphere Inc., P.O.Box 70, North Sutton, NH 03260, USA.
 - [20] H. van Benthem, private communication.
 - [21] T.G. Aardema, R.M.S. Knops, S.P.L. Nijsten, J.P.J. Driessen and H.C.W. Beijerinck, this thesis: chapter II.
 - [22] T.G. Aardema, R.M.S. Knops, R.N.M. Vanneer, J.P.J. Driessen and H.C.W. Beijerinck, this thesis: chapter IV.
 - [23] E. Vredenbregt, W. Boom, R. van Gerwen, and H. Beijerinck, *Chem. Phys.* **145**, 267 (1990).

Chapter II

Isotropic light slowing of $\text{Ne}^*(^3\text{P}_2)$ atoms: cavity design and applications

T.G. Aardema, R.M.S. Knops, S.P.L. Nijsten,
J.P.J. Driessen, and H.C.W. Beijerinck

*Physics Department, Eindhoven University of Technology,
P.O. Box 513, 5600 MB Eindhoven, The Netherlands*

Abstract

The slowing effect of a cold (180 K) Ne^* atomic beam in an red detuned monochromatic isotropic light field has been studied by numerical simulation. A Monte Carlo method is applied to determine the intensity distribution of the isotropic light field in a cylindrical and spherical optical cavity, as well as to simulate the slowing effect. The intensity distribution in the spherical cavity is constant, in contrast with the peaked distribution for the cylindrical setup. The calculations show a large deceleration for short cavities and low laser input powers. The beam divergence is determined by both absorption-spontaneous emission and absorption-stimulated emission. For large saturation parameters, the stimulated emission becomes important. Comparing the calculations with experimental results indicates an overestimate of the simulated deceleration and subsequently, of the beam divergence. In the range of velocities where all atoms are slowed to a value near the resonance velocity, we obtain similar results for both the cylindrical and spherical cavity. For larger initial velocities, the photons are absorbed at larger top angles θ with respect to the atomic velocity v . In that case, absorption-stimulated emission cycles start to contribute significantly to the transverse diffusion. This results in a larger beam divergence for the cylindrical setup, where larger saturation parameters occur. Finally, this technique seems to be promising for application as a 'Post-Zeeman' slower.

1 Introduction

Using radiation pressure to cool or slow individual atoms [1, 2] is common practice nowadays. To slow an atomic beam one must solve the problem of the large inhomogeneous broadening due to the velocity distribution in comparison with the linewidth of the atomic transition. Because of the Doppler-effect, the decelerated atoms tune out of resonance. Various compensation schemes are possible to keep the laser frequency resonant with the atomic transition. Frequency chirping of the laser is a possibility [3, 4], but gives a non-continuous atomic beam. Changing the frequency of the atomic transition with a spatially varying magnetic field and thus compensating the Doppler-offset is also an option [5, 6]. However, this may cause non-desirable magnetic fields and field gradients in the interaction region. Another method is to use a broadband laser [7, 8]. A disadvantage of the above options is the counterpropagating laser beam on-axis with the atomic beam, which is difficult to implement experimentally without affecting or blocking the scattering region downstream. This problem might be solved by an ‘angle-tuned’ laser beam.

Recently, isotropic monochromatic light fields have been introduced as promising alternative beam slowers [9, 10]. This technique is based on geometric selection of resonant light through the Doppler effect. An atom with resonance frequency ω_0 compensates for the laser detuning, $\delta \equiv \omega_l - \omega_0$, by absorbing an incident photon from a cone with top angle $\theta = \arccos(-\delta/kv)$ with respect to the atomic velocity \vec{v} (Fig. 1). This results in

$$\omega - \omega_0 = \omega_l - \omega_0 + kv \cos \theta = \delta + kv \cos \theta, \quad (1)$$

with k the magnitude of the wave vector. For red detuned light, $\delta < 0$, we find $0 < \theta < \pi/2$, meaning that the average photon recoil, $v_{\text{recoil},\parallel} = \hbar k \cos \theta / m$, opposes the atomic motion. As the atoms decelerate, the angle θ decreases until the minimum value of $\theta (= 0)$ is reached, corresponding to the so-called resonance velocity

$$v_\delta = -\delta/k. \quad (2)$$

Thus, the force acting on the atom, which is velocity-dependent, can compress or cool a velocity distribution. However, the Lorentzian tail of the natural line shape may cause the atom to absorb photons for velocities $v < v_\delta$, if the observed detuning is on the order of an atomic linewidth Γ . This ‘off-resonance slowing’ will slow the atoms below the desired resonant velocity v_δ , because there is no restoring force to keep the velocity of the atoms at v_δ . The slowed peak will extend to velocities $v_f \approx v_\delta - \Gamma/k$.

The velocity change due to an absorbed photon, $v_{\text{recoil}} = \hbar k / m$, has a component both parallel ($\cos \theta$) and perpendicular ($\sin \theta$) to the atomic velocity \vec{v} . The parallel component can be utilized for slowing the atomic beam. Subsequent spontaneous emission results in a zero photon recoil on average, and the atoms are slowed. The perpendicular component of the photon recoil, $v_{\text{recoil},\perp} = \hbar k \sin \theta / m$, is zero on average.

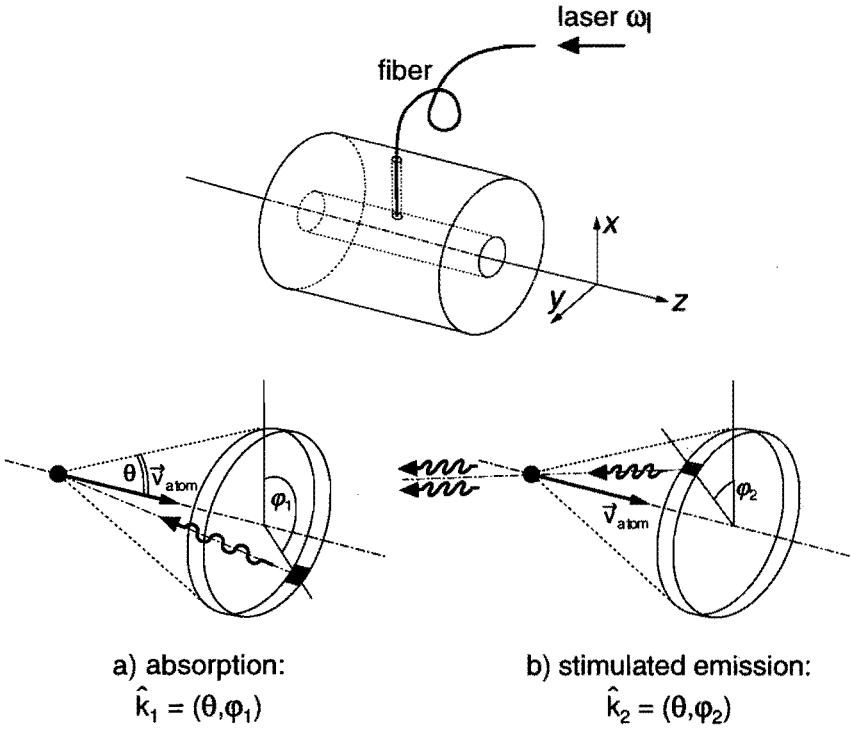


Figure 1: Cylindrical isotropic slower with laser light coupled into the cavity by using a fiber. An atomic beam enters the cavity in the z -direction and atoms absorb photons from a cone with top angle θ (panel a). The photon recoil parallel to the atomic velocity \vec{v} is cancelled by stimulated emission (panel b). The azimuthal angles of the absorbed and the emitted photon, φ_1 and φ_2 , result in a net velocity change of the atoms in the transverse direction.

However, the statistical distribution of the azimuthal angle of the absorbed photons (φ_1 in Fig. 1) and the random nature of the spontaneous emission afterwards lead to an increase of the perpendicular velocity spread, and contribute to the so-called transverse diffusion.

Additionally, the absorption-stimulated emission cycle has to be taken into account in isotropic light slowing. Stimulated emission by a resonant photon from the cone cancels the slowing effect of the absorbed photon (Fig. 1). However, in general the two photons involved have different azimuthal angles. This results in an extra transverse velocity change,

$$\Delta v_{\perp} = 2 v_{\text{recoil},\perp} |\sin((\varphi_1 - \varphi_2)/2)|, \quad (3)$$

and contributes to the transverse diffusion. We will refer to this extra transverse diffusion as stimulated diffusion.

This paper gives a model description isotropic light slowing and the strategy to calculate the spatial distribution of the light intensity in a cavity. The first two sections (2 and 3) describe the mathematical tools to calculate the average slowing effect and the light intensity in the cavity. As an example, we choose a cylindrical geometry for the optical cavity to create the isotropic light field. The following sections (4 and 5) describe the numerical recipes. A Monte Carlo simulation is used for calculating both the slowing rate and the intensity distribution. Finally, the last three sections (6, 7, and 8) discuss axial slowing, transverse diffusion, and a 'Post-Zeeman' slower for application in a scattering experiment.

2 Slowing by isotropic light

The spontaneous emission rate $\mathcal{S}_{\text{spont}}$ determines the slowing rate of an atom. Therefore, the force F_z of the light field on the atom equals

$$F_z = -\hbar k \cos \theta \mathcal{S}_{\text{spont}}. \quad (4)$$

An isotropic light field at a fixed frequency ω_l can be described as a broadband radiation field. In this case, the Einstein rate equations can be used to determine the spontaneous emission rate

$$\mathcal{S}_{\text{spont}} = \Gamma \frac{s}{2 + s \left(1 + \frac{g_g}{g_e}\right)}, \quad (5)$$

with s the saturation parameter, g_g and g_e the statistical weights of ground and excited state, respectively, and $\Gamma = \tau^{-1}$ the atomic linewidth. By incorporating the Lorentz profile of the atomic transition, the saturation parameter can be defined as

$$s = \frac{B_{ge}}{\Gamma/2} \int_{-\infty}^{+\infty} \mathcal{L}(\omega - \omega_0, \Gamma) U(\omega) d\omega, \quad (6)$$

where $\mathcal{U}(\omega)$ is the spectral density observed by the atom and B_{ge} the Einstein coefficient of the optical transition for absorption, given by

$$B_{ge} = \frac{g_e}{g_g} \frac{\pi^2 c^3}{\hbar \omega^3} \Gamma. \quad (7)$$

The Lorentz profile $\mathcal{L}(\omega - \omega_0; \Gamma)$ is defined as

$$\begin{aligned} \mathcal{L}(\omega - \omega_0; \Gamma) &= \frac{\Gamma}{2\pi} \frac{1}{(\omega - \omega_0)^2 + (\Gamma/2)^2}, \\ \int_{-\infty}^{+\infty} \mathcal{L}(\omega - \omega_0; \Gamma) d\omega &= 1, \end{aligned} \quad (8)$$

with ω_0 the central frequency of the atomic transition.

It is interesting to know the maximum slowing effect for an optical cavity with finite length L . This so-called 'capture range', Δv_{cap} , is defined as the maximum deceleration of an atom that is slowed in a finite interaction time Δt , and is equal to

$$\Delta v_{cap} = (v_i - v_\delta)_{max} = (v_{recoil,||} \Delta t \mathcal{S}_{spont})_{max} = v_{recoil} \frac{L}{v_\delta} \mathcal{S}_{spont}, \quad (9)$$

where L/v_δ is an upper limit for the interaction time.

3 Isotropic light cavity

An isotropic light field is created in a cylindrical cavity with walls which reflect with an isotropic distribution, the so-called Lambertian distribution or cosine distribution [11]. In practice, the material Spectralon is used to create isotropic light cavities [12]. This material is an ideal Lambertian reflector. Not only the isotropic character, *i.e.*, having the same properties in all directions, is important in the cavity, but also the variation of the intensity distribution along the cavity axis. Because the light intensity determines the maximum slowing rate, the geometry and the reflectance of the cavity should be taken into account. The reflectance of a flat surface of Spectralon is $\mathcal{R} \approx 0.99$. The average number of reflections per photon in a closed cavity is equal to $(1 - \mathcal{R})^{-1}$ and determines the recycling of the injected laser power. Moreover, the reflectance \mathcal{R} depends on the geometry due to the curvature of the surface and the fact that the photons diffuse into the material. Additionally, the entrance and exit apertures for the atomic beam result in a loss factor, f . In total, the enhancement factor of the cavity, *i.e.*, the average number of photon bounces in the open cavity, is determined by the reflectance \mathcal{R} and aperture losses f .

3.1 Wall reflection density $W(z)$

The wall reflection density $W[\text{m}^{-2}]$ is defined as the average number of photon reflections per unit area from the wall per photon entering the cavity. For an ideal closed

cavity without any losses (no apertures and a reflectance $\mathcal{R}=1$) the value of W would be infinite. However, in the case of Spectralon with a wall reflectance of $\mathcal{R} \approx 0.99$ and a surface area A of the cavity, the average value of W is equal to

$$\langle W \rangle = \frac{M \cdot \mathcal{R}}{A} = \frac{(1-f)}{(1-\mathcal{R})A} \mathcal{R}, \quad (10)$$

with M equal to the average number of reflections $1/(1-\mathcal{R})$ multiplied by the average probability $(1-f)$ to hit the wall once more after each reflection, instead of leaving the cavity through the apertures. This factor f determines the fraction of photons which leave the cavity through the entrance and exit apertures of the cavity. For a closed cavity we have $f=0$; the only way for the photons to leave the cavity is by diffusion through the wall. The factor $\mathcal{R}(1-f)/(1-\mathcal{R})$ defines the enhancement factor of the cavity.

For a cylindrical cavity with length L and diameter D , the method of Smith et al. [13] can be used to determine the loss factor f . They calculated the transmission, absorption and reflection for a free molecular flow of atoms through a cylindrical tube, with a Monte Carlo method for different ratios of $2L/D$. In the atomic analogue, the transmission factor is calculated at T_S , whereas the probability of sticking to the wall is given by S_S . This means that the entrance surface has an effective reflectance of $R_S=(1-T_S-S_S)$.

In the case of the optical cavity we have similar probabilities for transmission, reflection and the photon analogue of sticking, *i.e.*, diffusion through the wall. In our case, the photons start half way a cylindrical cavity. Therefore, the reflected photons (R_S) enter an identically cylindrical cavity and again a fraction of the photons will leave the cavity by either transmission or diffusion. In conclusion, the photons can leave the optical cavity through the apertures (T_S) or by diffusion through the wall (S_S). The fraction f of photons leaving through the apertures is given by

$$f = \frac{T_S}{1-R_S} = \frac{T_S}{T_S+S_S}. \quad (11)$$

Combining Eqs. (10) and (11) gives the average wall reflection density $\langle W \rangle$.

Another aspect of an isotropic light field is the fact that the traversed path of the photons through the cavity should be described by a random walk. The geometry of a sphere and the Lambertian character of the reflection satisfy this condition, if the apertures in the sphere are small in comparison with the surface area of the sphere itself. However, for a cylinder this is not trivial. To keep the average number of reflections, $(1-\mathcal{R})^{-1}$, within the cavity, the length L of the cavity must satisfy the condition

$$L \geq 2 \left[(1-\mathcal{R})^{-1} \cdot \Delta z^2 \right]^{\frac{1}{2}} \quad (12)$$

with $\Delta z^2 = 2/3D^2$ the average squared displacement in the z -direction between two reflections in a cylindrical setup. The factor 2 is added because the photons start halfway

Table 1: Standard Cylindrical Cavity.

Cavity parameters		
reflectance	\mathcal{R}	0.992
length	L	31.5 mm
inner diameter	D	1.5 mm
outer diameter	D'	32 mm
cavity factor	f	0.29
enhancement factor	$\frac{(1-f)\mathcal{R}}{(1-\mathcal{R})}$	88
wall reflection density	$\langle W(z) \rangle$	$5.9 \cdot 10^5 \text{ m}^{-2}$
Laser parameters		
detuning	δ	$-750 (2\pi)\text{MHz}$
resonance velocity	v_δ	480 ms^{-1}
wavelength	λ	640.225 nm

the cavity. However, the photons will hardly reach a distance beyond $[(1 - \mathcal{R})^{-1} \Delta z^2]^{1/2}$. Therefore, we choose the lower limit of Eq. (12) as a design criterium, which gives

$$\frac{L}{D} = 2 \sqrt{\frac{2}{3}} \sqrt{\frac{1}{1 - \mathcal{R}}}. \quad (13)$$

Using a value of the reflectance of $\mathcal{R}=0.992$, results in a ratio of $L/D \approx 20$ (Eq. (13)). This ratio L/D determines the length and diameter of the cavity, $L=31.5$ mm and $D=1.5$ mm, respectively, and results in an aperture loss of $f=0.29$ [13]. And finally, Eq. (10) gives an average value for the wall reflection density $\langle W \rangle \approx 5.9 \cdot 10^5 \text{ m}^{-2}$. Table 1 summarizes these values of our 'standard' cavity together with the standard laser parameters.

3.2 Spectral density $\mathcal{U}(\omega)$

To determine the force acting on an atom in an isotropic light field, the spectral density $\mathcal{U}(\omega)$, *i.e.*, the energy of the laser field per unit of frequency and volume with dimension Jm^{-3}s , should be calculated (Eqs. (4), (5) and (6)). The spectral density $\mathcal{U}(\omega; z, v)$ experienced by an atom moving with velocity v at position z , is determined by the characteristics of the cavity. Starting point is the distribution $\Phi_w(z)$ ($\text{Jm}^{-2}\text{s}^{-1}$) of the flux reflected by the walls of the cavity, as given by

$$\Phi_w(z) = W(z) P, \quad (14)$$

with P the optical input power and $W(z)$ the wall reflection density (Eq. (10)).

The power emitted by a cylindrical slice with area $2\pi R d\zeta$ located at position $z + \zeta$ is given by $\Phi_w(z + \zeta) \cdot 2\pi R d\zeta$ as is indicated in Fig. 2. The angular distribution of the

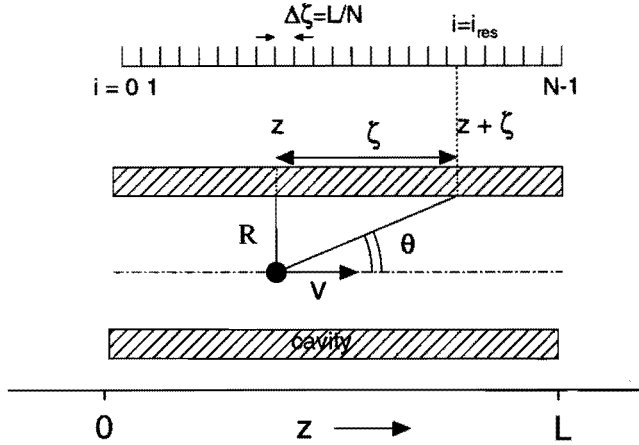


Figure 2: Schematic figure of the parameter definitions in a cylindrical isotropic light slower setup. The position of the cylindrical slices ($z + \zeta$) is given relative to the atomic position z .

emitted radiation is given by the probability distribution function $P(\alpha, \beta) = \cos \alpha / \pi$, with (α, β) the polar coordinates with respect to the normal on the surface. The contribution $d\Phi(\zeta; z)$ to the flux seen by the atom at position z is equal to

$$\begin{aligned} d\Phi(\zeta; z) &= \Phi_w(z + \zeta) 2\pi R d\zeta \cdot P(\pi/2 - \theta, \beta) \cdot \frac{1}{(\zeta^2 + R^2)} \\ &= \Phi_w(z + \zeta) 2 g(\zeta) d\zeta \end{aligned} \quad (15)$$

$$g(\zeta) = \frac{R^2}{(\zeta^2 + R^2)^{3/2}}, \quad (16)$$

where we have used the relation $\cos \alpha = \cos(\pi/2 - \theta) = R/(\zeta^2 + R^2)^{1/2}$.

The energy density $U(\zeta; z)$ (Jm^{-3}) at position z resulting from the wall slice at $z + \zeta$ is found by dividing $d\Phi(\zeta; z)$ by the speed of light c , resulting in

$$U(\zeta; z) d\zeta = \frac{\Phi_w(z + \zeta)}{c} 2 g(\zeta) d\zeta. \quad (17)$$

Finally, the energy density $U(\zeta; z)$ has to be transformed to the frequency domain ω perceived by the atom. The width of the cylindrical slice $d\zeta$ corresponds to a frequency interval $d\omega$ given by

$$\begin{aligned} \omega &= \omega_l + kv \cos \theta = \omega_l + kv \frac{\zeta}{(R^2 + \zeta^2)^{1/2}}, \\ d\omega &= |d\omega/d\zeta| d\zeta = kv g(\zeta) d\zeta. \end{aligned} \quad (18)$$

The spectral density $\mathcal{U}(\omega; z, v)$ seen by the moving atom is obtained by using Eq. (18) for the transformation to ω , resulting in

$$\mathcal{U}(\omega; z, v) d\omega = U(\zeta; z) \left| \frac{d\zeta}{d\omega} \right| d\omega = \frac{2 \Phi_w(z + \zeta)}{ckv} d\omega. \quad (19)$$

This result will be used in section 5 to calculate the absorption/(stimulated) emission cycles of the atom on its path through the cavity.

4 Monte Carlo simulation of $W(z)$

Section 3.1 gave a calculation of the average value of W . However, to determine the reflected light intensity $\Phi(z)$ as a function of the position z in the cavity no analytic functions are available. Therefore, on the analogy of calculations of free molecular flow through a tube [14], a Monte Carlo treatment is chosen to determine the wall reflection density. In our case, photons travel through a cylindrically symmetric cavity (Fig. 1) and reflect from a Lambertian surface with reflectance \mathcal{R} . Starting half way the cavity with length L and diameter D , we can determine the displacement of the photons along the z -axis of the cavity with two random numbers characterizing the polar angles (α, β) of the reflected photons. The total cavity is divided into N slices and each time a photon hits the wall at a certain slice ' i ' this is recorded in an array $[0..N - 1]$ at position ' i ' until the photon leaves the cavity. This results in a wall reflection density $W(z)$.

We can determine the distribution $W(z)$ of the standard cylindrical cavity (Table 1), corresponding to our experimental setup [15]. Figure 3 depicts the result for several values of the reflectance \mathcal{R} . The calculations are performed on an IBM RISC6000 system and take approximately 1/2 hour processing time. The input position of the photons is at $z=17$ mm, nearly halfway the length of the cylinder. For a reflectance of $\mathcal{R}=1$, the distribution $W(z)$ decreases linear as a function of the distance from the entrance position of the photons. The discontinuities at $z = 0$ and 31.5 mm result from the fact that photons can leave the cavity through the entrance and exit planes of the cylinder. Due to the finite probability to diffuse through the wall ($\mathcal{R} < 1$), the function $W(z)$ gradually changes to a concave shape with respect to the $\mathcal{R} = 1$ case: both the maximum and the full width at half maximum decrease with decreasing values of \mathcal{R} .

4.1 Geometry dependence of the reflectance

The $W(z)$ simulation is based on the material Spectralon, which is a volume reflector with photons diffusing a short distance into the material with a typical mean free path l_{photon} . The mean free path $l_{\text{photon}} = 0.02$ mm is given by the manufacturer and has been determined from data for a rectangular slab of Spectralon with a thickness of 6

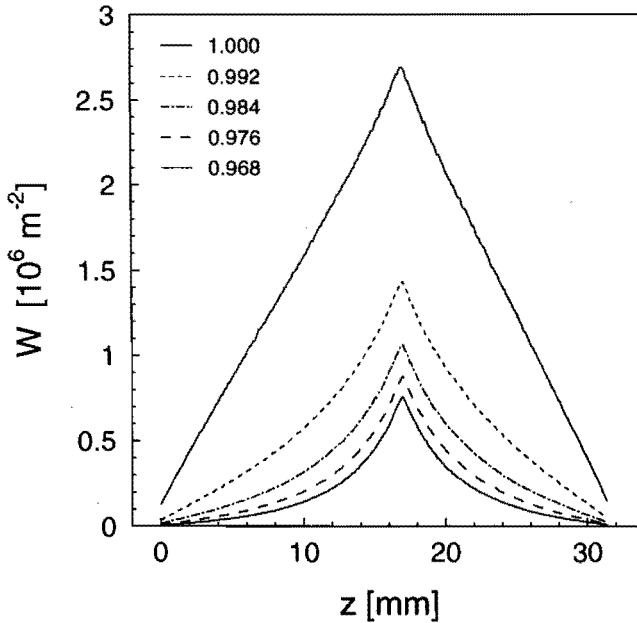


Figure 3: Simulation of the wall reflection density for a cylindrical symmetric cavity with $L=31.5$ mm, $D=1.5$ mm and reflectances of $\mathcal{R} = 1, 0.992, 0.984, 0.976$ and 0.968 , respectively. The photon entrance position is at $z = 17$ mm.

mm and a reflectance of $\mathcal{R}=0.992$ [12]. The cavity geometry strongly determines the reflectance. To show the influence of the geometry, the effective reflectance $\mathcal{R}(R_1, l_{\text{photon}})$ is shown in Fig. 4 as a function of the inner radius R_1 of a cylindrical cavity with $l_{\text{photon}} = 0.02$ mm. The thickness of the cavity wall, given by $R_2 - R_1$, has been fixed to 15.25 mm. The figure is based on calculations of Van Benthem et al.[16]. It should be noted that the reflectance is very sensitive to contamination of the Spectralon material. Due to absorption, the reflectance can change considerably [16]. This can result in a major change of the wall reflection density $W(z)$ because this distribution critically depends on the factor $(1 - \mathcal{R})^{-1}$. In Fig. 3, we see that a net change of \mathcal{R} from 0.992 to 0.968 results in nearly a factor 2 change in the maximum value of $W(z)$. The full width at half maximum decreases from 12 mm to 6 mm.

5 Monte Carlo simulation of slowing

To simulate the slowing effect of the atoms, we use a Monte Carlo method to determine the deceleration of the atoms and the spatial diffusion of the atomic beam. All atoms start on-axis and pass the cylindrical cavity [15]. We determine the probability of absorption and emission using the Einstein coefficients for absorption, stimulated emission and spontaneous emission: B_{ge} , B_{eg} and Γ , respectively, in combination with the calculated saturation parameter s (Eq. (6)) and the calculated wall reflection distri-

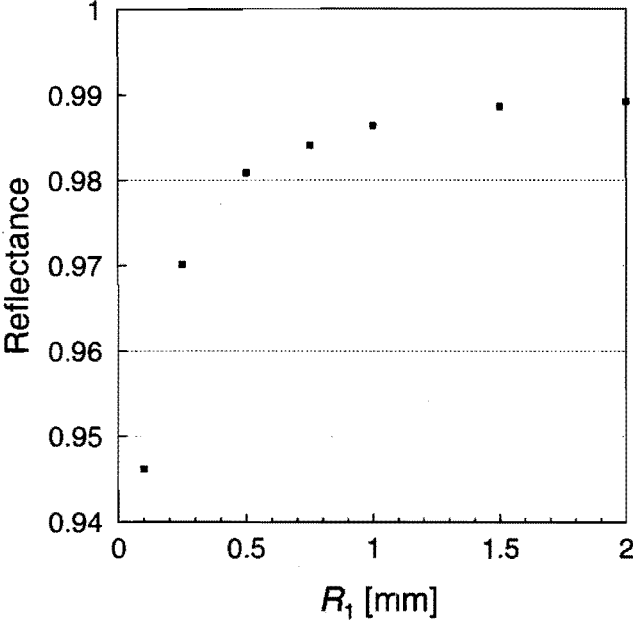


Figure 4: Reflectance parameter as a function of the inner radius R_1 of a cylindrical cavity of Spectralon. The thickness of the wall $R_2 - R_1 = 15.25$ mm is kept constant. The mean-free transport length is $l_{\text{photon}} = 0.02$ mm.

bution $W(z)$. The rates for absorption, stimulated emission and spontaneous emission are

$$\begin{aligned}
 \Xi_{\text{abs}} &= s \frac{\Gamma}{2}, \\
 \Xi_{\text{stim}} &= s \frac{g_g}{g_e} \frac{\Gamma}{2}, \\
 \Xi_{\text{spont}} &= \Gamma.
 \end{aligned} \tag{20}$$

The time intervals for absorption and emission are determined analytically with a random time-step

$$t = -\frac{\ln Q}{\Xi}, \tag{21}$$

with $Q \in [0..1]$ a random number and Ξ the total rate for absorption or emission (spontaneous and stimulated) Eq. (20). The resulting time-step t can range from 0 to infinity. Because the function $W(z)$ is strongly z -dependent, we need to limit this calculated time-step, thus avoiding large changes of the spectral density $\mathcal{U}(\omega; z, v)$ experienced by the atom during the time-step. We take the following strategy: an upper boundary t_1 for the time-step is chosen to limit the change in absorption and emission rates to a maximum of 20%. In case $0 < t < t_1$, the atom traverses a distance $v \cdot t$ after which an absorption or emission takes place. If, on the other hand, $t > t_1$, the atom is propagated over $v \cdot t_1$ without any absorption/emission. After this time-step

a new time interval is calculated and the procedure is repeated until the atom leaves the cavity.

Incorporated in the Monte Carlo approach are the atomic linewidth, together with a fixed angle θ for absorption and stimulated emission determined by the resonance condition. The saturation parameter s is determined according to the Lorentzian distribution weighted with the spectral density (Eq. (6)). The calculations have been performed on an IBM RISC6000 system, with an average calculation time of 1 hour, for typically 1000 trajectories at a single initial velocity. The output of each trajectory is: v_f , v_x and v_y . Further data processing has been performed on a PC.

5.1 Numerical implementation

To calculate the different absorption and emission rates we have to determine the saturation parameter s (Eq. (6)). This parameter is a function of the velocity v of the atom and its position z in the cavity, because the spectral density $\mathcal{U}(\omega; z, v)$ is determined by these parameters (Eq. (19)). We will use the following numerical recipe in our computer program. The cylindrical cavity is divided into N slices ($i = 0..N - 1$) (Fig.2). Each slice is located at a certain position z_i and has a width $\Delta\zeta = L/N$, with L the total length of the cavity. For all slices the total light intensity $\Phi_{w,i}$ is calculated numerically in the previously described Monte Carlo simulation of $W(z)$.

Using the $\zeta \leftrightarrow \omega$ transformation, the spectral density $\mathcal{U}(\omega_i; z, v)$ of the cylindrical slice 'i' can be determined through

$$\begin{aligned} \mathcal{U}(\omega_i; z, v) &= U(\zeta_i; z) \left| \frac{\Delta\zeta_i}{\Delta\omega_i} \right| = \frac{2\Phi_w(z + \zeta_i)}{ckv}, \\ \Delta\omega_i &= kv g(\zeta_i) \Delta\zeta_i = kv \frac{R^2}{(\zeta_i^2 + R^2)^{3/2}} \frac{L}{N}, \\ \zeta_i &= z_i - z, \end{aligned} \quad (22)$$

where we have used Eq. (17). In the limit for $v \downarrow 0$, *i.e.*, the frequency width $\Delta\omega_i$ goes to zero, the $\zeta \leftrightarrow \omega$ transformation results in an infinitely large Jacobian and $\mathcal{U}(\omega_i; z, v)$ becomes infinite. Analytically, this results in a delta function $\delta(\omega - \omega_0)$, which can lead to numerical problems. Therefore, we will distinguish between the three following cases.

First, when $\Delta\omega_i > 9\Gamma$ the $\zeta \leftrightarrow \omega$ transformation does not give any numerical infinities. The contribution $\Delta s_i(z, v)$ of each cylindrical slice to the saturation parameter $s(z, v)$ is now calculated using Eq. (6), resulting in

$$\begin{aligned} \Delta s_i(z, v) &= \frac{B_{ge}}{\Gamma/2} \int_{\omega_{l,i}}^{\omega_{h,i}} \mathcal{L}(\omega - \omega_0, \Gamma) \mathcal{U}(\omega_i; z, v) d\omega \\ &= \frac{B_{ge}}{\Gamma/2} \mathcal{U}(\omega_i; z, v) \delta_{i,iree}, \end{aligned} \quad (23)$$

with i_{res} the index corresponding to the on-resonance slice with $\cos\theta = -\delta/kv$ and $\zeta \in [\zeta_i, \zeta_i + L/N]$. The boundaries $\omega_{1,i}$ and $\omega_{\uparrow,i}$ are given by ω_i and $\omega_i + \Delta\omega_i$, respectively.

Secondly, when $\Delta\omega_i > \Gamma/10$ the $\zeta \leftrightarrow \omega$ transformation again does not give any numerical infinities. However, in this case the Lorentz profile of the atom is divided over more cylindrical slices, resulting in

$$\Delta s_i(z, v) = \frac{B_{ge}}{\Gamma/2} \mathcal{U}(\omega_i; z, v) \int_{\omega_{1,i}}^{\omega_{\uparrow,i}} \mathcal{L}(\omega - \omega_0, \Gamma) d\omega. \quad (24)$$

Thirdly, in the case that $\Delta\omega_i \leq \Gamma/10$ we will use a slightly different $\zeta \leftrightarrow \omega$ transformation, which takes into account the finite line width of the laser radiation. This laser frequency profile, given by a ‘Lorentz profile’ $\mathcal{L}(\omega - \omega_l, \Delta\omega_l)$, is very narrow compared to the atomic transition: $\Delta\omega_l \ll \Gamma$. The following transformation into the frequency domain gives a non-zero width $\Delta'\omega_i$ and a finite height $\mathcal{U}'(\omega_i; z, v)$:

$$\begin{aligned} \mathcal{U}'(\omega_i; z, v) \Delta'\omega_i &= U(\zeta_i; z) \Delta\zeta_i = U(\zeta_i; z) \frac{L}{N}, \\ \Delta'\omega_i &= \Delta\omega_l + \Delta\omega_i. \end{aligned} \quad (25)$$

The contribution $\Delta s_i(z, v)$ of the cylindrical slice ‘ i ’ to the saturation parameter $s(z, v)$ can now be obtained from Eq. (6), using the approximation that the ‘Lorentz function’ $\mathcal{L}(\omega_i - \omega_0, \Gamma)$ is constant over the frequency interval $\Delta'\omega_i$:

$$\begin{aligned} \Delta s_i(z, v) &= \frac{B_{ge}}{\Gamma/2} \mathcal{L}(\omega_i - \omega_0, \Gamma) \int_{\omega_{1,i}}^{\omega_{\uparrow,i}} \mathcal{U}'(\omega_i; z, v) d\omega \\ &= \frac{B_{ge}}{\Gamma/2} \mathcal{L}(\omega_i - \omega_0, \Gamma) \mathcal{U}'(\omega_i; z, v) \Delta'\omega_i \\ &= \frac{B_{ge}}{\Gamma/2} \mathcal{L}(\omega_i - \omega_0, \Gamma) U(\zeta_i; z) \frac{L}{N}, \end{aligned} \quad (26)$$

with the boundaries $\omega_{1,i}$ and $\omega_{\uparrow,i}$ given by ω_i and $\omega_i + \Delta'\omega_i$, respectively. Note that the final expression does not depend on the laser frequency profile anymore.

Finally, the total saturation parameter $s(z, v)$ observed by the atom is obtained by summing the contributions $s_i(z, v)$ of Eqs. (23), (24) or (26) over the N slices ($i = 0..N - 1$).

$$s(z, v) = \sum_{i=0}^{N-1} \Delta s_i(z, v). \quad (27)$$

In practice, we limit this summation to intervals with a non-negligible contribution. Cylindrical slices where the integration range $\omega_{1,i}.. \omega_{\uparrow,i}$ in Eqs. (24) or in Eq. (26) lie outside the optical transition range $[\omega_0 - \frac{9}{2}\Gamma, \dots, \omega_0 + \frac{9}{2}\Gamma]$ are neglected in this summation, *i.e.*, the summation goes over a range of slices centered around i_{res} . In conclusion, the absorption, stimulated emission and spontaneous emission rates can now be calculated by using Eq. (20).

6 Axial slowing and diffusion

In order to demonstrate the slowing of a Ne^* atomic beam in an isotropic light field, we study the case of the standard cylindrical optical cavity (Table 1). In this case, the reflectance is estimated at $\mathcal{R}=0.968$. The wavelength of the closed two-level system of Ne^* is equal to $\lambda=640.2$ nm. Furthermore, the experimental velocity distribution of the Ne^* source has an average velocity of $\langle v \rangle \approx 550 \text{ms}^{-1}$ and a velocity spread of $\approx 130 \text{ms}^{-1}$ [17]. Thus, a large slowing effect can be expected with a detuning of $\delta = -750 (2\pi) \text{MHz}$, corresponding with a resonance velocity $v_\delta=480 \text{ms}^{-1}$.

The simulated effect of $P=15$ mW laser input power in the Spectralon cavity is depicted in Fig. 5, where the deceleration Δv is shown as a function of the initial velocity v_i . As defined in Eq. (9), the capture range is the maximum deceleration of an atom. The initial velocities in the range $(v_\delta, v_\delta + \Delta v_{cap})$ are transformed to a small range of final velocities, within a finite interaction time. Owing to the Lorentzian tail of the atomic linewidth, some of the atoms can reach even lower values. This so-called 'off-resonance' slowing is indicated by the cross-hatched area in Fig. 5a.

Initial velocities which cannot reach the resonant velocity v_δ , obtain a deceleration Δv with a velocity dependence v^{-n} with n ranging from 2 to 3,

$$\begin{aligned} s \gg 1 & ; \quad \Delta v \propto \frac{1}{v^2} \\ s \ll 1 & ; \quad \Delta v \propto \frac{1}{v^3}. \end{aligned} \quad (28)$$

This dependence results from the interaction time ($\propto L/v$), the $\cos \theta$ term of the Doppler effect ($\propto \delta/kv$) and the behavior of \mathcal{S}_{spont} as a function of the saturation parameter s (Eqs. (4) and (5)). For high input powers $\mathcal{S}_{spont} \propto \Gamma/2$, but for low input powers $\mathcal{S}_{spont} \propto s$, which is proportional to v^{-1} (Eqs. (6) and (19)). For the situation with input power $P=15$ mW, the simulation gives an exponent lying somewhere between -2 and -3 .

More insight into the axial slowing process can be obtained from Fig. 6. This diagram shows the atomic velocity as a function of the position along the beam axis. The Spectralon cavity is positioned between $z = 0$ mm and $z = 31.5$ mm. Again the capture range can be determined and the off-resonance slowing is clearly seen. It is interesting to note that for initial velocities near v_δ , the deceleration already starts upstream of the cavity entrance. Of course this is trivial, because the resonance angle θ of the light cone is almost zero for atoms with velocities around v_δ . Thus, the atoms see the cavity before they actually enter it. For higher velocities, the starting position of the deceleration shifts towards $z = 0$ and scales with $\cos \theta$ because of the resonance condition Eq. (1). A similar effect occurs at the exit of the cavity.

Atoms with velocities below v_δ can still see resonant light in front of the cavity due to the Lorentzian tail of the atomic linewidth. This would result in a starting

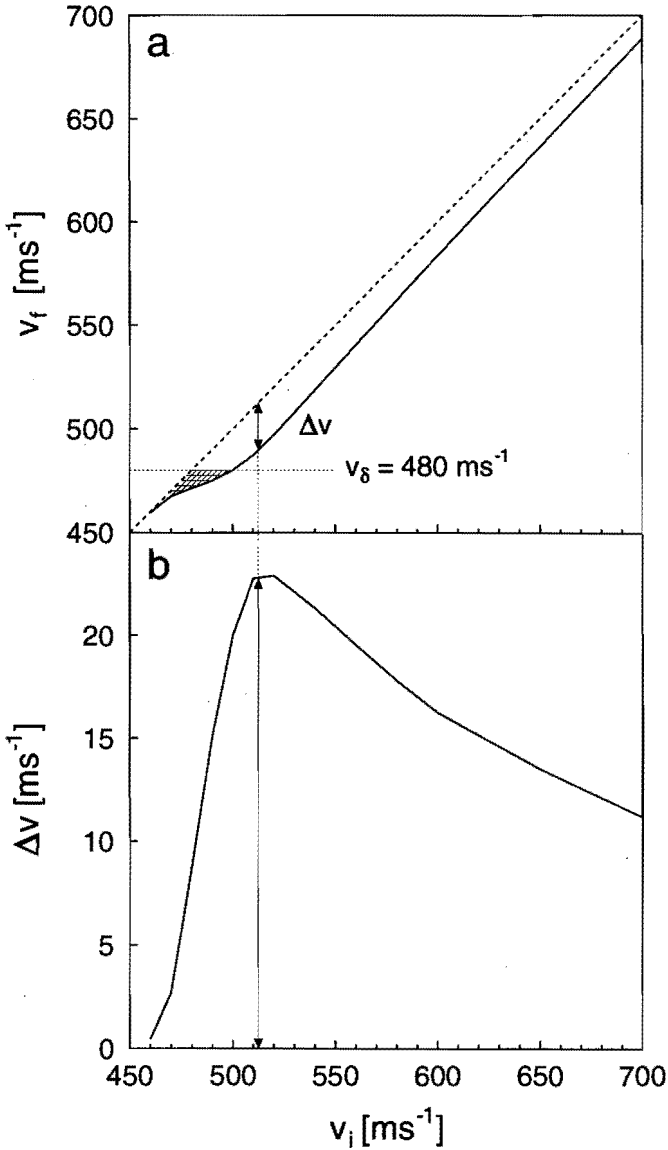


Figure 5: The velocity dependence of a Ne^* beam in an isotropic light field, represented in: a) final velocity and b) velocity difference. The capture range is indicated ($\Delta v_{cap} \approx 25 \text{ ms}^{-1}$) and nearly equals the maximum velocity difference (panel b). The high-velocity tail (panel b) has a dependence of $\propto v_i^{-n}$ ($n \in [2,3]$). The reflectance of the cavity is $\mathcal{R}=0.968$. The cross-hatched area represents 'off-resonance' slowing.

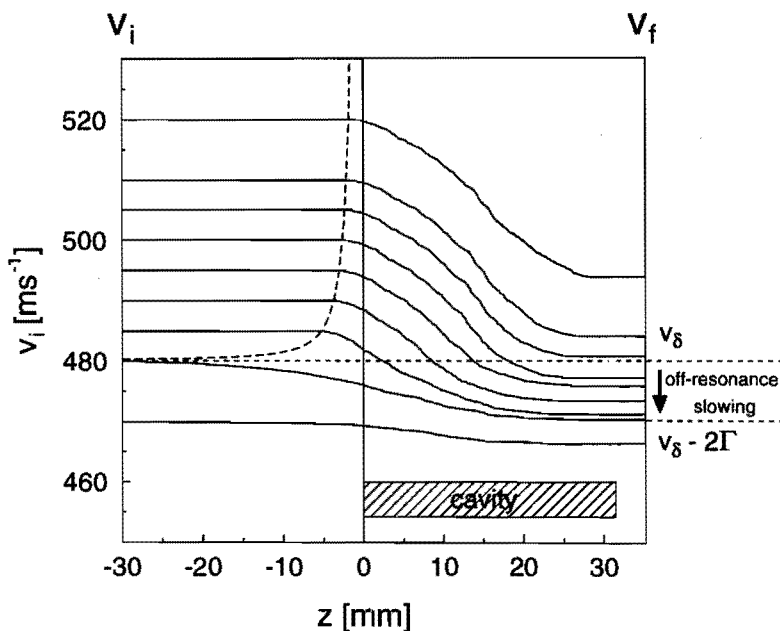


Figure 6: Parallel atomic velocity v as a function of the axial position z for various initial velocities, as simulated for the standard cylindrical cavity with a reflectance of $\mathcal{R}=0.984$ and a laser power $P=15$ mW. The resonant velocity $v_\delta=480$ ms^{-1} ($\delta = -750$ (2π)MHz) is indicated. Due to the Doppler effect the initial position of the deceleration process lies upstream of the cavity entrance, as indicated by the dashed line. The capture range is on the order of $\Delta v_{cap} \approx 25\text{ms}^{-1}$. The off-resonance slowing effect is clearly seen for velocities $v < 480$ ms^{-1} , with a typical deceleration $\Delta v \leq 10\text{ms}^{-1}$, which is smaller than Δv_{cap} .

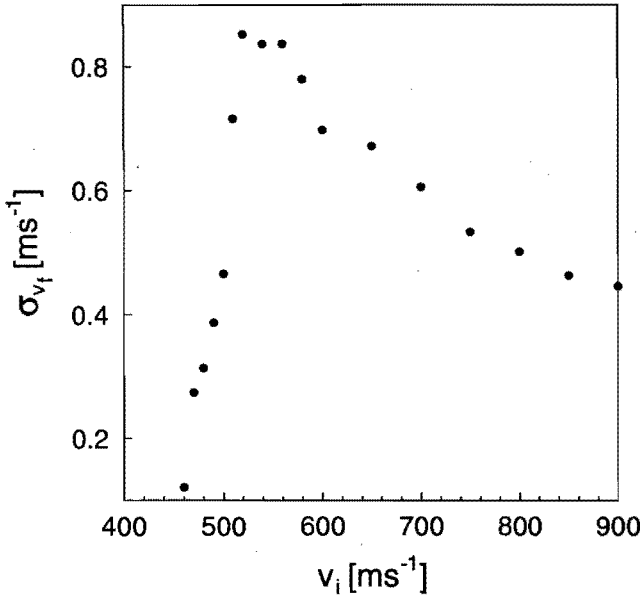


Figure 7: The r.m.s. value of the velocity spread σ_{v_f} , for different initial velocities. The value is determined by the spontaneous emission effect.

position at $z = -\infty$ with respect to the cavity. However, the light intensity drops by z^{-2} . Therefore, a maximum starting distance position is chosen in all Monte Carlo calculations: $z = -L = -31.5$ mm.

With regard to the parallel velocity component, we now want to look for the r.m.s. velocity spread σ_{v_f} of the final velocity distribution in case of a single initial velocity (standard cavity; Table 1, $\mathcal{R} = 0.968$, $P = 15$ mW). Figure 7 shows the width σ_{v_f} as a function of the initial velocity v_i , giving small values on the order of $\sigma_{v_f} \approx 0.8$ ms $^{-1}$. The shape of the curve is similar to the curve in Fig. 5, where the deceleration $\Delta v = v_f - v_i$ is proportional to the number of absorption-spontaneous emission cycles N . The parallel velocity spread σ_{v_f} originates from the random nature of the spontaneous emission processes, and is proportional to \sqrt{N} , explaining the comparable shape of both curves.

7 Transverse diffusion

In case of an isotropic light field, spontaneous emission is not the only contribution to the transverse diffusion of the atomic beam. Stimulated emission can have a large effect on the spatial characteristics of the beam as well. Due to the varying azimuthal angle between absorption φ_1 and stimulated emission φ_2 (Fig. 1) an extra transverse velocity change occurs Eq. (3). In Fig. 8a we show the r.m.s beam divergence $\sigma_\theta = v_\perp/v_f$ of the atoms caused by transverse diffusion. Again we use the standard cavity parameters with a reflectance $\mathcal{R} = 0.968$ and laser power $P = 15$ mW (Table 1). The position of

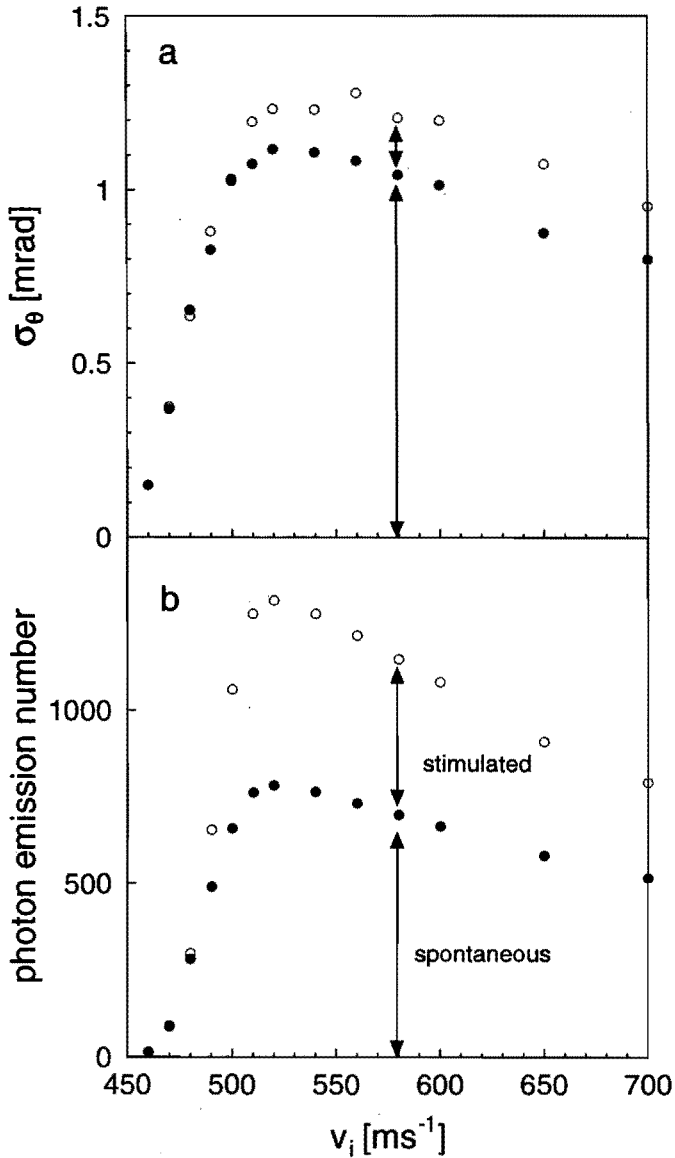


Figure 8: The influence of spontaneous and stimulated emission on the r.m.s. divergence σ_θ of the atomic beam (panel a) and the total number of spontaneous and stimulated emission events (panel b). The total effect of spontaneous plus stimulated emission is indicated by the open symbols (○), whereas the contribution from the spontaneous emission only is indicated by the solid symbols (●).

maximum divergence corresponds to the fastest atoms just at the outer edge of the capture range, *i.e.*, the atoms which acquire the largest deceleration and experience the largest number of absorption-emission cycles (Fig. 5). The resonance condition for these atoms results in a rather large initial angle θ , resulting in a fairly large contribution from stimulated diffusion ($\propto \sin^2 \theta$).

The importance of stimulated diffusion is also obvious from Fig. 8a, which also shows the result of the Monte Carlo calculation where the effect stimulated emission has been eliminated. The latter has been achieved by fixing $\varphi_1 = \varphi_2$ for the azimuthal angles involved in the absorption-stimulated emission cycle. Stimulated emission causes an extra divergence angle of ≈ 0.2 mrad. Figure 8b indicates the number of spontaneous emission events, together with the total number of emitted photons. In first order the result of Fig. 8a can be obtained from Fig. 8b by multiplying the resonant transverse recoil component ($v_{\text{perp}} \propto \sin \theta v_{\text{recoil}}$) with the total number of stimulated emission events and the perpendicular spontaneous recoil component ($v_{\perp} \propto \sqrt{2/3} v_{\text{recoil}}$) with the total number of spontaneous emission events. For velocities smaller than the resonant velocity v_{δ} , the effective saturation parameter is smaller and the contribution of absorption-stimulated emission cycles ($\propto s^2$) is negligible in comparison with the absorption-spontaneous emission cycles ($\propto s$). Together with a small resonance angle of the absorbed photons ($\sin \theta \approx 0$) this results in a negligible contribution of absorption-stimulated emission cycles to the transverse diffusion.

8 Comparison of experiment and simulation

To demonstrate the validity of the model, the calculated deceleration (Fig. 5) and the transverse diffusion (Fig. 8) are combined to simulate an experimental velocity distribution for the standard cylindrical cavity with a reflectance of $\mathcal{R}=0.968$ (Table 1). Simultaneously, the reflectance of the Spectralon cavity can be checked. This is important in order to investigate the geometry dependence of the reflectance in the optical cavity.

An initial parallel velocity distribution is transformed to a slowed spectrum using the calculated deceleration Δv . This results in a final velocity distribution with a narrow peak at a slightly shifted velocity at $v \simeq v_{\delta} - 2\Gamma/k$; the extra deceleration is due to off-resonance slowing [9]. The width of the slowed peak in the transformed velocity distribution, results from the slowly varying final velocity within the capture range (Fig. 5a), in combination with the parallel velocity spread $\sigma_{v_{\parallel}}$ for each final velocity (Fig. 7). Finally, the TOF velocity resolution and the finite solid angle acceptance of the detector have been taken into account, resulting in a simulated experimental velocity distribution which can be compared with the corresponding experimental results.

Figure 9 presents the experimental results for an initial ('laser off') and final velocity distribution ('laser on'), as measured for Ne⁺ in a 'standard' Spectralon cavity with

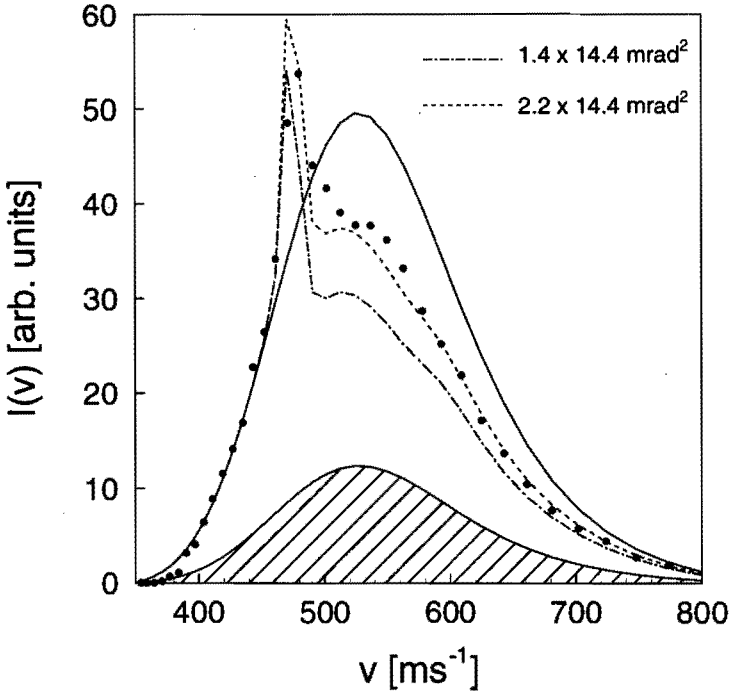


Figure 9: Experimental data for the initial (laser off, solid line) and the final (laser on, $P=15$ mW, full dots) velocity distribution, as compared with a calculated velocity distribution with laser on ($\mathcal{R}=0.968$, $P=12$ mW). The slowing of the atoms is clearly visible. The hatched area represents the velocity distribution of the 25% metastable atoms which are unaffected by the laser light, *i.e.*, $^{22}\text{Ne}^*$ and $\text{Ne}^*(^3\text{P}_0)$. The loss of beam flux for $v \gg v_\delta$ is caused by the slowing process and the finite acceptance of the detector, calculated for $x' \times y' = 1.4 \times 14.4$ mrad 2 (dashed-dotted line) and 2.2×14.4 mrad 2 (dashed line).

$P=15$ mW (Table 1). Due to off-resonance slowing, the peak of slowed atoms is located at a velocity $v \simeq v_\delta - 2\Gamma/k$, slightly below the resonant velocity $v_\delta = 480$ ms $^{-1}$. If the areas above and below the initial velocity distribution (laser 'off') are compared with the final distribution (laser 'on'), a large discrepancy is visible. This is caused by the finite solid angle acceptance of the detector in the experiment: the transverse diffusion causes part of the atoms to obtain such a large deflection that they do not reach the detector. The solid angle acceptance of the detector is $x' \times y' = 1.4 \times 14.4$ mrad 2 .

The final velocity distribution has been calculated, using a reflectance $\mathcal{R}=0.968$ and a power of $P=12$ mW. The reflectance value determines the shape of the slowed curve, resulting in a more severe loss of atoms for higher reflectance values. Furthermore, changing the reflectance does not result in a significant change in the peak position of

the curve. Changing the laser input power results in similar effects as for the reflectance. However, no change in shape occurs. Again, within the experimental laser power fluctuations (± 3 mW) the height and shape of the curve remains more or less the same. Figure 9 shows the calculated curve. The discrepancy between experiment and calculation is rather large. An explanation for this effect could be a too large calculated number of absorption-spontaneous emission and absorption-stimulated emission cycles, resulting in an overestimated deceleration and beam divergence. In the simulation all the atoms start on axis, whereas in the experimental setup the beam is determined by a finite aperture. Thus, by changing the solid angle acceptance of the detector more insight would be gained into this problem. Adjusting the solid angle acceptance to 2.2×14.4 mrad² results in a nearly perfect agreement between calculation and experiment. For the high velocity tail the match is very good, but near the slowed peak there is a difference. The simulated data give a smaller peak as compared with the experiment which still has a small shoulder. This is caused by the fact that the calculation does not take into account the apertures in front of the Spectralon cavity in the experimental setup (see chapter IV). Thus, this change in aperture size may indicate that our present analysis is incomplete.

Finally, the reflectance value of $\mathcal{R}=0.968$ lies within the range calculated by Van Benthem et al. [16] for this cylindrically symmetric geometry. Furthermore, the simulations give a clear insight into the process of isotropic slowing and can be used to predict the effect of different cavity designs.

9 Spherical cavity

Until now we have studied the influence of an isotropic light field on a Ne* beam using a cylindrical cavity (Table 1), because in practice it is the most straightforward to construct. We have seen that the deceleration and the beam divergence strongly depend on the light distribution in the cavity, *i.e.*, the wall reflection distribution $W(z)$. The peaked structure of the $W(z)$ distribution of the cylindrical cavity (Fig. 3) results in large saturation parameters and subsequently in a major contribution of the absorption-stimulated emission cycles to the transverse diffusion. To minimize this effect, we would like to have a constant $W(z)$ value as a function of the position z , which would give us the opportunity of minimizing the beam divergence and maximizing the deceleration, by fine tuning the laser power P . A spherical cavity satisfies these conditions.

In the case of a spherical geometry with the area of the apertures small in comparison with the total area of the sphere, the cavity is close to ideal. Photons will stay in the cavity until they escape through the wall. Additionally, the loss factor will be $f \approx 0$ Eq. (11), and together with Eq. (10) the constant wall reflection density can be calculated. Based upon the experimental situation in Chapter IV, we studied a spherical cavity with a radius of $R = 8$ mm and on both sides two short cylindrical

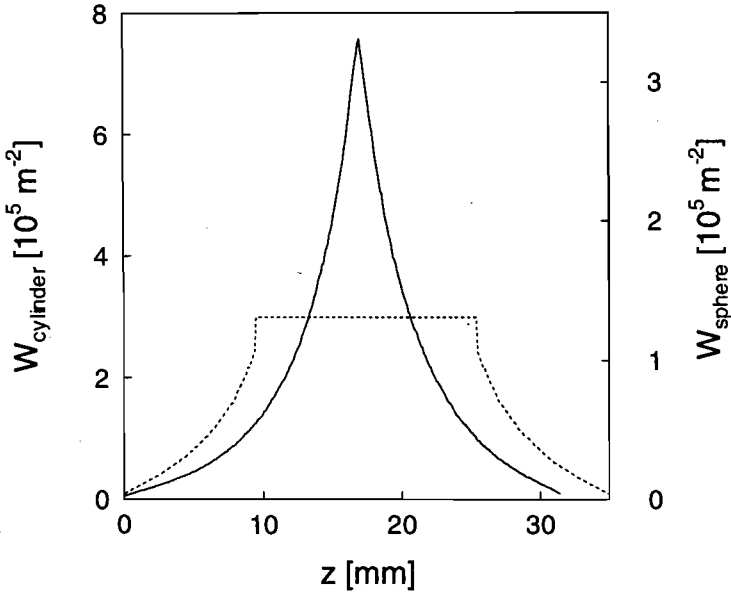


Figure 10: Wall reflection density $W(z)$ of the standard cylinder (solid line) and sphere (dashed line). The reflectance of the cylinder and the cylindrical entrance and exit parts of the sphere is $\mathcal{R}=0.968$. The spherical part has a reflectance of $\mathcal{R}=0.990$. Values of the $W(z)$ distribution are depicted on the left and right y-axis for the cylinder and sphere, respectively.

cavities with each a length of $L = 9.5$ mm and a bore diameter of $D = 1.5$ mm. Thus, the effective length of the spherical section is $L_{eff} = 35$ mm. For the calculation of $W(z)$ in respect of the cylindrical parts of the sphere, the same method as described in section 4 was used and for the spherical part Eq. (10) was used. The reflectance of the cylindrically shaped cavities is $\mathcal{R}=0.968$ and for the spherical cavity $\mathcal{R}=0.990$. This total cavity is referred to as the spherical setup, whereas the pure cylindrical cavity is referred to as the cylindrical setup. Figure 10 shows the wall reflection density $W(z)$ of both the cylindrical setup (Table 1) and the spherical setup.

In case of the spherical setup, the light distribution does not depend on the axial position of the atom in the spherical part of the cavity. The discontinuities in the wall reflection density $W(z)$ at the boundaries of the spherical and cylindrical part are due to the abrupt change in the solid angle, with a corresponding change in the photon-flux incident on the wall-elements per surface area. In the cylindrical setup the light intensity varies with the axial position. Differences in absolute values of both setups are caused by the different geometries. Comparing the two $W(z)$ distributions for the cylindrical and spherical setup results in approximately a factor 2.3 difference

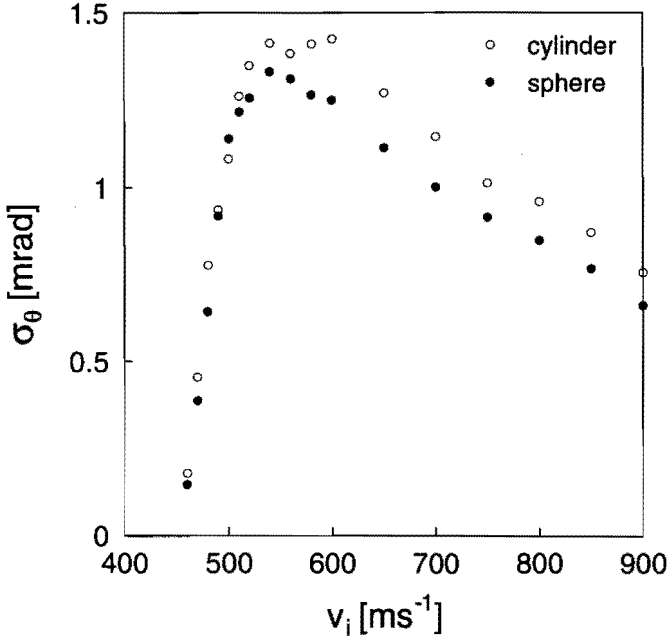


Figure 11: Calculations of the r.m.s. beam divergence σ_θ for the cylindrical (\circ) and spherical (\bullet) optical cavity with an input power of $P=30$ and 41 mW, respectively. The laser detuning is $\delta = -750$ (2π)MHz.

in the average values of the wall reflection densities. Accordingly, the laser input power should be adjusted with the same factor, to create the same deceleration for both cases. The average value of the wall reflection density $W(z)$ for the cylindrical and spherical setup are: $1.9 \cdot 10^5 \text{ m}^{-2}$ and $0.8 \cdot 10^5 \text{ m}^{-2}$, respectively. Keep in mind that the reflectance of the Spectralon material strongly depends on the geometry of the cavity [16].

In two simulations for the spherical and cylindrical setup we tune the input power P in such a way that in both cases the same deceleration occurs. Consequently, the difference in input power determines the desired scaling factor. These calculations result in a factor 1.4, which is smaller than the expected value of 2.3. This is due to the fact that the effective length of the spherical setup is longer in comparison with the cylinder. The saturation parameter is constant over a longer range and fixed at a certain value in such a way that more absorption-spontaneous emission cycles occurs. Apart from the larger input power, the use of laser power in the spherical setup is more effective.

In these simulations we can also obtain information on the divergence of the slowed atomic beam in the case of the cylindrical and spherical setup. Figure 11 depicts the

r.m.s. divergence σ_θ of the beam. Although the both setups give the same values of σ_θ within the capture range Δv_{cap} , there is a difference for initial velocities above this range. In this example, the difference is about 0.15 mrad. Fine tuning the laser power to create the same deceleration results in almost equivalent capture ranges, which are small enough to avoid large contributions of stimulated emission within the capture range. Therefore, the two cases described above do not differ as to beam divergence within the capture range. Atoms with an initial velocity v_i in this range will reach the final velocity v_f . However, for atoms with a larger initial velocity the specific shape of the wall reflection density starts to play an important role. The interaction time with the isotropic light field for those atoms results in a certain final velocity $v_i > v_f > v_b$ depending on the number of absorption-spontaneous or stimulated emission cycles.

10 Post-Zeeman slower

To use an isotropic light field to slow a thermal atomic beam (*e.g.* a Ne^* beam source at $T=180$ K, with an average velocity of $v \approx 600 \text{ ms}^{-1}$) to velocities in the Kelvin range requires a huge amount of laser power in comparison with the conventional Zeeman slowing technique [5, 6], because the needed interaction time results in a very long optical cavity ($L > 2$ m). Besides, stimulated diffusion can be disastrous for the spatial characteristics of the atomic beam (section 7). However, as mentioned in the introduction the absence of both magnetic fields and an on-axis laser beam is rather promising for scattering applications. In our opinion, an isotropic light slower is ideal in combination with a Zeeman slower. In this combination the isotropic light field decelerates the atoms below a velocity of $v \approx 100 \text{ ms}^{-1}$, since below this value the disadvantages of the Zeeman technique outweigh the advantages [18]. For the deceleration from $v \approx 100 \text{ ms}^{-1}$ down to the sub-thermal velocities we can use short cavities and low input powers. However, we must keep in mind that for short cylindrical cavities (small L/D ratios) power losses f through the entrance and exit apertures become important [13].

As an example of a 'Post-Zeeman' slower we have simulated the effect of a cylindrical cavity with length $L=15$ mm, diameter $D=1.5$ mm, reflectance $\mathcal{R}=0.984$ and an input power $P=2$ mW. At the entrance, we assume a Ne^* beam with an average velocity of $v \approx 100 \text{ ms}^{-1}$ and a velocity spread of $\sigma_v \approx 10 \text{ ms}^{-1}$, typical values for a Zeeman slower [18]. To decelerate the atomic beam to a final velocity $v_f \approx 50 \text{ ms}^{-1}$, we apply a detuning of $\delta = -110$ (2π)MHz, corresponding to $v_\delta = 70.4 \text{ ms}^{-1}$. Due to the off-resonance slowing the total number of absorption/emission cycles increases, resulting in a capture range $\Delta v_{cap}^{eff} \approx 50 \text{ ms}^{-1}$. This is larger than predicted by Eq. (9). Furthermore, the r.m.s. beam divergence σ_θ will be minimal because the resonance condition results in small angles θ .

Before we investigate the final velocity distribution, $P(v)$, we first have a look at the

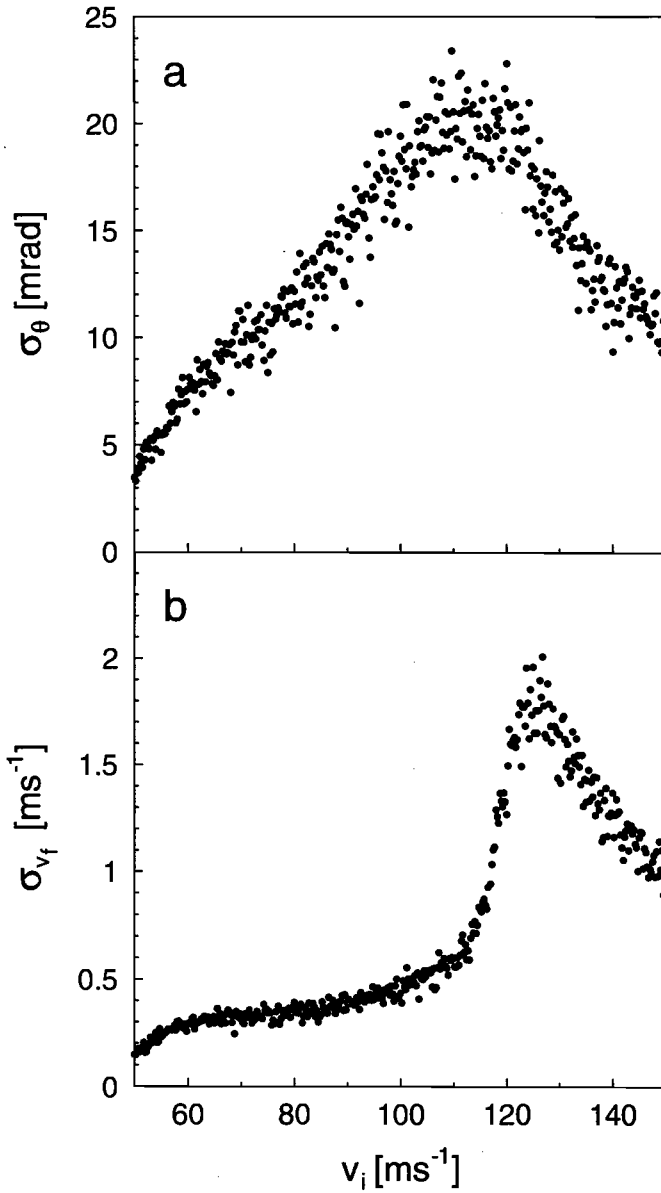


Figure 12: Simulation of the beam divergence (panel a) and the final velocity spread (panel b). For a large number of initial velocities the above values are calculated by averaging over 100 simulated trajectories. The capture range is on the order of $\Delta v_{cap} \approx 35 \text{ ms}^{-1}$, which corresponds to the flat part in panel b).

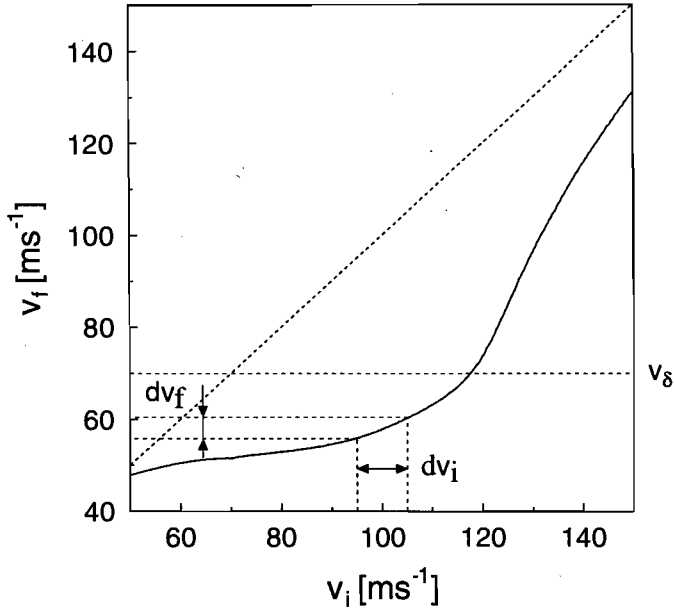


Figure 13: Deceleration curve for the ‘Post-Zeeman’ slower. In the range where $dv_f/dv_i < 1$, the velocity distribution is compressed, *i.e.*, cooling is observed.

transverse diffusion and the parallel velocity spread. In Fig. 12 the beam divergence, σ_θ , and the parallel velocity spread σ_{v_f} are depicted, as a function of the initial velocity. The most striking result is the rather large divergence $\sigma_{\theta, max} = 20$ mrad. Due to the low axial beam velocity (z -component) we obtain a large deflection angle, which is proportional to v_\perp/v_\parallel . This geometric divergence should be taken into account when designing a ‘Post-Zeeman’ slower. Of course several solutions are possible to minimize this negative effect. Enlarging the cavity and simultaneously minimizing the laser input power could be an option. However, when the capture range is enlarged (Eq. (9)), initial velocities with increasing absorption angles θ are slowed to v_δ as well. Therefore, the contribution of stimulated emission to the transverse diffusion becomes more important. For the parallel velocity component we obtain a low value for the final velocity spread σ_{v_f} . The velocity spread never exceeds a value larger than 2 ms^{-1} . This value is reasonable for a cold atomic beam setup [18].

To investigate the transformation of the velocity distribution for an atomic beam entering an isotropic light slower we should have a closer look at the deceleration curve. Figure 13 shows the final velocity v_f as a function of the initial velocity v_i . In the range where the slope dv_f/dv_i is less than one, the initial velocity distribution can be compressed. For initial velocities near the resonant velocity v_δ , the slope approaches

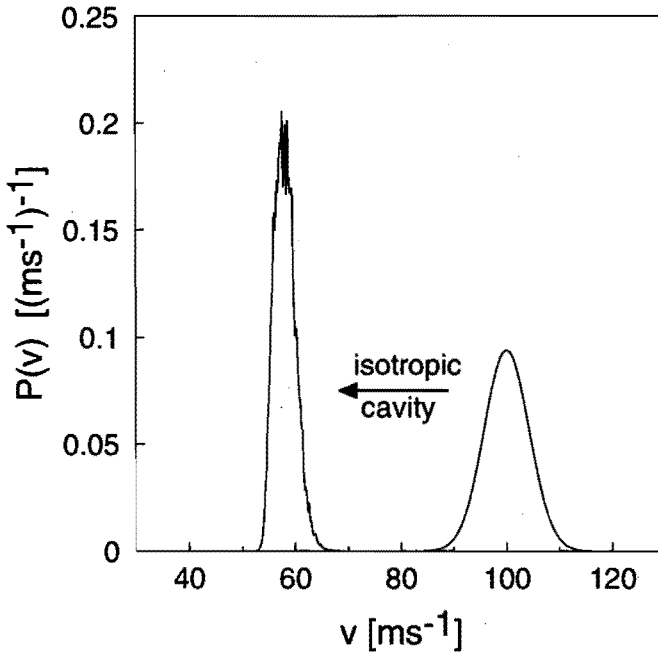


Figure 14: Transformation of the velocity distribution of an atomic beam. The initial velocity distribution with $\langle v_i \rangle = 100 \text{ ms}^{-1}$ and $\sigma_{v_i} = 10 \text{ ms}^{-1}$ is transformed to a final distribution with $\langle v_f \rangle = 57 \text{ ms}^{-1}$ and a r.m.s. spread of $\sigma_{v_f} = 6 \text{ ms}^{-1}$, *i.e.* slowing and cooling are observed. Both distributions are normalized to unity.

zero and a large velocity compression is possible. The shape of the curve for $v_f < v_i$ corresponds to 'off-resonance' slowing due to the Lorentzian tail of the atomic linewidth.

Finally, Fig. 14 depicts the transformation of an initial velocity distribution. The total deceleration is equal to $\Delta v = v_i - v_f = 43 \text{ ms}^{-1}$ and the initial width $\sigma_{v_i} = 10 \text{ ms}^{-1}$ of the velocity distribution is compressed to a final value $\sigma_{v_f} = 6 \text{ ms}^{-1}$. The compression can be optimized to a smaller value by choosing the initial distribution in the range with a smaller value of the slope of the deceleration curve (Fig. 13). Note that in this transformed velocity distribution the axial diffusion σ_{v_f} has been taken into account. (Fig. 12).

11 Concluding remarks

The effect of an isotropic light field on a Ne^* atomic beam has been investigated by using a theoretical model and comparing its calculations with a representative experimental result. Apart from deceleration, a significant divergence of the atomic beam is

introduced. The absorption-stimulated emission cycles lead to a large spatial change of the beam, especially when the resonance condition results in large angles θ . By using model calculations, more insight has been gained into this isotropic slowing process. However, the calculations overestimate the slowing effect and, consequently, the transverse diffusion of the atomic beam. An important aspect related to this point is the experimental realization of the isotropic light field. The reflectance of the material (Spectralon) used to create the enhanced isotropic light field strongly depends on the geometry of the optical cavity. Although the wall reflection density and the reflectance can be calculated, they are difficult to verify experimentally. However, changing the laser input power and reflectance in the simulations, no exact match with the experiment could be obtained within the experimental fluctuations and predicted ranges. This may indicate that our model is still incomplete. Other materials for the optical cavity, such as TiO_2 , may be used in the future to check whether they are better suited to create an isotropic light field.

Apart from the discrepancies between calculations and experiment, we can still deduce important information from the performance of the isotropic light slower. For example, the difference between cylindrical and spherical geometry results only in larger beam divergence of the atomic beam of the cylinder, for velocities above the capture range. We assume that the capture range is small enough to exclude transverse diffusion resulting from large resonance angles ($\Delta v_1^2 \approx \sin^2 \theta$). Finally, the use of an isotropic light slower as a 'Post-Zeeman' slower looks promising. The deceleration process is more effective for lower velocities. Because of the long interaction time less laser power is required. However, the transverse diffusion becomes important at lower velocities, since it scales with the parallel velocity component $\sigma_\theta = v_\perp/v_\parallel$. Furthermore, an initial velocity distribution with a width smaller than the capture range is not only decelerated but also compressed within the capture range. A limiting factor here is that the width of the initial distribution should be larger than the created axial velocity spread during the deceleration.

References

- [1] T. Hänsch and A. Schalow, *Opt. Comm.* **13**, 68 (1975).
- [2] D. Wineland and H. Dehmelt, *Bull. Am. Phys. Soc.* **20**, 637 (1975).
- [3] V. Balykin, V. Letokhov, and V. Mishin, *Sov. Phys. JETP* **51**, 692 (1980).
- [4] W. Ertmer, R. Blatt, J. Hall, and M. Zhu, *Phys. Rev. Lett.* **54**, 996 (1985).
- [5] W. Phillips, J. Prodan, and H. Metcalf, *J. Opt. Soc. Am. B.* **2**, 1751 (1985).

-
- [6] T. Barrett, S. Dapore-Schwartz, M. D. Ray, and G. Lafyatis, *Phys. Rev. Lett.* **67**, 3483 (1991).
 - [7] M. Zhu, C. Oates, and J. Hall, *Phys. Rev. Lett.* **67**, 46 (1991).
 - [8] I. Littler, H.-M. Keller, U. Gaubatz, and K. Bergmann, *Z. Phys. D* **18**, 307 (1991).
 - [9] W. Ketterle, A. Martin, M. Joffe, and E. Pritchard, *Phys. Rev. Lett.* **69**, 2483 (1992).
 - [10] H. Batelaan, S. Padua, D. Yang, C. Xie, R. Gupta, and H. Metcalf, *Phys. Rev. A* **49**, 2780 (1994).
 - [11] M. Born and E. Wolf, *Principles of Optics* (Pergamon Press, Oxford, 1975).
 - [12] Labsphere Inc., P.O.Box 70, North Sutton, NH 03260, USA.
 - [13] C. Smith and G. Lewin, *J. Vac. Sci. Techn.* **3**, 92 (1966).
 - [14] M. Stevens, H. Beijerinck, and N. Verster, *Physica* **83C**, 209 (1976).
 - [15] T.G. Aardema, R.M.S. Knops, R.N.M. Vanneer, J.P.J. Driessen and H.C.W. Beijerinck, this thesis: chapter IV.
 - [16] H. van Benthem, private communication.
 - [17] M. Hoogerland, Ph.D. thesis, Eindhoven University of Technology, The Netherlands, (1993).
 - [18] E. Vredenburg, private communication.

Chapter III

Transverse diffusion in isotropic light

T.G. Aardema, R.M.S. Knops, S.P.L. Nijsten,
J.P.J. Driessen, and H.C.W. Beijerinck

*Physics Department, Eindhoven University of Technology,
P.O. Box 513, 5600 MB Eindhoven, The Netherlands*

Abstract

We have demonstrated the slowing of a beam of cold (180 K) metastable neon atoms in a diffuse reflecting cylindrical cavity with monochromatic light. Using a well collimated atomic beam entering the cavity, it is shown that stimulated emission has a major effect on the transverse velocity distribution. A large saturation parameter s results in a loss mechanism for the centerline beam intensity. A Monte Carlo simulation shows that the light intensity should be evenly distributed with moderate saturation conditions, to optimize the slowing effect while minimizing the transverse diffusion.

Studying cold collisions requires dense samples of cold atoms. The method used so far has been to fill a trap with slow atoms that are subsequently cooled to the desired temperatures in the mK-range. The collision processes are then probed by observing, *e.g.*, the trap loss rate, or in more detail, the yield of fluorescence or electrons. Commonly used methods for slowing atoms down to velocities in the capture range of the trap ($\approx 10 \text{ ms}^{-1}$ for Na or metastable Ne) are the Zeeman technique [1, 2] and the chirped frequency technique [3, 4]. Recently white light [5, 6] and isotropic monochromatic light slowers [7, 8] have been introduced as promising alternatives. Isotropic light slowers are interesting because of their simple implementation into an atomic beam line and the absence of both magnetic fields and an on-axis laser beam.

Monochromatic isotropic light slowing is based on geometric selection of resonant light through the Doppler effect. An atom with resonance frequency ω_a compensates for the laser detuning, $\delta = \omega_l - \omega_a$, by absorbing an incident photon from a cone with top angle $\theta = \arccos(-\delta/kv)$ with respect to the atomic velocity \vec{v} (see Fig. 1), resulting in

$$\omega_a = \omega_l + kv \cos \theta \quad (1)$$

with k the magnitude of the wave vector. The corresponding velocity change, $v_{\text{recoil}} = \hbar k/m$, has components *both* parallel ($\cos \theta$) and perpendicular ($\sin \theta$) to the atomic velocity \vec{v} . The parallel component can be utilized for slowing the atomic beam. For red detuned light, $\delta < 0$, we find $0 < \theta < \pi/2$, meaning that the average photon recoil, $v_{\text{recoil},\parallel} = \hbar k \cos \theta/m$, opposes the atomic motion. Subsequent spontaneous emission results in a zero photon recoil on average, and the atoms are slowed. As the atoms decelerate, the angle θ decreases until the minimum value of $\theta (= 0)$ is obtained, corresponding to a final atomic velocity $v_f = -\delta/k$. The perpendicular component of the photon recoil, $v_{\text{recoil},\perp} = \hbar k \sin \theta/m$, is zero on average. However, the statistical distribution of the azimuthal angle of the absorbed photons (φ_1 in Fig.1a) and the random nature of the spontaneous emission afterwards lead to an increase of the perpendicular velocity spread, $\langle \Delta v_{\perp}^2 \rangle$, and contribute to the so-called transverse diffusion.

In contrast to conventional Zeeman slowing, the absorption-stimulated emission cycle has to be taken into account in isotropic light slowing. Stimulated emission by a resonant photon from the cone cancels the slowing effect of the absorbed photon. However, in general the two photons involved have a different azimuthal angle, $\Delta\varphi = \varphi_1 - \varphi_2$ (Fig.1). This results in an extra transverse velocity change, $|\Delta v_{\perp}| = 2 v_{\text{recoil},\perp} \sin(\Delta\varphi/2)$, and also contributes to the transverse diffusion. The average contribution for one absorption-stimulated emission cycle is equal to

$$\langle \Delta v_{\perp}^2 \rangle_{\Delta\varphi} = 2 v_{\text{recoil},\perp}^2 = 2 (\hbar k/m)^2 \sin^2 \theta. \quad (2)$$

We will refer to this extra transverse diffusion as *stimulated diffusion*. In this letter we investigate the isotropic slowing of a beam of cold metastable neon atoms. The

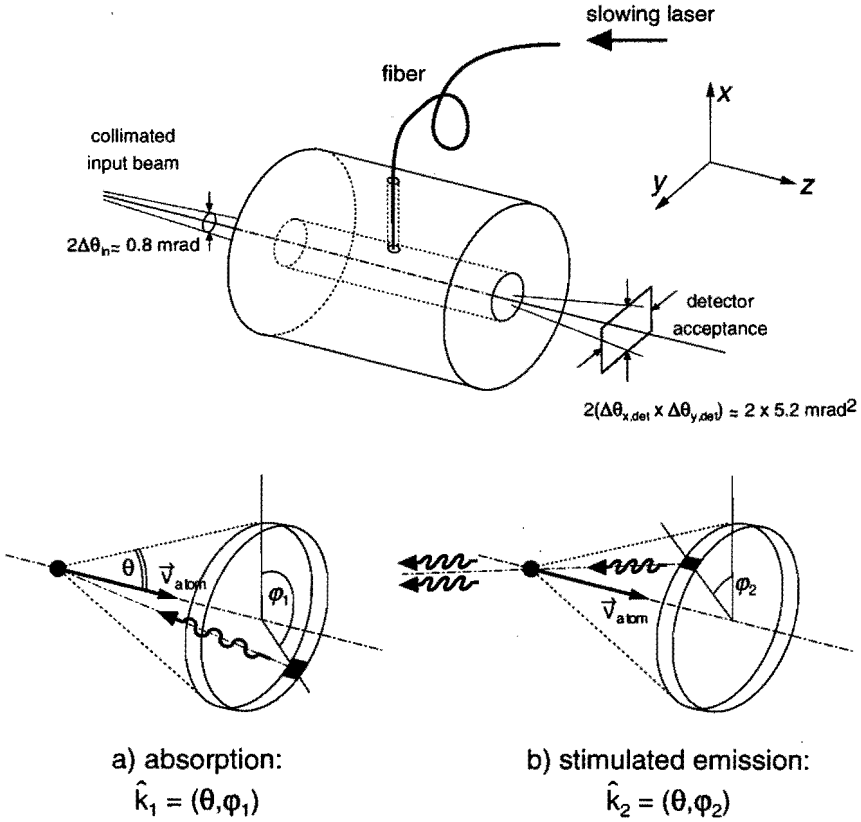


Figure 1: The isotropic slower is a 31.5 mm long cylindrical Spectralon rod with an inner diameter of 1.5 mm. Laser light is coupled into the cavity using a multimode fiber. Atoms entering the cavity are collimated to $\approx 0.8 \text{ mrad}$. An aperture in front of the detector determines the solid angle acceptance, $\approx 2 \times 5.2 \text{ mrad}^2$. Atoms absorb photons from a cone with top angle θ (Figure a). The photon recoil parallel to the atomic velocity \vec{v} is cancelled by stimulated emission (Figure b). The azimuthal angles of the absorbed and the emitted photon, φ_1 and φ_2 , result in a net velocity change of the atoms in the transverse direction.

effect of the photon recoil, $\hbar k/m = 0.03 \text{ ms}^{-1}$, on the transverse diffusion will also be studied.

The isotropic slower is implemented experimentally using cylindrical sections of Spectralon[9], a material with a diffuse reflectivity $R \approx 0.99$. The outer diameter of the Spectralon rod is 32 mm. The length of a single section is $L = 31.5 \text{ mm}$; the bore has an inner diameter $d = 1.5 \text{ mm}$. Up to three cavity sections can be lined up, thus enlarging the cavity length. Light is coupled into the cavity sections halfway using a multimode optical fiber (see Fig.1). The intensity distribution $\Phi(z)$ of the laser light on the cavity walls is calculated using a Lambertian reflector[10]. It is found to drop nearly linear in the z -direction from the center to the outer ends by a factor of 40, which depends critically on the length-to-diameter ratio L/d .

A CW ring dye-laser (Spectra Physics) is tuned near resonance to the Ne $\{3s \ ^3P_2\} \leftrightarrow \{3p \ ^3D_3\}$ two level transition at $\lambda=640.2 \text{ nm}$. Saturated absorption at the atomic frequency ω_a is used to calibrate the laser frequency ω_l . The laser frequency is locked to an electronically controlled external cavity, providing the desired frequency offset, $\delta = -2\pi \times 750\text{MHz}$ ($v_l=480 \text{ ms}^{-1}$). No active long-term drift corrections for the laser frequency are made. The maximum frequency drift is estimated at $\approx 10 \text{ MHz/hour}$, which is acceptable with typical measuring times of 10 minutes for a velocity distribution.

A beam of cold metastable Ne^* atoms is passed through the cavity to determine the influence of the isotropic light field on *both* the axial (\parallel) and perpendicular (\perp) velocity distribution. The Ne^* atoms are produced in a discharge-excited supersonic expansion source, cooled with liquid nitrogen to an effective temperature of $T_{\parallel} \approx 180 \text{ K}$ [11], corresponding with a mean velocity of $v_{\parallel} \approx 560 \text{ ms}^{-1}$ and a velocity spread of $\Delta v_{\parallel} \approx 130 \text{ ms}^{-1}$. The final velocity distribution $P(v_{\parallel})dv_{\parallel}$ is determined using the time-of-flight (TOF) method with a mechanical chopper and a metastable atom detector, which are located 790 mm and 1760 mm downstream of the isotropic slower, respectively. The velocity resolution, $\Delta v_{\text{TOF}} = 20 \text{ ms}^{-1}$ at $v_{\parallel} \approx 500 \text{ ms}^{-1}$, is determined by the width of the slit in the mechanical chopper[12]. To measure the effect of transverse diffusion on the perpendicular velocity distribution, we collimate the beam entering the cavity to $2 \times \Delta\theta_{\text{in}} \approx 0.8 \text{ mrad}$, *i.e.*, a perpendicular velocity spread $\Delta v_{\perp} \approx 0.2 \text{ ms}^{-1}$. The rectangular solid acceptance angle of the metastable atom detector is $\approx 2 \times 5.2 \text{ mrad}^2$, corresponding to a maximum velocity spread $\Delta v_{\perp} \approx 3 \text{ ms}^{-1}$. Thus transverse diffusion can result in a loss of detected metastable atoms.

The measured velocity distributions for three values 3×2.5 , 3×10 and $3 \times 40 \text{ mW}$ of input power are shown in Fig.2. Three Spectralon sections are aligned, each equipped with a separate optical fiber. As a reference the initial velocity distribution is given, as measured with the laser switched 'off'. Note that 25% of the detected metastable atoms is not affected by the light: it is the wrong isotope, 10% $^{22}\text{Ne}^*$, or a different metastable level, 15% $^{20}\text{Ne}^*(^3P_0)$. The effect of slowing is obvious. Atoms with a higher

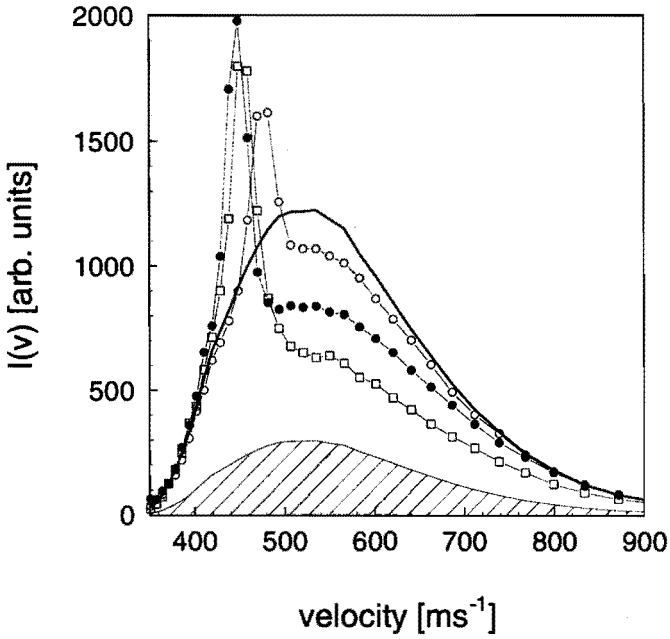


Figure 2: Experimental results for velocity distributions with 'laser on' and 'off', obtained with three Spectralon sections. The laser detuning is $\delta = -750 (2\pi)\text{MHz}$ ($v_f = 480 \text{ms}^{-1}$). The laser powers used are $3 \times 2.5 \text{mW}$ (\circ), $3 \times 10 \text{mW}$ (\bullet), and $3 \times 40 \text{mW}$ (\square). The solid line represents the initial distribution ('laser off'). The hatched area represents the velocity distribution of the 25% metastable atoms which are unaffected by the laser light, *i.e.*, $^{22}\text{Ne}^*$ and $\text{Ne}^*(^3\text{P}_0)$.

initial velocity are slowed towards the final velocity of $v_f=480 \text{ ms}^{-1}$ ($\delta=-2\pi\times 750 \text{ MHz}$) resulting in a sharp peak in the laser 'on' distributions. The width of the peaks is $\Delta v_f \approx 20 \text{ ms}^{-1}$, in agreement with Δv_{TOP} . Due to drift of ω_l in time between the measurements, the frequency shift δ is slightly different for the three power settings. The height of the slowed peak hardly increases with increasing laser power.

The most remarkable feature is the pronounced discrepancy in the area above and below the initial velocity distribution when comparing the 'on' and 'off' situation: some of the atoms are obviously lost when they are decelerated. The only explanation is transverse diffusion beyond the acceptance angle of the atomic beam detector. For higher input powers the difference becomes even more pronounced, implying that stimulated diffusion is becoming increasingly important.

To investigate the above effect we simulate the atomic trajectories in the slower with a Monte Carlo calculation. All atoms start on axis and thus see a cylindrical slice of the cavity wall with resonant light (Fig.1a). The effective width of the slice is determined by the Lorentzian profile of the transition. The energy density distribution $U(\omega, z)d\omega$ experienced by the moving atom can be derived from the calculated light intensity $\Phi(z)$ on the cavity wall using the Doppler effect. Therefore, the rates of absorption, stimulated and spontaneous emission can be calculated with a simple semiclassical approach using the Einstein-coefficients and the energy density in the cavity [13]. A random number decides whether stimulated or spontaneous emission will occur. Statistical analysis of the final velocities gives *both* the deceleration as well as the transverse diffusion of the atoms. By omitting the stimulated emission in the Monte Carlo calculation we can trace the effect of stimulated diffusion.

In the Monte Carlo calculation we have taken input powers 3×2.5 and $3\times 40 \text{ mW}$ for the three cavities. The laser detuning is assumed to be $\delta = -2\pi \times 750 \text{ MHz}$, in accordance with the experimental results. The results of the calculation are shown as a function of the initial atomic velocity v in Figures 3a (the average final velocity) and 3b (the r.m.s. value of the deflection angle). The average final velocities in Figure 3a clearly demonstrate a broad initial velocity range being transformed to a narrow range of final velocities, $\approx v_f$. The width of this broad range, $v - v_f$, is called the *capture range* and is found to be $\approx 35 \text{ ms}^{-1}$ and $\approx 96 \text{ ms}^{-1}$ for the $3\times 2.5 \text{ mW}$ and $3\times 40 \text{ mW}$ cases, respectively. The capture range depends on both the interaction time in the cavity, $\approx L/v_f$, and the deceleration, $\approx v_{\text{recoil},\parallel} \Gamma/2$, with Γ the spontaneous emission rate. An upper estimate for the capture range is given by

$$(v - v_f)_{\text{max}} = (L\Gamma/2v_f) v_{\text{recoil}}, \quad (3)$$

which equals 152 ms^{-1} for three sections with $L=94.5 \text{ mm}$. Because an absorption-stimulated emission cycle does not contribute to the slowing process, Figure 3a is unchanged if stimulated emission is omitted in the Monte Carlo calculation.

As a result of the transverse diffusion the atoms are deflected over an angle $\theta = v_{\perp}/v_f$. The average deflection angle as a function of the initial velocity is shown in

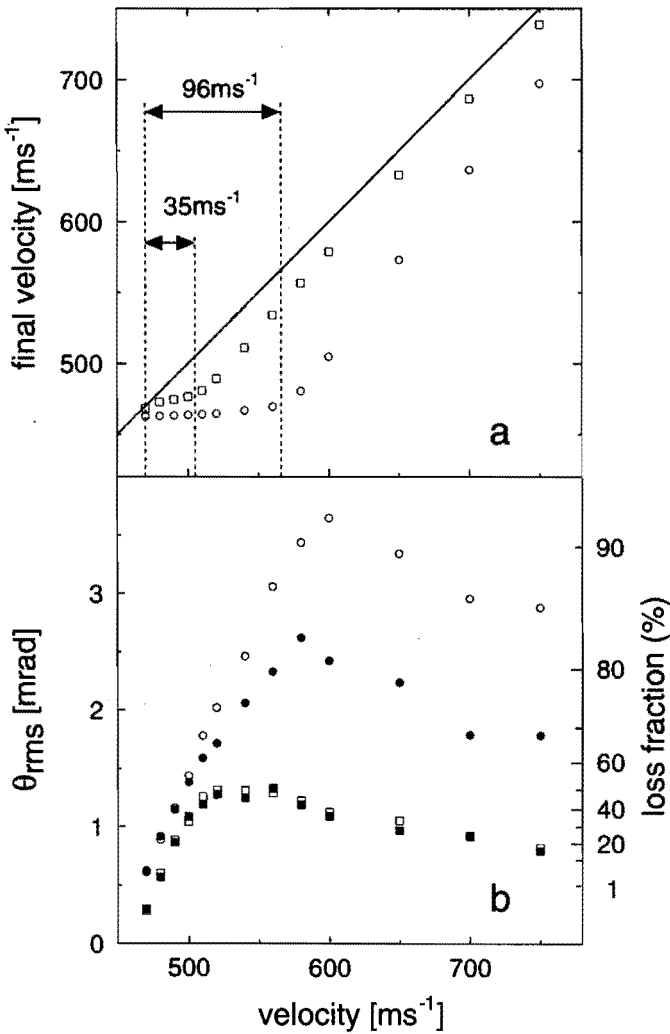


Figure 3: Monte Carlo calculation of a) the average final velocity and b) the r.m.s. value of the deflection angle versus the initial velocity. Shown are two input power calculations, $3 \times 2.5 \text{ mW}$ (squares) and $3 \times 40 \text{ mW}$ (circles). The capture range, which gives a 10 ms^{-1} wide v_f -range, has been indicated for both cases. The significant role of stimulated diffusion is demonstrated in Figure b. The deflection angle is calculated both with (empty markers) and without (filled markers) including the stimulated emission process. The right axis in Figure b gives the loss fraction of the atoms due to the final aperture (see Fig.1).

Figure 3b. The rectangular aperture, 1.5×4 mm, positioned 765 mm downstream of the isotropic slower results in a loss factor. This loss factor is calculated for each deflection angle and is shown on the right y-axis. Comparing Figs.3a and 3b we see that the position of maximum deflection corresponds to the fastest atoms just within the capture range. The resonance condition for these atoms results in a rather large initial angle θ , resulting in a fairly large contribution from stimulated diffusion ($\propto \sin^2 \theta$). For initial velocities above the capture range the angle θ becomes so large that the average photon recoil, $\hbar k \cos \theta / m$, is insufficient to slow the atom to the desired final velocity during the interaction time in the isotropic slower.

The importance of stimulated diffusion is also obvious from Fig.3b, where the results of the Monte Carlo calculation with and without stimulated emission are displayed. In the 3×2.5 mW case we observe a negligible difference. This indicates that spontaneous emission is the major driving force of the transverse diffusion for low laser power. However, for the 3×40 mW case there is an extra contribution of 1.0 mrad due to stimulated diffusion. This extra diffusion is also prominent within the capture range. Thus the advantage of an extended capture range through higher laser power has the negative side-effect of a large increase in transverse diffusion.

If the goal is to enlarge the capture range and simultaneously reduce transverse diffusion, one should maximize the number of absorption-spontaneous emission cycles and minimize the number of absorption-stimulated emission cycles. The number of cycles scales as $s/(s+1)$ for spontaneous emission and as $s^2/(s+1)$ for stimulated emission, with s the on-resonance saturation parameter as defined in a two level system. From the calculated intensity distribution $\Phi(z)$ the value of $s(z)$ is found to vary between $0.01 < s < 0.9$ and $0.2 < s < 15.3$ for the 3×2.5 mW and 3×40 mW cases, respectively. It is evident that the 3×40 mW situation is dominated by the absorption-stimulated emission cycles, with a correspondingly large contribution from stimulated diffusion.

An alternative manner to enlarge the capture range is by elongating the cavity. This could be implemented by using multiple cavity sections. The laser power per cavity section can now be chosen such that stimulated diffusion has a negligible effect. For large velocities in the capture range the resonance condition of Eq.1 results in large angles θ : to avoid the average photon recoil, $\hbar k \cos \theta / m$, from becoming too small, we might use different laser detunings in the various cavities thus keeping $\cos \theta$ as large as possible throughout the whole cavity as has been demonstrated by Ketterle et al.[7].

In a Monte Carlo calculation the final velocity distribution is simulated, using the initial distribution obtained with 'laser off' as input. Both the TOF velocity resolution and the finite solid angle acceptance of the detector have been taken into account. For the 3×10 mW case, the calculated distribution is compared with the experimental results in Fig.4. We observe good agreement for the slowed peak, but the loss of atoms is overestimated. It should be mentioned that the calculation is extremely sensitive

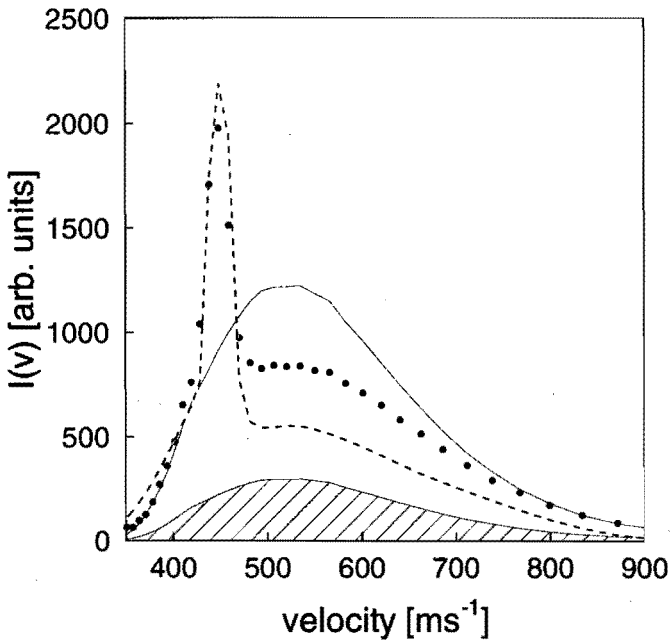


Figure 4: Three-section velocity distribution calculations with a detuning of $\delta = -720 (2\pi)\text{MHz}$. The thin solid line represents the initial distribution. The dashed line is the calculation for the $3 \times 10 \text{ mW}$ case; the experimental data are indicated by the dots. Again the hatched area represents the velocity distribution of the 25% metastable atoms which are unaffected by the laser light.

for the reflectivity of the cylindrical Spectralon cavity: an increase in reflectivity by $\approx 0.8\%$ results in a loss factor > 0.9 for velocities $v > 500$ m/s [8, 14].

This work demonstrates the isotropic slowing effect for Ne^* in a small cavity with low laser powers. Although papers [7, 8] stated that this could be a promising technique for beam slowing, the effect of transverse diffusion caused by stimulated emission can destroy the beam quality dramatically. In the experiment of Batelaan et al. [8] the perpendicular velocity resolution ($v_{\perp} \approx 2 \text{ ms}^{-1}$) is too large for this effect to be observable. In the experiment of Ketterle et al. [7] the perpendicular velocity is not resolved at all. Through a careful design of the cavity [14], the effect of transverse diffusion can be minimized. In the setup described above the saturation parameter still varies over fairly large range ($s_{\text{max}}/s_{\text{min}} \approx 20$). The laser light can be more evenly distributed along the z -axis, *e.g.* by illuminating the cylindrical cavity at more positions, spaced at closer intervals. Alternative ways of minimizing the transverse diffusion can be realized by illuminating the cylindrical cavity along the whole axis [15], or using a spherical cavity [16, 14]. In these cases, the intensity distribution in the cavity has no longer a peaked structure.

We wish to acknowledge helpful discussions with dr. H. Batelaan and dr. K.A.H. van Leeuwen. This work is financially supported by the "Stichting Fundamenteel Onderzoek der Materie" (Dutch Foundation for Fundamental Research on Matter (FOM)). The research of J.D. has been made possible by a fellowship of the Royal Netherlands Academy of Arts and Science.

References

- [1] W. Phillips, J. Prodan, and H. Metcalf, *J. Opt. Soc. Am. B.* **2**, 1751 (1985).
- [2] T. Barrett, S. Dapore-Schwartz, M. D. Ray, and G. Lafyatis, *Phys. Rev. Lett.* **67**, 3483 (1991).
- [3] V. Balykin, V. Letokhov, and V. Mishin, *Sov. Phys. JETP* **51**, 692 (1980).
- [4] W. Ertmer, R. Blatt, J. Hall, and M. Zhu, *Phys. Rev. Lett.* **54**, 996 (1985).
- [5] M. Zhu, C. Oates, and J. Hall, *Phys. Rev. Lett.* **67**, 46 (1991).
- [6] I. Littler, H.-M. Keller, U. Gaubatz, and K. Bergmann, *Z. Phys. D* **18**, 307 (1991).
- [7] W. Ketterle, A. Martin, M. Joffe, and E. Pritchard, *Phys. Rev. Lett.* **69**, 2483 (1992).
- [8] H. Batelaan, S. Padua, D. Yang, C. Xie, R. Gupta, and H. Metcalf, *Phys. Rev. A* **49**, 2780 (1994).

-
- [9] Labsphere Inc., P.O.Box 70, North Sutton, NH 03260, USA.
 - [10] M. Born and E. Wolf, *Principles of Optics* (Pergamon Press, Oxford, 1975).
 - [11] M. Hoogerland, Ph.D. thesis, Eindhoven University of Technology, The Netherlands, (1993).
 - [12] E. Kerstel, C. van Kruijsdijk, J. Vlugter, and H. Beijerinck, *Chem. Phys.* **121**, 211 (1988).
 - [13] R. Hilborn, *Am. J. Phys.* **50**, 982 (1982).
 - [14] T.G. Aardema, R.M.S. Knops, R.N.M. Vanneer, J.P.J. Driessen and H.C.W. Beijerinck, this thesis: chapter IV.
 - [15] H. Batelaan, private communication.
 - [16] T.G. Aardema, R.M.S. Knops, S.P.L. Nijsten, J.P.J. Driessen and H.C.W. Beijerinck, this thesis: chapter II.

Chapter IV

Slowing of $\text{Ne}^*(^3\text{P}_2)$ in Spectralon cavities: experiments

T.G. Aardema, R.M.S. Knops, R.N.M. Vanneer,
J.P.J. Driessen, and H.C.W. Beijerinck

*Physics Department, Eindhoven University of Technology,
P.O. Box 513, 5600 MB Eindhoven, The Netherlands*

Abstract

We present measurements of slowing an atomic beam of cold (180 K) metastable Ne^* atoms in monochromatic isotropic light cavities made of Spectralon. In combination with a 1D position-resolved time-of-flight experiment, both the axial and the transverse velocity component of the slowed atoms are determined. Short cavities ($L = 30 - 95$ mm) and low laser powers ($P = 2.5 - 80$ mW) are used. Distributing the laser input power over more optical cavities enhances the number of slowed atoms and reduces the transverse diffusion of the beam due to absorption-stimulated emission cycles. Comparing cylindrical and spherical cavity geometries, gives more insight into the slowing process. Comparison with a numerical model for the cooling proces shows discrepancies, that might be caused by lower values of the reflectance than expected.

1 Introduction

In the past few years, manipulation of neutral atomic beams has been investigated thoroughly [1]. A large variety of methods can be used for slowing, cooling, deflecting, trapping and/or focussing an atomic beam. Most of the techniques employ one or several directed laser beams and are based on the compensation of the Doppler offset experienced by the moving atoms. Some methods realize the Doppler compensation by either shifting the atomic frequency (Zeeman slowing [2, 3]) or the laser frequency (laser chirping [4, 5]). Additionally, white light slowing [6, 7] and isotropic monochromatic light slowing [8, 9] show to be promising techniques. Especially the isotropic light slower has the advantage of avoiding magnetic field gradients and simultaneously an on-axis laser beam, which may disturb beam-experiments downstream. Furthermore, laser power demands can be reduced and a simple implementation in an atomic beam line is possible.

In a near-resonant monochromatic isotropic light field with frequency ω_l , the atoms with a transition frequency ω_0 will absorb photons at an angle θ with respect to the atomic velocity v (see Fig. 1), satisfying the Doppler resonance condition

$$\begin{aligned}\omega - \omega_0 &= \omega_l - \omega_0 + kv \cos \theta \\ &= \delta + kv \cos \theta,\end{aligned}\tag{1}$$

with $\delta = \omega_l - \omega_0$ the laser detuning and k the magnitude of the wave vector. The corresponding velocity change, $v_{\text{recoil}} = \hbar k/m$, has components *both* parallel ($\cos \theta$) and perpendicular ($\sin \theta$) to the atomic velocity \vec{v} . The parallel component is utilized for slowing the atomic beam.

In this paper we want to determine the efficiency of laser cooling in an isotropic light field. To measure this isotropic slowing, a beam of metastable Ne^* atoms at 180 K is passed through an optical cavity, in which the monochromatic isotropic light field is realized using a single laser beam as input. Downstream of this cavity we perform a one-dimensional(1D) position resolved time-of-flight experiment. The influence of the cavity geometry has been studied by comparing a cylindrical optical cavity with a spherical one. Moreover, we have tripled the interaction time of the atoms in the isotropic light field by lining up three cavities in series. In addition, we have changed the laser frequency detuning for each individual cavity in order to maximize the total slowing effect. Finally, a blue-detuned laser beam is employed to study acceleration of an atomic beam. The experimental velocity distributions are compared with Monte Carlo simulations [10] (see chapter II), enabling us to unravel the dynamic processes involved in the isotropic cooling process in the optical cavity for different geometries.

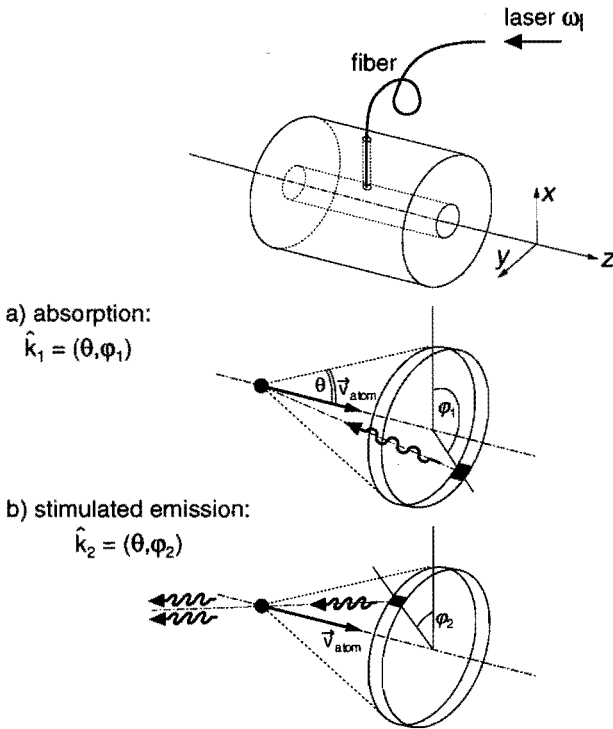


Figure 1: Cylindrical isotropic slower with laser light coupled into the cavity by using a fiber. An atomic beam enters the cavity in the z -direction and atoms absorb photons from a cone with top angle θ (panel a). The photon recoil parallel to the atomic velocity \vec{v} is cancelled by stimulated emission (panel b). The azimuthal angles of the absorbed and the emitted photon, φ_1 and φ_2 , result in a net velocity change of the atoms in the transverse direction.

2 Isotropic slowing

As a result of the Doppler effect, the recoil, $v_{\text{recoil}} = \hbar k/m$, experienced by a moving atom when absorbing a photon from an isotropic light field has components *both* parallel ($\cos \theta$) and perpendicular ($\sin \theta$) to the atomic velocity \vec{v} . The parallel component can be utilized for slowing the atomic beam. For red detuned light, $\delta < 0$, we find $0 < \theta < \pi/2$, meaning that the average photon recoil, $v_{\text{recoil},\parallel} = v_{\text{recoil}} \cos \theta$, opposes the atomic motion. Subsequent spontaneous emission results in a zero photon recoil on the average, and the atoms are slowed. As the atoms decelerate, the angle θ decreases until the minimum value of $\theta = 0$ is reached and the cone from which the atoms absorbs the photons becomes a 'spot'. This limit corresponds to a resonance atomic velocity $v_\delta = -\delta/k$. Because of the Lorentzian tail of the atomic linewidth, the atoms can even be slowed below the resonance velocity v_δ . However, the deceleration, which is proportional to the absorption rate given by the Lorentzian profile, decreases with a decreasing velocity ($v < v_\delta$) of the atoms.

The average force in the parallel direction of acting on an atom in an isotropic light field is equal to

$$F_z = m a = m a_0 \cos \theta, \quad (2)$$

with $a_0 = \hbar k S_{\text{spont}}/m$ the deceleration and S_{spont} the spontaneous emission rate. This force can be calculated in first order by using the Einstein rate equations, which are valid in an isotropic light field, resulting in

$$S_{\text{spont}} = \Gamma \frac{s}{2 + s \left(1 + \frac{g_g}{g_e}\right)}, \quad (3)$$

with s the saturation parameter, g_g and g_e the degeneracy factors of ground state and excited state, respectively, and Γ the atomic linewidth. The saturation parameter is calculated from the spectral density $\mathcal{U}(\omega)$ seen by the moving atom, which in its turn depends on the reflected light distribution along the walls of the cavity [10].

The maximum difference between initial and final velocity of an atom that can be obtained in a cavity with length L , is proportional to the interaction time Δt ($\approx L/v$) and the spontaneous emission rate S_{spont} . We define the 'capture range' Δv_{cap} as

$$\Delta v_{\text{cap}} \equiv (v - v_\delta)_{\text{max}} = (v_{\text{recoil},\parallel} \Delta t S_{\text{spont}})_{\text{max}} = v_{\text{recoil}} \frac{L}{v_\delta} S_{\text{spont}}. \quad (4)$$

The perpendicular component of the photon recoil, $v_{\text{recoil},\perp} = v_{\text{recoil}} \sin \theta$, is zero on the average. However, the statistical distribution of the azimuthal angle of the absorbed photons (φ_1 in Fig. 1) and the random nature of the spontaneous emission afterwards lead to an increase of the perpendicular velocity spread and contribute to the so-called transverse diffusion. If the absorption angle θ is small enough, the maximum value of the variance of the perpendicular velocity due to absorption-spontaneous emission

cycles N_{spon} is given by

$$\begin{aligned} \langle \Delta v_{\perp, spon}^2 \rangle &= N_{spon} v_{recoil}^2 \left\{ \frac{2}{3} + \langle \sin^2 \theta \rangle \right\}, \\ &= \left(\frac{\Delta v_{cap}}{v_{recoil}} \right) v_{recoil}^2 \left\{ \frac{2}{3} + \langle \sin^2 \theta \rangle \right\}, \end{aligned} \quad (5)$$

with the factor $\frac{2}{3}$ caused by the spontaneous emission and the $\sin^2 \theta$ term caused by the absorption.

Additionally, the absorption-stimulated emission cycle has to be taken into account in isotropic light slowing. As shown in Fig. 1, stimulated emission by a resonant photon from the cone cancels the slowing effect of the absorbed photon ($\Delta v_{\parallel, abs} = -\Delta v_{\parallel, stim}$). However, in general the two photons involved have a different azimuthal angle. This results in an extra transverse velocity change, $\Delta v_{\perp, stim} = 2 v_{recoil, \perp} |\sin((\varphi_1 - \varphi_2)/2)|$, and contributes to the transverse diffusion. We will refer to this extra transverse diffusion as stimulated diffusion. The corresponding variance is defined as

$$\langle \Delta v_{\perp, stim}^2 \rangle = N_{stim} \langle \Delta v_{\perp, stim}^2 \rangle_{\varphi}, \quad (6)$$

with N_{stim} the total number of absorption-stimulated emission cycles, determined by the absorption-stimulated emission rate $\mathcal{S}_{stim} = \mathcal{S}_{spon} s/2$ multiplied by the maximum interaction time L/v_{δ} . Substituting Eq. (4) in Eq. (6) results for a large saturation parameter s in,

$$s \gg 1: \quad \langle \Delta v_{\perp, stim}^2 \rangle = \left(\frac{s}{2} \right) \left(\frac{\Delta v_{cap}}{v_{recoil}} \right) v_{recoil}^2 \langle \sin^2 \theta \rangle. \quad (7)$$

3 Experimental setup

3.1 Beam machine

The Ne^* atoms are produced in a discharge-excited supersonic expansion, cooled by liquid nitrogen to an effective temperature of $T_{\parallel} \approx 180$ K [11] corresponding with a mean velocity $v_{\parallel} \approx 560$ ms^{-1} and a velocity spread of $\Delta v_{\parallel} \approx 130$ ms^{-1} . To measure the influence of an isotropic light field on both the axial (\parallel) and perpendicular (\perp) velocity distribution of a metastable Ne^* beam passing through the optical cavity we use the time-of-flight method (TOF) together with a position dependent metastable atom detector.

The TOF technique is used to determine the axial velocity v_{\parallel} . The time-of-flight distribution is measured with a mechanical chopper in combination with the metastable atom detector, located 714 mm and 1855 mm downstream of the isotropic slower, respectively. The velocity resolution, $\Delta v_{\text{TOF}} = 14$ ms^{-1} at $v_{\parallel} \approx 500$ ms^{-1} , is determined by the channel time ($\Delta t = 50$ μs) of the multiscaler and the open time of the chopper

($\Delta t = 40 \mu\text{s}$). Simultaneously, the perpendicular velocity v_{\perp} is determined with a position resolving detector. The resolution, $\Delta y \approx 50 \mu\text{m}$, determines the detection angular resolution of the slowed atoms: $\Delta\theta \approx 0.027 \text{ mrad}$.

A schematic representation of the beam apparatus is shown in Fig. 2. The atomic

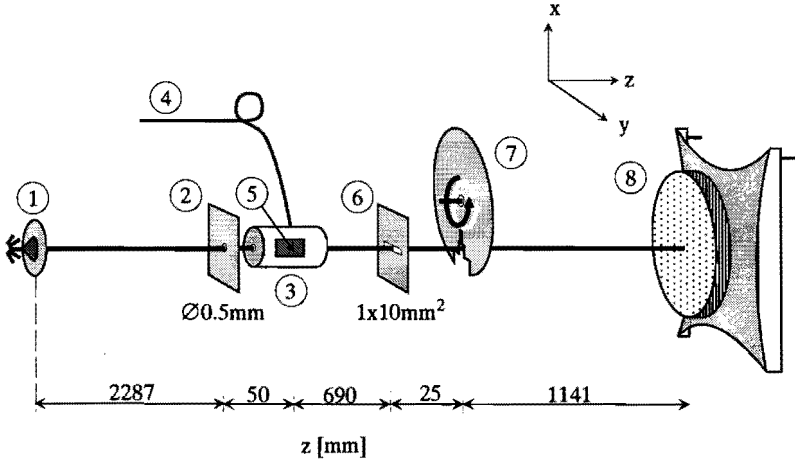


Figure 2: TOF experimental setup with a position resolving detector. 1) LN_2 cooled Ne^* beam source, 2) circular aperture, diameter 0.5 mm, 3) cylindrical or spherical Spectralon cavity, maximum three sections in line, 4) multimode fiber, 5) photo-diode for measuring the input power, 6) $1 \text{ mm} \times 10 \text{ mm}^2$ aperture, 7) mechanical chopper disk, 8) Micro Channel Plate stack with resistive anode serving as 1D position-resolving detector.

beam entering the cavity is collimated to $\theta_{\text{in,FWHM}} \approx 0.22 \text{ mrad}$, *i.e.*, a perpendicular velocity spread $\Delta v_{\perp} \approx 0.05 \text{ ms}^{-1}$. Subsequently, a rectangular aperture $1 \times 10 \text{ mm}^2$ in front of the chopper is used to determine the transverse diffusion in one dimension. This aperture corresponds to a total angular acceptance of $\theta_{\text{det,FWHM}} = 14.4 \text{ mrad} \approx 70 \theta_{\text{in,FWHM}}$.

3.2 Isotropic light cavity

The optical cavity is made of cylindrical sections of Spectralon [12], a material which perfectly isotropically reflects (Lambertian distribution [13]) with a reflectance of $\mathcal{R} \approx 0.99$. The outer diameter of a Spectralon rod is 32 mm. There are two different cavity setups: a cylindrical and a spherical geometry (Fig. 3). The length of a single cylindrical section is $L = 31.5 \text{ mm}$ and the diameter of the bore is $D = 1.5 \text{ mm}$. A spherical section, implemented in a cylindrical Spectralon rod, has a radius of $R = 8 \text{ mm}$ and on either side two short cylindrical cavities, each with a length of $L = 9.5 \text{ mm}$ and a bore diameter of $D = 1.5 \text{ mm}$. Thus, the effective length of the spherical setup

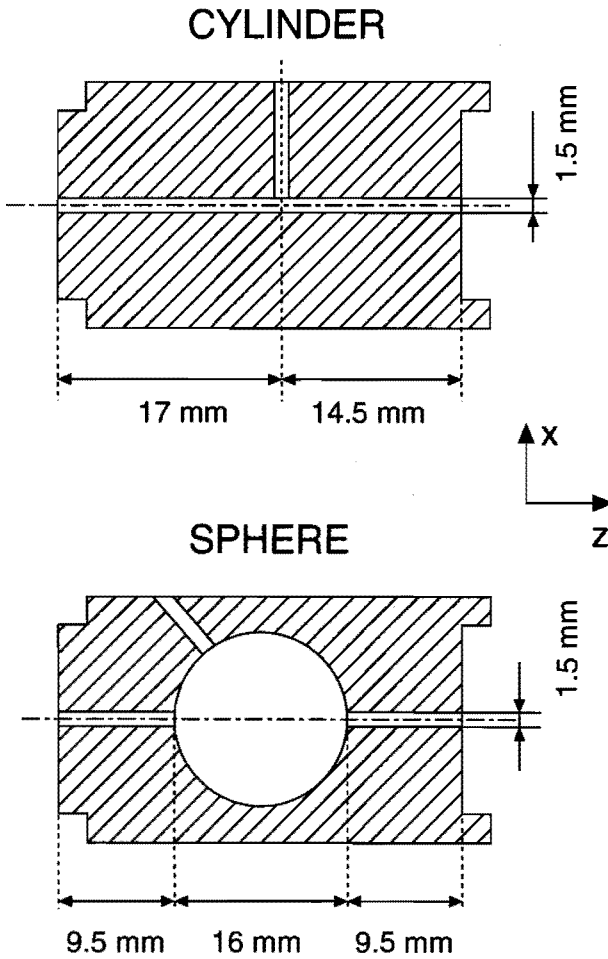


Figure 3: Schematic representation of the cylindrical and spherical optical cavities.

is $L_{\text{eff}} = 35$ mm. Up to three cavity sections can be lined up, enlarging the cavity length. Light is coupled into each cavity section halfway using a multimode optical fiber (Fig. 1). A photo-diode, mounted on the outside of the Spectralon cavity, is used to monitor the laser input power P .

The intensity distribution $\Phi_w(z) = W(z) \cdot P$ of the laser light which is being reflected on the cavity walls is calculated with a Monte Carlo method as described in chapter II [10]. For each photon entering the cavity the axial distribution of the number of reflections along the cavity wall is simulated, resulting in the so-called wall reflection density $W(z)$. Figure 4 shows the results for this wall reflection density $W(z)$ for both the cylindrical and spherical cavity setup. In case of the spherical setup, the

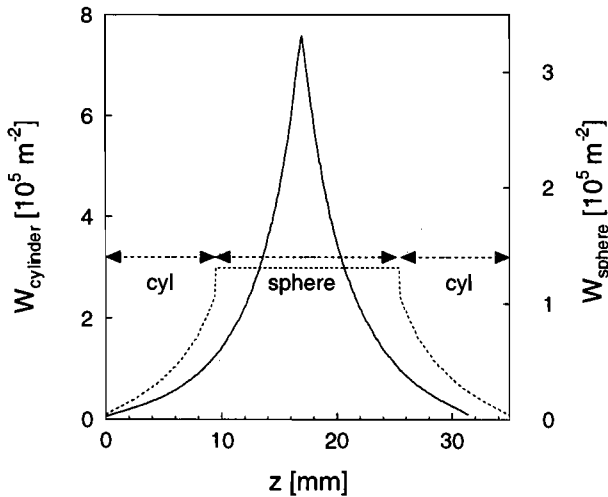


Figure 4: Wall reflection density $W(z)$ of the cylindrical (solid line) and spherical (dashed line) optical cavities (see text). The reflectance of the cylindrical setup and the cylindrical entrance and exit sections of the spherical setup is $\mathcal{R}=0.968$. The spherical part has a reflectance of $\mathcal{R}=0.990$. Values of the $W(z)$ distribution are depicted on the left and right y-axis for the cylindrical and spherical setup, respectively.

light distribution does not depend on the axial position z of the atom in the spherical part of the cavity. However, in the cylindrical cavities on either end, the light intensity varies with the axial position. The discontinuities in the wall reflection density $W(z)$ at the boundaries between the spherical and cylindrical cavities are caused by the abrupt change in the solid angle, observed by a wall element, with a corresponding change in the incident photon-flux. Differences in magnitude between the two setups are caused by the different geometries. To create the same average wall intensity $\Phi_w(z)$ in both cases, about a factor 2.3 more laser power should be used in the spherical cavity setup.

Note that the reflectance \mathcal{R} of the Spectralon material strongly depends on the

geometry of the cavity [14]. For the spherical cavity we use the reflectance data $\mathcal{R} = 0.990$ for a flat slice of Spectralon as reported by the manufacturer [12]. However, for the cylinder we use the simulated reflectance $\mathcal{R} = 0.968$ given by Van Benthem et al. [14]. They showed that a change of the inner radius R_1 from 0.5 mm to 1 mm, for a cylinder with infinite length and wall thickness of 15.25 mm, results in a relative change of 0.5% in the reflectance. This may result in a large change of the wall intensity distribution $\Phi_w(z)$, because this distribution critically depends on the factor $(1 - \mathcal{R})^{-1}$. Finally, it is likely that the reflectance is very sensitive to contamination of the Spectralon material [12].

3.3 Laser equipment

For our experiment we use the two-level transition $\text{Ne}^*(3s;^3P_2) \rightarrow \text{Ne}^{**}(3p;^3D_3)$ at $\lambda = 640.225$ nm with a lifetime of $\tau = 19.4$ ns, *i.e.*, $\Gamma = 8.2 (2\pi)$ MHz. A Coherent Innova 70 Argon Ion pump laser and a Spectra-Physics 380D ring dye-laser operating on DCM [15] provide the monochromatic light. Saturated absorption at the atomic frequency ω_0 is used to calibrate the laser frequency ω_l . The laser frequency is locked to an electronically controlled external cavity, with a frequency offset ($\delta = -k\nu_\delta$) controlled by an external voltage. No active long-term drift corrections for the laser frequency are made. The maximum frequency drift is estimated at ≈ 10 MHz/hour, which is acceptable in view of the typical timespan of 10 minutes needed to measure a velocity distribution.

Note that $^{20}\text{Ne}^*(^3P_0)$ and $^{22}\text{Ne}^*(^3P_0, ^3P_2)$, *i.e.*, 25% of the total beam flux, are not excited by the laser in the experiments.

4 Position-dependent detector

4.1 Hardware

The position resolving metastable atom detector consists of a stack of three Micro Channel Plates [16] with a diameter of 25 mm, in combination with a resistive anode. Each metastable atom causes an electron avalanche of approximately 10^7 electrons. A voltage of about 300 V is used to accelerate the released electrons to the anode. The pillow-shaped resistive anode (39×39 mm) results in a linear dependence of the resistive properties in the x - (or y -) direction when the pairs of outputs at the same x - (or y -) outer ends are connected together (Fig. 2). The ratio of the two electric pulses obtained at the outer edges can be transformed to a one-dimensional position. In our setup, the position is resolved in the y -direction. Additionally, the pulsed-mode operation of the detector allows for the time-of-flight technique to determine the parallel velocity distribution simultaneously.

To convert the pulse charges into information on position and time, an analog/digital electronic circuit is used. The analog part consists of a current-to-voltage converter, and the voltage can subsequently be used for AD-conversion. At the same time, the analog part generates signals for the synchronization of the digital part. Next, the digitized data are stored on a M68030-based computer system and further analyzed on a separate PC. Due to the time delay of the amplifiers in the analog circuit, the maximum count rate is limited to 10^4 Hz. The time-of-flight resolution of the detector is approximately $60 \mu\text{s}$ and the position resolution, determined by both the channel dimensions ($17 \mu\text{m}$) and the accuracy of the AD-conversion, is about $50 \mu\text{m}$. These resolutions are small enough for our experiments.

4.2 Measuring routine

For every experiment we make a choice for the cavity setup, the detuning and the input power of the laser beam. Each experiment is performed with a modulation technique, *i.e.*, measurements are performed both with laser ‘on’ and ‘off’, giving the position-resolved spectra $\mathcal{I}^{\text{on}}(y, t)$ and $\mathcal{I}^{\text{off}}(y, t)$. Because a large storage capacity is required for a single time-of-flight experiment, we have limited the maximum number of accumulated counts per spectrum to $5 \cdot 10^4$. The measuring time is inversely proportional to the count rate and is stored as well for each spectrum in order to compare the different arrangements. Drift in the production of Ne^* atoms can be neglected and laser ‘on/off’ measurements are carried out sequentially. Finally, after each experiment the frequency drift of the laser is checked using a Fabry-Perot cavity with a free spectral range of $\nu_{\text{FSR}} = 150$ MHz.

To compare the spectra $\mathcal{I}^{\text{on}}(y, t)$ and $\mathcal{I}^{\text{off}}(y, t)$ we have to correct for the various measuring times. In the laser ‘on’ situation some of the atoms do not reach the detector (deflection), in contrast with the laser ‘off’ situation. Assuming that the Ne^* production remains constant, the measuring time in case of laser ‘on’ will be longer than in case of laser ‘off’. Storing the total measuring time allows us to calculate the count rate. Therefore, we can compare the different spectra. During each experiment, the chopper frequency is measured in order to calibrate the starting time (t_0) of the time-of-flight measurement. Note that this calibration varies linear with the position y on the detector ($t_0 = t_0(0) + by$), because the chopper-slit takes a finite time to pass the diverging Ne^* beam (Fig. 2).

4.3 Beam measurements

A typical experimental result is shown in Fig. 5. Figure 5a and 5b depict the TOF and the beam profiles in the y -direction in a two-dimensional plot for a laser ‘on’ and ‘off’ situation. Clearly, the UV photons from the Ne^* source result in a peak at the start of the spectrum. This peak position determines the zero-point of the time

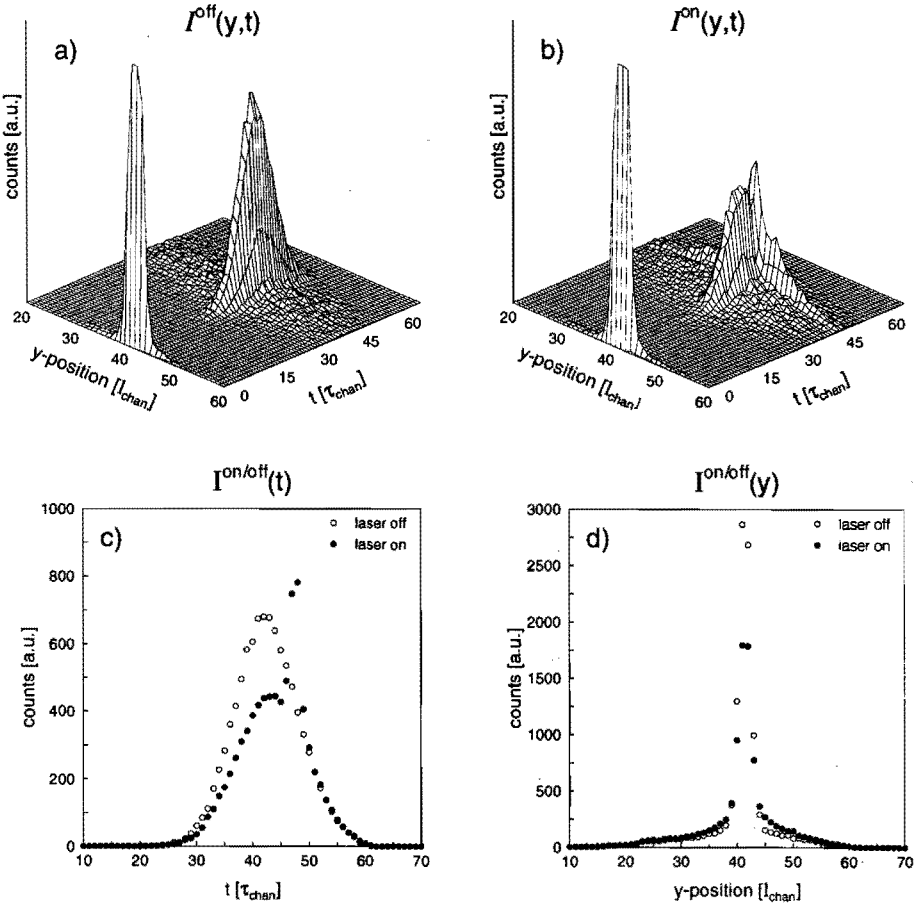


Figure 5: Typical example of a velocity resolved beam profile $I(y,t)$, for a three cylindrical cavity setup with 3×10 mW input power and a detuning of $\delta = -750$ (2π)MHz. a) TOF and y -position dependent information for the laser 'off' situation. b) idem for laser 'on'. c) position-accumulated time-of-flight spectrum for laser 'off' (\circ) and laser 'on' (\bullet). d) time-accumulated position spectrum in the y -direction for laser 'on' and 'off' (same as in c)).

scale of the spectrum. In the case of the laser ‘on’ situation (Fig. 5b), divergence due to transverse diffusion is clearly visible. The time resolution is $\tau_{\text{chan}}=50 \mu\text{s}$ and the position resolution is $l_{\text{chan}}=500 \mu\text{m}$ by summing over 10 adjacent channels (section 4.1). For the transformation of the y -position to a deflection angle, we define the deflection angles in cartesian coordinates (θ_x, θ_y) . Because of the 1D position-resolved measuring method for the y -direction, the transformation from y -position to deflection angle θ_y is given by

$$\theta_y = y \cdot 0.54 \frac{\text{mrad}}{\text{mm}}, \quad (8)$$

using the cavity-detector distance of 1855 mm as input (Fig. 2).

Summation over all time channels results in a position distribution

$$I(y) = \Sigma_t \mathcal{I}(y, t), \quad (9)$$

as shown in Fig. 5d. Important features are the wings on both sides of the central peak. For the laser ‘on’ situation the wings are larger due to transverse diffusion. Surprisingly, we also observe a significant contribution to the wings in the laser ‘off’ situation. This is caused by small angle scattering resulting from the large background pressure ($\approx 5 \cdot 10^{-6}$ Torr) in the vacuum vessel containing the Spectralon cavity.

Alternatively, summation over all y -positions gives the time-of-flight spectrum

$$I(t) = \Sigma_y \mathcal{I}(y, t), \quad (10)$$

as depicted in Fig. 5c.

5 Cylindrical cavity

5.1 Varying the laser power P

We first investigate the force of an isotropic light field on moving atoms in different geometries; we start out with a cylindrical cavity and proceed with the spherical cavity (section 3.2). As discussed in section 3, the velocity change in the axial direction of the atoms (v_{\parallel}) can be measured simultaneously with the spatial change of the atomic beam (v_{\perp}) in one direction. In Fig. 6a the measured velocity distributions are shown for three different laser powers. For all three power settings the laser detuning is adjusted to $\delta = -765 (2\pi)\text{MHz}$, corresponding to a resonance velocity $v_{\delta}=490 \text{ms}^{-1}$. Two pronounced features are visible in all cases. First, a peak of slowed atoms can be seen which is shifted $\approx -2\Gamma/k$ to the left of the resonance velocity v_{δ} . The shift is due to off-resonance slowing, because there is no accelerating force for velocities $v < v_{\delta}$. Secondly, we observe that the total flux reaching the detector (summed over time and position channels, $\Sigma_{y,t} \mathcal{I}(y, t)$) is smaller for the laser ‘on’ situation. For larger input powers this decrease in measured flux becomes even more pronounced. This is due to

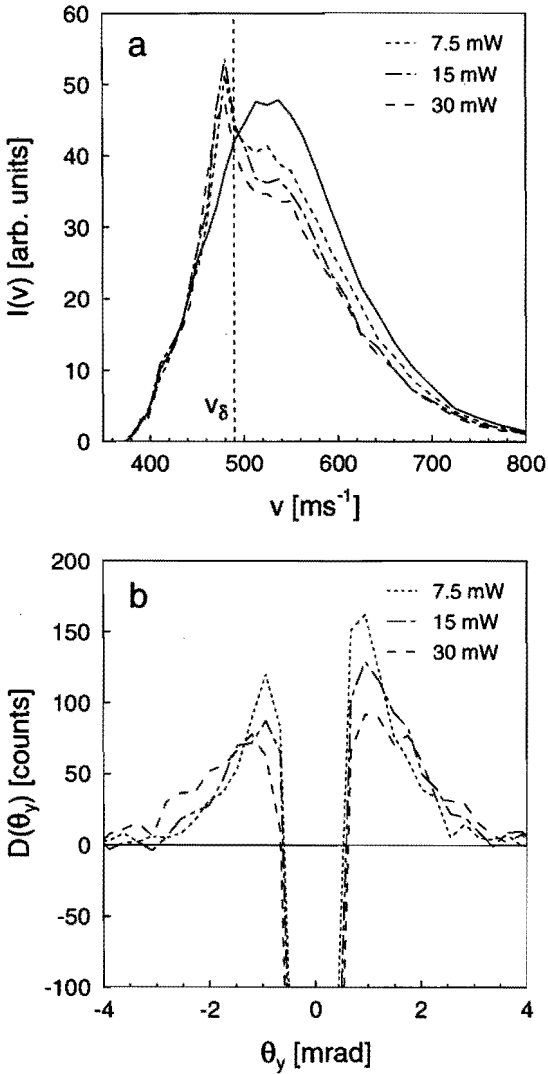


Figure 6: Experimental velocity spectra (panel a) and difference between the position spectra of laser 'on' and 'off' (panel b), for one cylindrical cavity. The detuning is $\delta = -765 (2\pi)\text{MHz}$ and the laser input powers are: 7.5, 15 and 30 mW. In panel a) the initial distribution is indicated by a solid line.

transverse diffusion, both spontaneous and stimulated, as discussed in the introduction. To check this assumption we have plotted in Fig. 6b the difference spectrum

$$D(y) = I^{\text{off}}(y) - I^{\text{on}}(y), \quad (11)$$

summed over all time channels and suppressing the light peak. In this way only the atoms which interact with the laser light are visible. From the shape of the wings for the three laser powers we conclude that the atoms are deflected over larger angles in case of higher input powers.

The finite solid angle acceptance of the position sensitive detector is responsible for the discrepancy in the flux reaching the detector. Moreover, it can also explain the increase in loss of flux for higher input powers. Apparently, the increase of the capture range for large input powers (Eq. (4)) does not contribute to an increase of the slowed peak due to the larger average divergence of the atoms passing the optical cavity. To investigate this we will have a closer look at Fig. 6b. The wings suggest a gaussian type distribution. In view of the definition of the cartesian deflection angles θ_x, θ_y (section 4.3) this would imply the following distribution

$$P(\theta_x)P(\theta_y)d\theta_x d\theta_y = \frac{1}{\sigma_x \sigma_y} \frac{1}{2\pi} e^{-\frac{1}{2}(\theta_x/\sigma_x)^2} e^{-\frac{1}{2}(\theta_y/\sigma_y)^2} d\theta_x d\theta_y, \quad (12)$$

with σ_x and σ_y the angular spread for the x - and y -direction. As discussed in section 3, the position information is only resolved for the y -direction. Thus, integrating over the x -coordinate results in,

$$P(\theta_y)d\theta_y = C e^{-\frac{1}{2}(\theta_y/\sigma_y)^2} d\theta_y. \quad (13)$$

This distribution would be the correct description of the experimental data with C a scaling factor. In principle, the angular spread σ_y can be obtained from the second-order moment of this distribution.

However, the difference spectrum, $D(y)$ (Fig. 6b), has a gap for $|\theta_y| < \theta' \approx 0.7\text{mrad}$. Therefore, we calculate an alternative angular spread as follows

$$\sigma_{\text{eff}}^2 = \frac{\int_{|\theta_y| > \theta'} (|\theta_y| - \theta')^2 D(\theta_y) d\theta_y}{\int_{|\theta_y| > \theta'} D(\theta_y) d\theta_y}. \quad (14)$$

This procedure can be applied to the distribution of Eq. 13, enabling us to compare experimental results with the Monte Carlo simulations. For an angular spread $\sigma_y > \theta'$, this results in an effective spread $\sigma_{\text{eff}} \approx \sigma_y$, with an error less than 10%, whereas for $\sigma_y \ll \theta'$ we find $\sigma_{\text{eff}} \approx \theta'$. In our case the relation $\theta' \geq \sigma_y$ always holds.

Because of the limited number of total counts ($5 \cdot 10^4$) for both the laser 'on' and 'off' spectra, the statistical accuracy of the difference spectrum is not sufficient. Only one experiment with a laser detuning $\delta = -660 (2\pi)\text{MHz}$ was repeated several times.

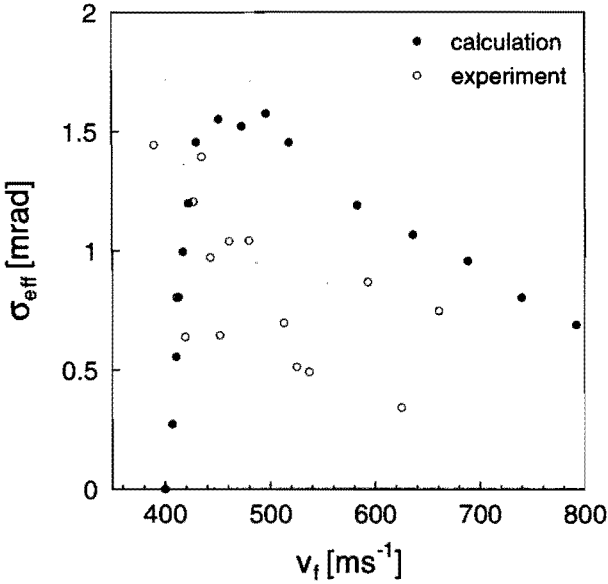


Figure 7: Angular spread according to Eq. (14) as a function of the final velocity v_f . The laser frequency detuning is $\delta = -660$ (2π)MHz and the input power is $P=30$ mW. The open symbols (\circ) denote experimental results whereas simulated data are indicated by the filled symbols (\bullet).

providing us sufficient accuracy to confront the experiment with theoretical simulations. Figure 7 compares the experimentally determined angular spread according to Eq. (14) with the simulations. The large scatter in the experimental data is indicative for the poor statistical accuracy. It is obvious that the simulations overestimate the angular spread. However, both experiment and theory show a decreasing trend for increasing final velocities v_f .

5.2 Varying the resonance velocity v_δ

To show the effect of various laser detunings δ on the velocity distribution, we have chosen three different values for δ : -450 , -600 and -750 (2π)MHz. These values correspond to resonance velocities of $v_{\delta_1}=288$, $v_{\delta_2}=384$ and $v_{\delta_3}=480$ ms $^{-1}$, respectively. The resulting velocity distributions are depicted in Fig. 8. All three experimental distributions are measured with a laser power of $P=30$ mW. For the largest resonance velocity v_δ we observe a distinct peak of slowed atoms. For $\delta_2 = -600$ (2π)MHz the effect of slowing is less pronounced. This is due to the smaller number of available atoms that can reach the resonance velocity, given by the finite capture range Δv_{cap} .

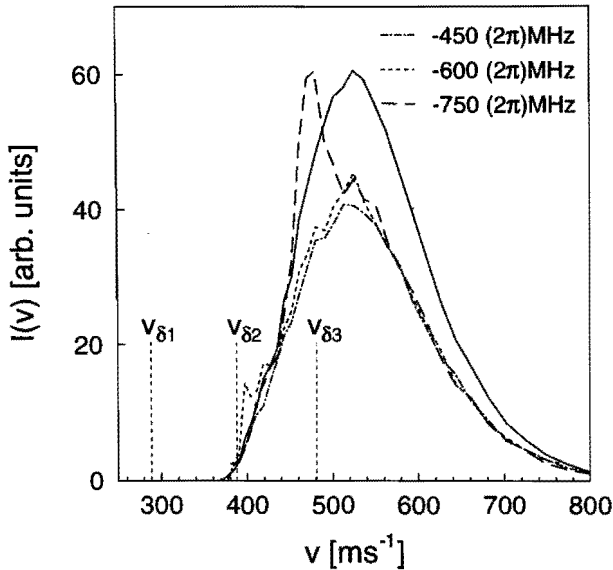


Figure 8: Velocity distributions for a single cylindrical cavity with an input power of $P=30$ mW and detunings δ of -450 , -600 and -750 (2π)MHz as indicated in the figure. The solid line represents the initial velocity distribution.

For $\delta_1 = -450$ (2π)MHz no slowed peak is visible at all. The atoms are slowed but the capture range is obviously too small to overlap significantly with the initial velocity distribution. Therefore, only a negligible fraction of the atoms can reach the resonance velocity $v_{\delta_1}=288$ ms^{-1} . A difference in initial and final velocity distribution is evident due to laser interaction with the atomic beam causing a transverse diffusion of the beam and resulting in a loss of atoms reaching the detector.

To confirm the above explanations we calculated the r.m.s. value of the beam divergence σ_y denoted by σ_θ . The results are shown in Fig. 9. In these calculations only the resonance velocity v_δ changes. Clearly visible is the increase in σ_θ for smaller values of $|\delta|$, while σ_θ remains constant for the high velocity tail. This constant value for σ_θ for high velocities is caused by the fact that all the atoms nearly see the same wall intensity. In the case of $v \geq 2v_\delta$ the resonance angle θ is already larger than 60° , resulting in a delta function of the atomic linewidth projected on the cavity wall. Therefore, the same absorption, stimulated emission and spontaneous emission rates occur and consequently, nearly the same angular spread σ_θ . The increase in σ_θ for lower velocities is due to the increasing traveling time through the optical cavity for lower velocities. This results in a larger beam divergence and a decreasing fraction of atoms reaching the detector. This explains the features in Fig. 8: decreasing slowed atom peak height and the nearly constant shape of the velocity distribution between

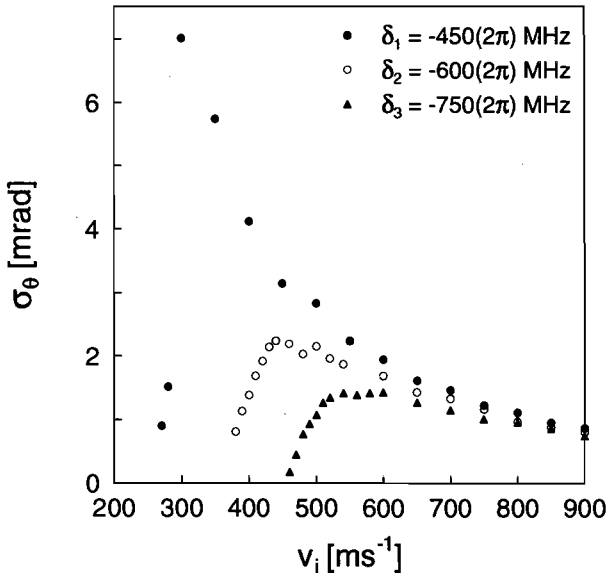


Figure 9: Calculated r.m.s beam divergence σ_θ as a function of the initial velocity v_i . The detunings are $\delta_1 = -450$, $\delta_2 = -600$ and $\delta_3 = -750$ (2π)MHz, laser power $P=30$ mW and reflectance $\mathcal{R}=0.968$.

$v=440$ and 500 ms $^{-1}$ for different detunings.

5.3 Simulated TOF distribution

From the simulations we obtain data for both the axial deceleration and the transverse diffusion. Combination with the finite solid angle acceptance of the metastable atom detector enables us to construct the final velocity distribution as measured with the experimental setup [10]. This results in a slowed peak slightly below v_δ . Finally, the TOF velocity resolution (14 ms $^{-1}$) is taken into account (section 3), giving a simulated experimental velocity distribution which can be directly compared with the experimental results. In Fig. 10 an experimentally determined velocity distribution is depicted together with two simulations. The solid angle acceptance is determined by a rectangular aperture of 1×10 mm 2 in front of our 2 D detector. However, the finite diameter (0.5 mm) and angular spread (0.22 mrad) of the atomic beam entering the optical cavity have not been taken into account in the simulations. Therefore, we have also analyzed the simulated data with a slightly different aperture, 1.5×10 mm 2 , to give more insight in the simulated slowing process. Note that this aperture value is not a correction for not convoluting the atomic beam with the finite aperture. The reflectance chosen is $\mathcal{R} = 0.968$ and an input power is used of $P=30$ mW.

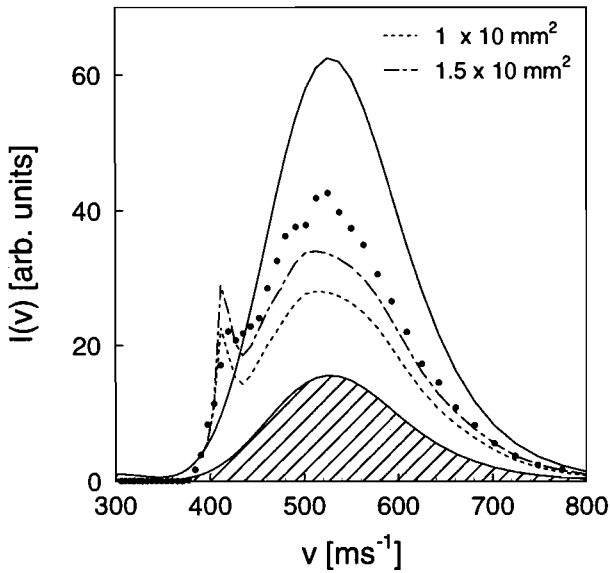


Figure 10: Experimental and simulated velocity distribution with a laser detuning of $\delta = -660 (2\pi)\text{MHz}$. The initial velocity distribution (laser 'off') is indicated by the solid line, whereas the final distribution (laser 'on') is represented by the filled circles (\bullet). Two simulated velocity distributions are depicted, obtained with different apertures in front of the detector: $1 \times 10 \text{ mm}^2$ and $1.5 \times 10 \text{ mm}^2$. The reflectance of the optical cavity is assumed to be $\mathcal{R}=0.968$ and the experimental laser input power is $P=30 \text{ mW}$. The hatched area represents the velocity distribution of the 25% metastable atoms which are unaffected by the laser light.

The two simulations overestimate the slowing effect, *i.e.*, the simulated slowed peak is larger than the experimental peak. Moreover, the total flux reaching the detector is lower for the simulated spectra. Obviously, the simulations seem to overrate the slowing process both for the axial velocity component and for the beam divergence (Fig. 7). In the next section we will focus on some possible causes.

5.4 Transverse diffusion exclusively, $\delta = 0$

More information about the transverse diffusion can be obtained by eliminating the axial deceleration. This can be realized by choosing a zero detuning ($\delta = 0$) for the laser frequency. In that case the photons are absorbed from an angle $\theta \approx \pi/2$. Therefore, the average photon recoil in the axial direction is zero for all processes involved: absorption, spontaneous emission and stimulated emission. However, the diffusion in the transverse and the axial direction is not switched off. In our setup we can directly measure the perpendicular velocity spread $\langle \Delta v_{\perp}^2 \rangle$, which results from the transverse diffusion. The difference spectrum $D(t(v))$,

$$D(t(v)) = I^{\text{off}}(t(v)) - I^{\text{on}}(t(v)), \quad (15)$$

represents the deflected atoms which do not reach the detector anymore. The resulting loss fraction $f(t(v))$, as defined by

$$f(t(v)) = D(t(v))/I^{\text{off}}(t(v)), \quad (16)$$

can be compared with theoretical predictions obtained by convoluting the simulated beam divergence with the solid angle acceptance of the detector (section 3.1). In Fig. 11 the simulated and experimental loss fractions are plotted as a function of the axial velocity v . Again, the simulations overestimate the total number of absorptions as indicated by the larger loss fractions.

This experiment can be regarded as the ultimate check as to whether the simulation and/or circumstances under which the experiment is performed are correct. In the first place, the results between experiment and calculation improve drastically when the laser power P is decreased by more than a factor 6. This change cannot be explained by the errors ($\pm 10\%$) of the measurements of the laser power. On the other hand, this change would imply that the reflectance of the Spectralon data is incorrect. Scaling the enhancement factor $\approx (\mathcal{R}/(1 - \mathcal{R}))$ of the cavity by a factor 6 would result in a decrease of the reflectance of $\mathcal{R} = 0.968$ down to $\mathcal{R} = 0.802$. This value is not realistic when comparing with the data reported by the manufacturer [12] and calculations performed by Van Benthem et al. [14]. Note that changing the reflectance value also causes a smaller effective cavity length (see chapter II). Thus, causes an extra decrease in absorption-spontaneous and absorption-stimulated emission cycles, resulting in a too small loss fraction. Therefore, the estimate of the reflectance $\mathcal{R} \approx 0.8$ is the lower limit.

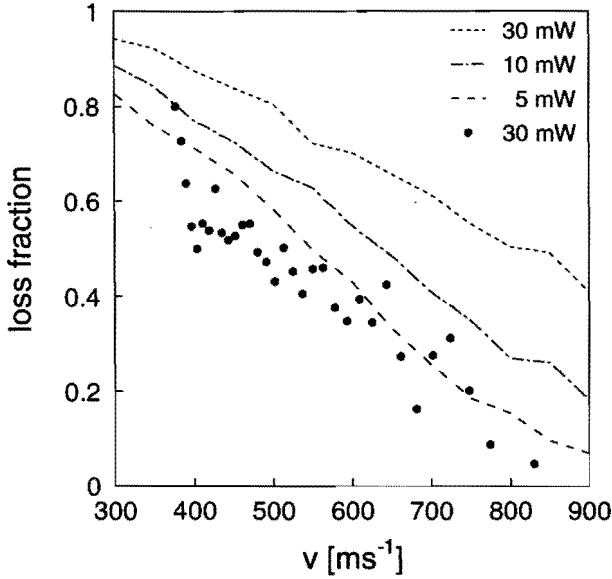


Figure 11: Loss fraction due to transverse diffusion as a function of the atomic velocity v . The experimental (\bullet) and simulated data (see figure) of the loss fraction are shown for a laser detuning $\delta=0$ MHz, different laser powers and a reflectance $\mathcal{R}=0.968$. In this case we no longer observe an axial slowing effect and the loss fraction is solely due to beam divergence caused by transverse diffusion.

Furthermore, the material Spectralon is very sensitive to contamination, which could explain a possible decrease in reflectance \mathcal{R} . However, no reactive gases which could diminish the reflectance are used in this experiment, except for oil of the used pumps in our apparatus. No checks were made in our experiment to verify any possible contamination. Another possible explanation could be the finite beam aperture in front of the Spectralon cavity but this is of minor importance with respect to the above mentioned statements. Although there still is a discrepancy between experiment and simulation, the calculations give a qualitatively good view of the slowing process in an isotropic light field.

6 Spherical cavity

The deceleration of an atomic beam depends on the resonant part of the isotropic light field, *i.e.*, the photons which satisfy the Doppler resonance conditions of Eq. (1). The energy density distribution $\mathcal{U}(\omega; v, z)$ experienced by an atom moving with velocity v at position z in the cavity can be derived from the spatial distribution of

the light within the cavity. This distribution directly influences the total number of absorption-spontaneous emission and absorption-stimulated emission cycles. Therefore, it determines both the deceleration and the divergence of the atomic beam. The spatial light field can be determined from the calculated wall reflection density, $W(z)$, which has been depicted in Fig. 4 for both the cylindrical and spherical geometry [10]. Due to the peaked structure of $W(z)$ for the cylindrical cavity it is impossible to obtain a homogeneous energy density distribution $\mathcal{U}(\omega; v, z)$, which leads to a significant beam divergence for the cylindrical setup. However, in case of the spherical cavity this divergence can be minimized because $W(z)$ is flat for a large part of this cavity. Note that increasing the saturation parameter s , *i.e.*, switching from sphere to cylinder in this case, only results in more transverse diffusion while the deceleration remains constant.

The average value of the wall reflection density $\langle W(z) \rangle$ differs about a factor 2.3 for the cylindrical and spherical geometries. Accordingly, to compare experiments with the same average light intensity we need to scale the laser power by this factor. The slowing effect for the two different geometries has been measured with laser input powers $P = 30$ mW and 65 mW for the cylinder and sphere, respectively, and with

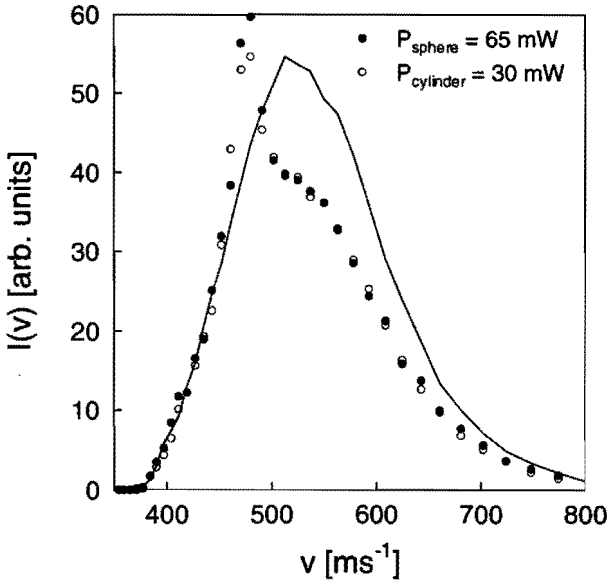


Figure 12: Experimental velocity distribution obtained for the cylindrical and spherical geometries. The detuning is $\delta = -750$ (2π)MHz. The input powers are $P=30$ mW for the cylindrical cavity (\circ) and 65 mW for the spherical cavity (\bullet). The solid line represents the initial distribution.

a laser detuning of $\delta = -750 (2\pi)\text{MHz}$. The experimental velocity distributions are shown in Fig. 12. In both cases we see a peak of slowed metastable Ne^* atoms and an overall loss of flux reaching the detector, indicated by the discrepancy between the laser 'on' and laser 'off' spectra, $I^{\text{on}}(t)$ and $I^{\text{off}}(t)$, respectively. The spherical cavity results in more decelerated atoms, indicated by the higher slowed peak. Furthermore, both setups have the same loss fraction for $v > 500 \text{ ms}^{-1}$, resulting in an identical final velocity distribution. Obviously, the estimated value 2.3 is not the correct scaling factor because the height of the slowed peaks is different. The actual deceleration is not proportional to the average intensity $\langle \mathcal{U}(\omega) \rangle$ but depends on the actual shape of the intensity distribution $\mathcal{U}(\omega; v, z)$. Unfortunately, we are unable to compare the angular divergence spectra for these cases due to poor statistical accuracy (section 4).

7 Multiple cavities

Deceleration and transverse diffusion are correlated aspects in isotropic light slowing of an atomic beam. For the design of a slower with a maximum deceleration and a minimum transverse diffusion, the absorption-spontaneous emission and absorption-stimulated emission should be optimized accordingly. Increasing the capture range Δv_{cap} by using more laser power does not solve the problem. As can be derived from section 2, the ratio of stimulated emission events and spontaneous emission events scales as

$$\frac{\mathcal{S}_{\text{stim}}}{\mathcal{S}_{\text{spont}}} = \frac{\Gamma s^2 / (4 + 2s(1 + \frac{g_s}{g_e}))}{\Gamma s / (2 + s(1 + \frac{g_s}{g_e}))} = \frac{s}{2}. \quad (17)$$

For higher s -values this results in a larger contribution of stimulated transverse diffusion, whereas hardly more spontaneous emission events occur. However, an alternative way to enlarge the capture range is by choosing a longer cavity (Eq. (4)). This could be implemented by using multiple cavity sections and reducing the laser power per cavity section.

For a large saturation parameter $s \gg 1$, with $\mathcal{S}_{\text{spont}} \approx \Gamma/2$, the capture range can be written as

$$\Delta v_{\text{cap}} = v_{\text{recoil}} \frac{L}{v_s} \frac{\Gamma}{2}. \quad (18)$$

For example, increasing the length of the cavity to $L' = 3L$ and decreasing the laser power to $P' = P/3$ and hence the saturation parameter by a factor three, results in an extended capture range

$$\Delta v'_{\text{cap}} \approx 3 \Delta v_{\text{cap}}. \quad (19)$$

Consequently, the transverse diffusion will increase. The perpendicular velocity spread due to absorption-spontaneous emission cycles, $\langle \Delta v_{\perp, \text{spont}}^2 \rangle^{1/2}$, increases by a factor $\sqrt{3}$ (Eq. (5)). This effect is inherent to slowing and can never be avoided. However, the velocity spread due to absorption-stimulated emission cycles, $\langle \Delta v_{\perp, \text{stim}}^2 \rangle^{1/2}$, remains

the same (Eq. (7)). A capture range a factor three larger (Eq. (19)) is cancelled by a factor three smaller saturation parameter. Finally, we expect a larger fraction of slowed atoms for a three times longer cavity and saturation parameter a factor three smaller, with still the assumption $s > 1$. From these simple scaling arguments we can conclude that enlarging the cavity and dividing the laser power over more optical cavities is more efficient.

To check whether the above statements are correct, we have calculated the slowing effect for a one and three-cylindrical cavity setup and compared the results with an experiment. First we discuss the calculated results. In Fig. 13 the deceleration Δv and the photon emission number (spontaneous and stimulated photons) are depicted for an input power $P = 1 \times 30$ mW and 3×10 mW in the case of a one and three-cylindrical cavity setup, respectively. The detuning is $\delta = -750$ (2π)MHz and the reflectance of the cavity is $\mathcal{R}=0.968$. In both cases the average saturation parameter s is larger than unity: for a single cavity $\langle s \rangle \approx 6$ and $\langle s \rangle \approx 2$ for a triple cavity. The deceleration curve and the photon emission curve show an increase by a factor two for the triple cavity setup in comparison with the single cavity. The calculated increase in the capture range is not equal to the simple scaling law given by Eq. (19). Clearly, the capture range is not a function of the average saturation parameter as used for the prediction, which in its turn is an upper limit. The capture range also depends on the shape of the wall reflection density, which determines the saturation parameter. Apart from changing the capture range, the changing number of spontaneous and stimulated emissions should be investigated. The number of spontaneous emissions N_{spont} in Fig. 13b increases by the same factor as the deceleration Δv . However, the number of stimulated emission N_{stim} events decreases slightly, which is beneficial. The influence on the divergence of the atomic beam, caused by the changing number of photon emissions, is depicted in Fig. 14. Clearly visible is the extra velocity spread of approximately 0.2 mrad for the triple cavity setup in comparison with the single cavity setup. This extra contribution is caused by additional spontaneous emissions (Fig. 13b).

Experimentally, the above two options for the cavity setup have been investigated in terms of the velocity distributions $I(v)$. The results are shown in Fig. 15. The velocity distribution for the three-cylinder cavity shows a larger number of slowed atoms than the one-cylinder case. This of course is due to the interaction time which is three times longer and the relatively small increase in the perpendicular velocity spread because of absorption-spontaneous emission. Therefore, relatively more atoms are decelerated to the resonance velocity v_g and reach the detector. In conclusion, both experiment and simulation show a more efficient slowing effect in the case of the triple cavity setup.

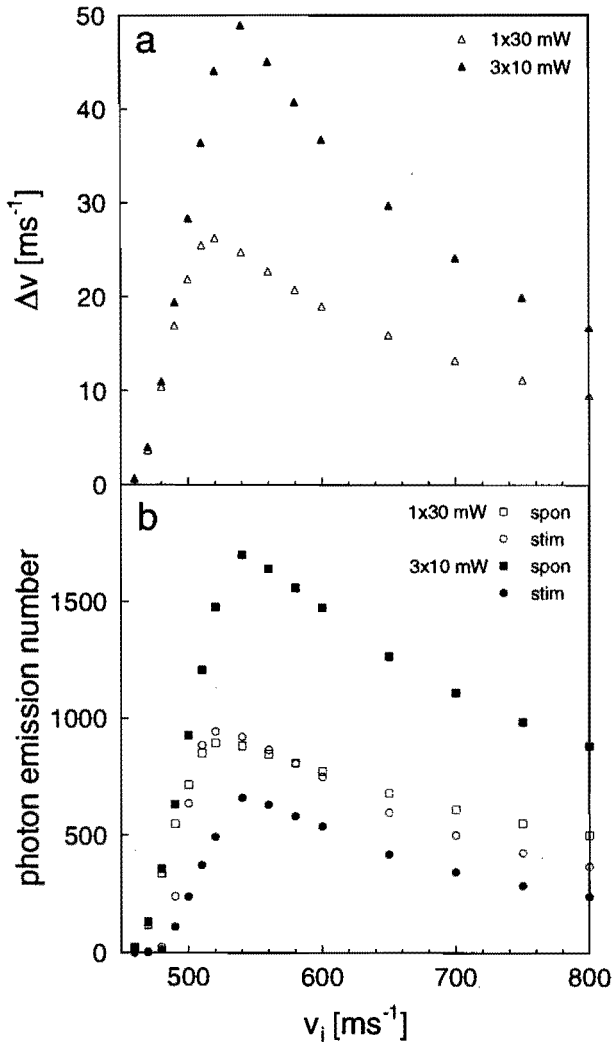


Figure 13: Calculated deceleration (a) and photon emission number (b) for the one and three-cylindrical cavity setup. The input power is $1 \times 30 \text{ mW}$ and $3 \times 10 \text{ mW}$, detuning $\delta = -750 (2\pi)\text{MHz}$ and the reflectance $\mathcal{R}=0.968$. The maximum deceleration increases by a factor 2 for the three cylindrical cavity setup and is in agreement with the total number of spontaneous emission events. The number of stimulated emissions, however, decreases for the three-cylindrical cavity setup in comparison with the single-cylindrical cavity. Note that Δv scales approximately with N_{spont} .

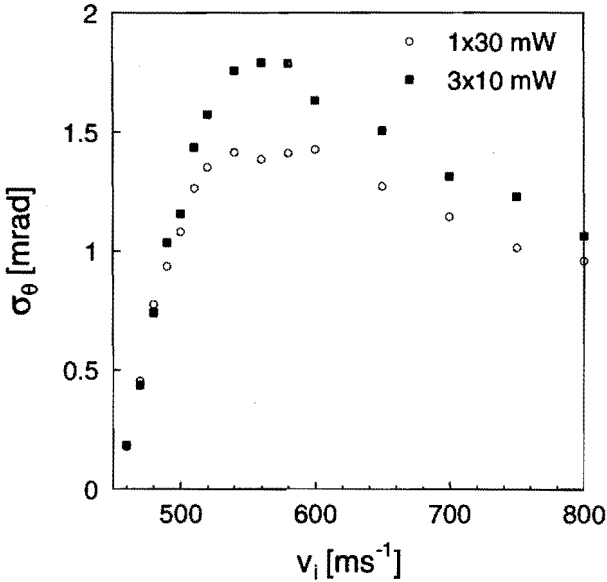


Figure 14: Perpendicular velocity spread σ_θ for the single and triple-cylindrical cavity setup (parameters see text). In the triple cavity setup an extra spread occurs due to the larger number of spontaneous emissions caused by an increase of the capture range by a factor two.

8 Special features

8.1 Multiple frequency slowing

Apart from dividing the input power over a longer cavity, which results in more decelerated atoms around the resonance velocity v_δ and less beam divergence or transverse diffusion, it is interesting to have a closer look at the capture range Δv_{cap} . For large velocities in the capture range, the resonance condition of Eq. (1) results in large absorption angles θ , and increases even more for larger capture ranges. To avoid the average photon recoil, $\hbar k \cos \theta / m$, from becoming too small and, accordingly, the perpendicular component $\hbar k \sin \theta / m$ too large, we may use different laser detunings in the various cavities. Thus, $\cos \theta$ is kept as large as possible throughout the whole cavity as has been demonstrated by Ketterle et al.[8]. Figure 16 shows the experimental results for the final velocity distribution using three-cylindrical cavities with detunings, $\delta = -830, -750$ and -670 (2π)MHz, realized by an acousto-optic modulator with a frequency shift $\Delta\nu = 80$ MHz. The frequency shift corresponds with a change in

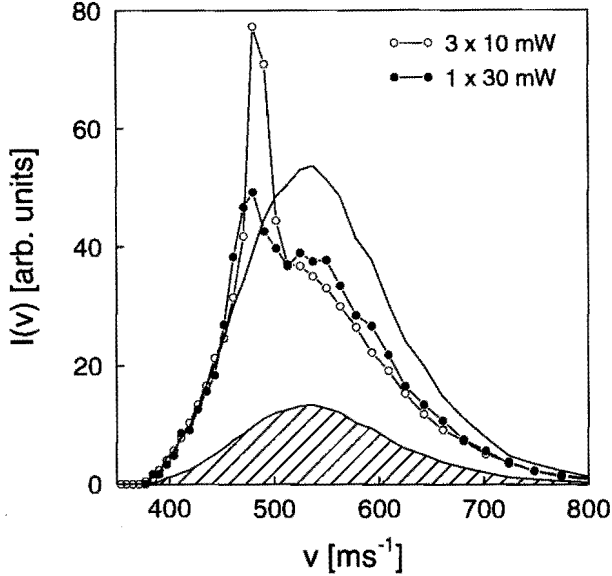


Figure 15: Experimental velocity distributions of an one and three-cylindrical section setup. The detuning is $\delta = -750 (2\pi)\text{MHz}$. The solid line represents the initial distribution and final distributions are indicated in the figure. Again the hatched area represents the velocity distribution of the 25% metastable atoms which are unaffected by the laser light.

resonance velocities of $\Delta v_\delta = 51 \text{ ms}^{-1}$, resulting in

$$\begin{aligned}
 v_{\delta,1} &= 531 \text{ ms}^{-1}, \\
 v_{\delta,2} &= v_{\delta,1} - \Delta v_\delta = 480 \text{ ms}^{-1}, \\
 v_{\delta,3} &= v_{\delta,2} - \Delta v_\delta = 429 \text{ ms}^{-1}.
 \end{aligned} \tag{20}$$

The goal of this experiment is to slow the atoms sequentially within the capture range of each section, resulting in a single slowed atom peak while simultaneously minimizing the transverse diffusion. However, the figure shows two pronounced slowed atom peaks around $v_{\delta,3}=429 \text{ ms}^{-1}$ and $v_{\delta,2}=480 \text{ ms}^{-1}$, corresponding to the resonance velocities of the last two cavities. Clearly, the capture range of the last cylindrical cavity is smaller than the difference between the resonance velocities. Therefore, the atoms within the capture range of the middle cylindrical cavity cannot reach the capture range of the last cavity ($\Delta v_{cap} < \Delta v_\delta$).

Another peak is to be expected near $v_{\delta,1}=531 \text{ ms}^{-1}$ if the above statements are correct. The peak indeed exists, but disappears in the high velocity tail of the distribution. This is even more true because Δv_{cap} scales with $1/v_\delta$.

Finally, in order to optimize the total slowing effect of the three cavities we need

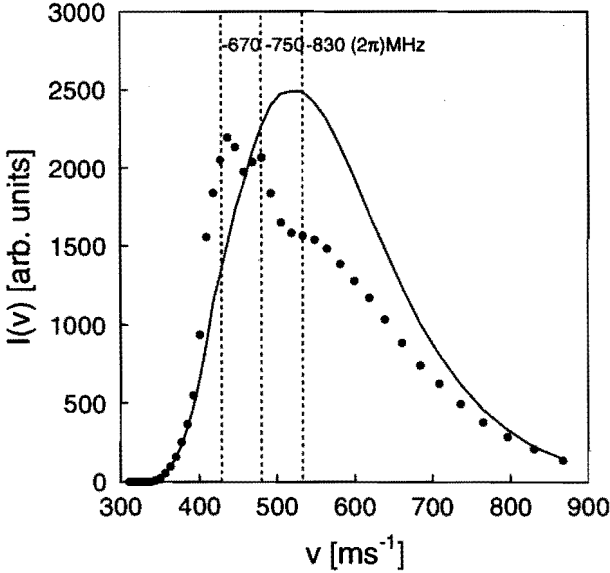


Figure 16: Experimental velocity distribution based on a multiple frequency slowing technique. Three cylindrical cavities are used each with an input power of $P=10$ mW and detunings of $\delta = -830, -750$ and -670 (2π)MHz in downstream order of the atomic beam, respectively. Again, the initial distribution is represented by a solid line.

to ensure that the capture range for a single cavity Δv_{cap} , is equal or larger than the step Δv_δ in the resonance velocities v_δ .

8.2 Acceleration

Instead of only choosing the laser detuning negative (red), we also switched to positive detuned laser light (blue). In this way, the resonance angle θ becomes larger than $\theta > \pi/2$. Therefore, atoms will only absorb photons which increase their axial velocity. To demonstrate this effect, Figure 17 shows the result for a three-cylindrical cavity setup with a detuning of $\delta=+780$ (2π)MHz and an input power of 3×10 mW. In this situation, all the atoms with a velocity larger than $v_\delta=500$ ms $^{-1}$ will be resonant with the laser light. This is comparable with the red detuned case. However, we cannot define a capture range because there is no unique final velocity. Analogous to the definition of the deceleration, the acceleration can be defined as, $\Delta v = v_i - v_f$. For example, this results in a similar curve as in Fig. 13, except for the fact that now the curve is the mirror image, *i.e.*, the initial and final velocities, v_i and v_f , are interchanged. In this case, the experiment can be considered as the time inversion of the red detuned experiment.

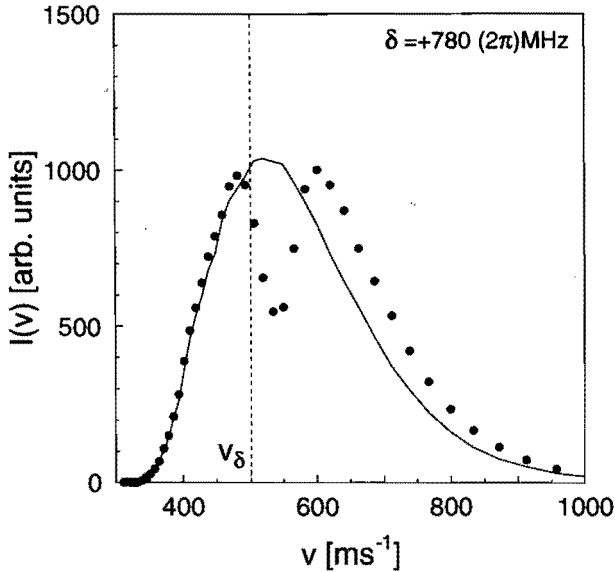


Figure 17: Velocity distribution for a blue detuned laser resulting in acceleration instead of deceleration. For velocities higher than the resonance velocity $v_{\delta}=500 \text{ ms}^{-1}$ the atoms stay in resonance, which results in a minimum in the distribution. Again the solid line represents the initial velocity distribution.

The acceleration is velocity dependent and results in a slightly compressed velocity distribution. However, in this case the initial distribution is split up in comparison with the red detuned experiments. This results in a minimum in the distribution at a position near the resonance velocity v_{δ} with a compressed part for velocities larger than the resonance velocity as can be seen from the slight increase in intensity in Fig. 17. This figure also shows a pronounced shift in the velocity distribution resulting in a minimum near the resonance velocity.

9 Concluding remarks

We have studied the slowing effect of metastable neon atoms experimentally in a monochromatic isotropic light field. The setup used is a beam apparatus based on the time-of-flight technique together with a position-dependent metastable atom detector. In this manner, we can determine both the axial velocity change Δv_{\parallel} , and the perpendicular velocity change Δv_{\perp} of the atoms. The isotropic light field is created by using the material Spectralon [12], which is an ideal isotropic reflector and has a large reflectance value $\mathcal{R} \approx 0.99$. Therefore, the laser input power can be relatively

small and the cavity length short, due to the large enhancement factor of the cavity which is proportional to $\mathcal{R}/(1 - \mathcal{R})$. The reflectance \mathcal{R} is very sensitive to contamination [12], and depends critically on the geometrical curvature of the optical cavity. However, we have not been able to verify the value of \mathcal{R} experimentally. For different laser input powers and frequency detunings striking deceleration effects are observed. Apart from deceleration, a significant divergence of the atomic beam is introduced. The absorption-emission cycles lead to an increase of the transverse velocity spread v_{\perp} . Especially the absorption-stimulated emission cycles contribute to this velocity spread when the resonance condition results in large angles θ and high laser powers are used.

Using model calculations, more insight has been gained into this isotropic slowing process. However, the calculations seem to overestimate the deceleration and, as a consequence, the transverse diffusion of the atomic beam. The straightforward test to check the calculations is by using a detuning $\delta = 0$ MHz and comparing the results with the experiment. In this case, the deceleration is switched off and we only obtain diffusion effects. The discrepancy between model and experiment cannot be explained by varying the laser power P and reflectance \mathcal{R} within realistic ranges. Note that we have incorporated the linewidth of the transition as well as the line broadening resulting from the light intensity. Therefore, we should investigate features which have not been taken into account in our theoretical model. For example, the Zeeman splitting of the magnetic sublevels due to earth magnetic field is expected to have a negligible effect because the energy splittings are small compared to the atomic linewidth. Additionally, the polarization preserving properties of the material Spectralon are not available. However, our model assumes an unpolarized laser field in view of the isotropic character of the scattering process.

Nevertheless, we can still deduce important information from the performance of the isotropic light slower. First, we have demonstrated that using isotropic light is an effective way to slow an atomic beam. This technique is most effective if the laser power is divided over multiple cavities. Secondly, the difference between a cylindrical and spherical geometry has been investigated. The experiments confirm the predictions presented in chapter II resulting in the same deceleration for comparable light intensity distributions in both geometries. However, for velocities above the capture range a larger beam divergence is obtained in the case of the cylinder, because more absorption-stimulated emission cycles occur. This makes a spherical optical cavity more ideal for slowing. In conclusion, we have demonstrated that isotropic light slowing is a promising technique to manipulate atomic beams.

References

- [1] A. Aspect, R. Kaiser, N. Vansteenkiste, and C. Westbrook, (1994), submitted to

Phys. Scripta.

- [2] W. Phillips, J. Prodan, and H. Metcalf, *J. Opt. Soc. Am. B.* **2**, 1751 (1985).
- [3] T. Barrett, S. Dapore-Schwartz, M. D. Ray, and G. Lafyatis, *Phys. Rev. Lett.* **67**, 3483 (1991).
- [4] V. Balykin, V. Letokhov, and V. Mishin, *Sov. Phys. JETP* **51**, 692 (1980).
- [5] W. Ertmer, R. Blatt, J. Hall, and M. Zhu, *Phys. Rev. Lett.* **54**, 996 (1985).
- [6] M. Zhu, C. Oates, and J. Hall, *Phys. Rev. Lett.* **67**, 46 (1991).
- [7] I. Littler, H.-M. Keller, U. Gaubatz, and K. Bergmann, *Z. Phys. D* **18**, 307 (1991).
- [8] W. Ketterle, A. Martin, M. Joffe, and E. Pritchard, *Phys. Rev. Lett.* **69**, 2483 (1992).
- [9] H. Batelaan, S. Padua, D. Yang, C. Xie, R. Gupta, and H. Metcalf, *Phys. Rev. A* **49**, 2780 (1994).
- [10] T.G. Aardema, R.M.S. Knops, S.P.L. Nijsten, J.P.J. Driessen and H.C.W. Beijerinck, this thesis: chapter II.
- [11] M. Hoogerland, Ph.D. thesis, Eindhoven University of Technology, The Netherlands, (1993).
- [12] Labsphere Inc., P.O.Box 70, North Sutton, NH 03260, USA.
- [13] M. Born and E. Wolf, *Principles of Optics* (Pergamon Press, Oxford, 1975).
- [14] H. van Benthem, private communication.
- [15] 4-dicyanomethylene-2-methyl-6(p-dimethyl-amino-styryl)-4H-pyran.
- [16] Photec, OFD 25/3/RA.

Chapter V

Excitation transfer for $\text{Xe}^*(^3\text{P}_2) + \text{N}_2$ in the eV energy range: double potential crossing for $\text{N}_2(\text{B}, v'=5)$

T.G Aardema, E.J. van Nijnatten and H.C.W. Beijerinck

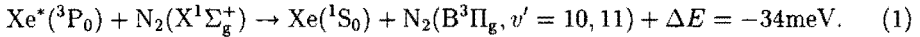
*Physics Department, Eindhoven University of Technology,
P.O. Box 513, 5600 MB Eindhoven, The Netherlands*

Abstract

In a crossed beam experiment the yield of $\text{N}_2(\text{B } ^3\Pi_g, v'=5)$ excited product molecules was measured for Xe^*/N_2 collisions over a kinetic energy range 80 - 2000 meV. The observed threshold is 59.4 meV, nearly equal to the endothermicity of 59 meV for this process. The dynamics of this collision process is described with a Landau-Zener model in terms of two curve crossings of the entrance and exit potentials. For energies higher than 500 meV additional curve crossing with the repulsive branch of the potentials of the $v' \leq 4$ final states can be reached, resulting in a sharp decrease of the $v' = 5$ production cross section.

1 Introduction

The excitation transfer process between metastable Xe* atoms and N₂ molecules is a fine example of distinct vibrational selectivity in the product N₂(B ³Π_g, *v*'). The reactions



and

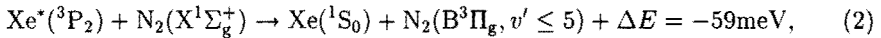


exhibit a preference for the *v*'=5 and 11 states, respectively, with an endothermic exit channel. These results were first observed in spectroscopic studies of the N₂(B³Π_g → A³Σ_u⁺) emission, in flowing and pulsed afterglows, as well as in beam-gascell and crossed beam experiments [1, 2, 3]. Optical pumping by a laser resulted in absolute cross sections being measured [4]. The first theoretical explanations were given by Krümpelmann et al. [5, 6] for the clear occurrence of the bands originating from *v*'=5, as well as *v*'= 10 and 11, in the N₂(B-A) product emission. In a more detailed approach the exothermic output channels *v*' ≤ 4 for Xe*(³P₂) were theoretically explained by Aquilanti et al. [7] in terms of model potentials.

This work describes a crossed beam experiment of reaction (2). Compared with Krümpelmann [5] we achieved a higher collision energy resolution and a considerably wider collision energy range. The results are discussed by using a semiclassical Landau-Zener model. The potential parameters determined by this model are compared with the calculated potential parameters of Aquilanti et al. [7].

2 Experimental

Recently the apparatus was described by Vredendregt et al. [8], which can be summarized as follows. A beam of metastable Xe* atoms crosses a supersonic secondary beam of N₂ molecules. The metastable Xe* atoms are produced in two types of sources. First, the thermal metastable atom source (TMS) [9], a discharge-excited supersonic expansion supplies atoms with translational energies in the range 80 < *E*[meV] < 110 when operated with pure Xe. By seeding this gas in He, higher energies 100 < *E*[meV] < 200 for a mixture of 15% Xe in 85% He can be attained. Secondly, a hollow cathode arc beam source (HCA) [10] covers the superthermal energy range, 180 < *E*[meV] < 2000. The secondary beam is a skimmed, supersonic expansion from a nozzle 80 μm in diameter and at room temperature.

In the scattering centre, fluorescence photons are produced and detected in a direction perpendicular to both beams by a high efficiency optical system. This system consists of an EMI 9658 photomultiplier, a lens section and a bandpass interference

filter for final state selection. The scattering volume of 150 mm³ is fully accepted by the optical system, with an average solid angle efficiency of 41 %. The overall efficiency at $\lambda = 668.87$ nm is 5.86×10^{-4} counts/photon. The product of target number density n and interaction length l of primary and secondary beams has a calculated average value $\langle nl \rangle = 9.6 \times 10^{16} \text{ m}^{-2}$ for 1500 Torr N₂ stagnation pressure and 300 K nozzle temperature [11].

The primary beam is chopped by a mechanical chopper in order to resolve the collision energy dependence of the fluorescence signal with a single-burst time of flight (TOF) method. The velocity distribution in the primary beam is measured with a metastable atom detector consisting of a stainless steel plate and an electron multiplier. By using the relative data of Borst [12] and the "absolute" value for Ar* of Theuws [13], we estimated the metastable detection efficiencies of Xe*(³P₀) and Xe*(³P₂), which are $\eta_m = 0.039$ and 0.014, respectively. The results of Böhle et al. [4] showed that the ratio r of Xe*(³P₂) to Xe*(³P₀) atoms is not statistical [4]. The analysis of our data is based on the assumption that $r = 12 \pm 1$, independent of the collision energy [14]. This value has been determined by comparing our absolute values for the cross section of the reaction in Eq.(1), which is fully due to Xe*(³P₀), with the values given by Böhle et al. [4]. Recent experiments on the ¹³¹Xe* isotope result in $r = 11.5 \pm 2$ and thus confirm this estimate [15].

Both the photomultiplier and the metastable atom detector are operated in pulse counting mode. The pulses are fed into a multichannel counting device which is interfaced to a M68000 Phydas computer and interface system [16] that controls most of the experiment. The raw data is stored on a central file server of the department for further analysis on a separate microcomputer.

3 Experimental cross sections

To determine the cross section for excitation of ground state N₂(X¹Σ_g⁺, $v = 0$) to vibrational level $v' = 5$ of N₂(B³Π_g) in collision with Xe* atoms, we monitored the intensity of the decay N₂(B³Π_g, v') → N₂(A³Σ_g⁺, v''), referred to as the first positive system [17]. Since this system is state selective, a custom-made bandpass interference filter has been used, with a central wavelength of $\lambda_c = 670.34$ nm and a bandpass of $\Delta\lambda = 12.9$ nm, to monitor the $v' = 5$ to $v'' = 2$ decay emission. The wavelength of this emission line is $\lambda = 668.87$ nm. The measured intensity of the emission of $v' = 4 \rightarrow v'' = 1$, which is much smaller due to both the smaller effective cross section and detection efficiency of the optical system, lies well within the statistical error of the $v' = 5$ to $v'' = 2$ emission intensity. Therefore no corrections on the fluorescence yield are made for this extra exit channel.

The measurements consists of 22 to 50 cycles in which 5000 to 20000 TOF bursts of the fluorescence were accumulated. The total measuring time depends on the strength

of the signal. For this process the typical count rates for the different sources (HCA, TMS-SEED, TMS) in the top of the TOF spectra are 200, 1000 and 900 cps, respectively. To compensate for drift, the measurements of the photon TOF spectrum were sandwiched between two measurements of the TOF spectrum of the metastable atoms. The TOF spectra of the metastable atoms were taken with the secondary beam off. A full measurement might take up to 12 hours to complete. The measurements with the HCA source were repeated one more time to obtain sufficient statistical accuracy. These data sets were first analyzed separately, and afterwards averaged according to their statistical weight.

The analysis performed to convert fluorescence and metastable atom TOF spectra into inelastic cross sections has been described in detail by Van Vliembergen et al. [18]. Here we only give a brief description. First, the TOF spectrum of the metastable Xe^* atoms at the detector is converted to a velocity distribution by least-squares adjustment of a suitable model function. The convolution of this model function with the finite velocity resolution due to the width of the chopper slit is included in this least-squares process. This velocity distribution is converted to a TOF distribution $N_m(t_i)$ for metastable atoms at the position of the scattering center. From this and the measured TOF spectrum $N_{ph}(t_i)$ of the fluorescence, the inelastic cross section $Q^{v'}$ is determined by,

$$Q^{v'}_{\text{expt}}(E(t_i)) = \frac{N_{ph}(t_i)}{N_m(t_i)} \frac{r+1}{r} \frac{\eta_m}{\eta_{ph}} \frac{1}{M_{v',v''}} \frac{\Omega_m}{\Omega_{sc}} \frac{Q_{el}}{\left[1 - \exp(-\langle nl \rangle \frac{g}{v_1} Q_{el})\right]}. \quad (3)$$

Here, $E(t_i)$ is the collision energy, calculated from the velocity of the Xe^* atoms v_i arriving at time t_i at the scattering center and the velocity v_2 of the target molecules. The fraction $r/(r+1)$ takes into account that only $\text{Xe}^*(^3\text{P}_2)$ atoms contribute to this cross section, with r the ratio of the population of $\text{Xe}^*(^3\text{P}_2)$ to $\text{Xe}^*(^3\text{P}_0)$. The quantity g is the relative velocity and $\langle nl \rangle$ is the mean value of the density-length product. Both v_2 and $\langle nl \rangle$ can be calculated accurately from the source parameters and the skimmer geometry [11]. The solid angle in which the Xe^* atoms reach the metastable atom detector and the scattering center are denoted as Ω_m and Ω_{sc} , respectively. The coefficient $M_{v',v''}$ is the optical branching ratio for the decay $\text{N}_2(\text{B}, v') \rightarrow \text{N}_2(\text{A}, v'')$, calculated from the Einstein coefficients tabulated by Lofthus and Krupenie [17]. The integral elastic cross section $Q_{el} = 200 \text{ \AA}^2$ excluding small angle scattering, is taken notably smaller than the full total elastic cross section $Q_{el} \approx 500 \text{ \AA}^2$ [19, 20]. The inelastic cross section $Q^{v'}$ is, however, in first order insensitive to the exact value of Q_{el} . Finally, η_m and η_{ph} are the detection efficiencies for the metastable atoms and photons, respectively.

The photon detection efficiency $\eta_{ph} = \eta_t \eta_{qe} \eta_{\Omega}$ is determined by the transmission of the lens system $\eta_t = 0.41$, the quantum efficiency of the photomultiplier $\eta_{qe} = 0.08$ and the solid angle acceptance η_{Ω} . The scattering centre is spatially fully accepted by the

detection system in which the solid angle acceptance is constant, $\eta_{\Omega} = \eta_{\Omega}^0 = 3.27 \cdot 10^{-2}$. However, η_{Ω} is not constant for the entire zone of radiative decay of the longlived $N_2(B, v' = 5)$ products. For the distance z , from the center of the scattering center along the primary beam axis, the experimental relations are

$$\begin{aligned} 0 < z[\text{mm}] < 3 & \quad \eta_{\Omega}(z) = \eta_{\Omega}^0 = 3.27 \cdot 10^{-2}, \\ 3 < z[\text{mm}] < 9.75 & \quad \eta_{\Omega}(z) = \eta_{\Omega}^0(1.44 - z \cdot 0.148 [\text{mm}^{-1}]), \\ 9.75 < z[\text{mm}] & \quad \eta_{\Omega}(z) = 0. \end{aligned} \quad (4)$$

This relation is exactly the same for the x -direction of the secondary beam axis and only slightly different for the y -direction of the optical detection system.

Owing to the long radiative lifetime of $N_2(B, v')$ ($\tau \approx 5 \mu\text{s}$ [21]), a significant number of product molecules of reaction (2) leave the line of view of the optical system before radiative decay occurs. The inelastic cross section $Q^{v'=5}$ was corrected for this effect by scaling the experimental cross section with a calculated effective solid angle acceptance $\eta_{\Omega_{eff}}$, as given by

$$\begin{aligned} Q^{v'}(E(t_i)) &= \frac{\eta_{\Omega}^0}{\eta_{\Omega_{eff}}^0} Q^{v'}_{expt}(E(t_i)), \\ &= c(\tau_{v'}, E) Q^{v'}_{expt}(E(t_i)), \end{aligned} \quad (5)$$

with $c(\tau_{v'}, E)$ the energy dependent correction factor for the intensity. The effective solid angle acceptance is given by

$$\begin{aligned} \eta_{\Omega_{eff}}(E) &= \frac{1}{\tau_{v'}} \int_0^{\infty} \eta_{\Omega}(z) \exp\left(\frac{-t(E)}{\tau_{v'}}\right) dt, \\ t(E) &= \frac{z}{v'_{N_2}(E)}. \end{aligned} \quad (6)$$

For a realistic estimate for the average value of the velocity $v'_{N_2}(E)$ of the scattered $N_2(B^3\Pi_g, v')$ molecules along the primary beam axis in the laboratory velocity we assume that backward scattering dominates in the collision frame. A Newton diagram of the collision at $E = 100$ meV and 1000 meV is given in Fig. 1, together with the v'_{N_2} value used for calculating the correction factor in Eq.(6). For the lifetime of the $N_2(B^3\Pi_g, v'=5)$ level we have used $\tau_{v'} = 5.8 \mu\text{s}$ [21]. In Fig. 2 the resulting intensity correction factor $c(\tau_{v'}, E)$ is plotted, showing a pronounced influence of the correction factor on the measurements in the experimentally accessible energy range.

Especially in the thermal energy range the specific shape of the inelastic differential cross section has a large influence on the laboratory velocity v'_{N_2} , even for backward scattering. Because the correction factor c is small, this will most likely only influence the threshold energy.

In the superthermal energy range $E > 1000$ meV the laboratory velocity v'_{N_2} is rather independent of the scattering angle when backward scattering dominates.

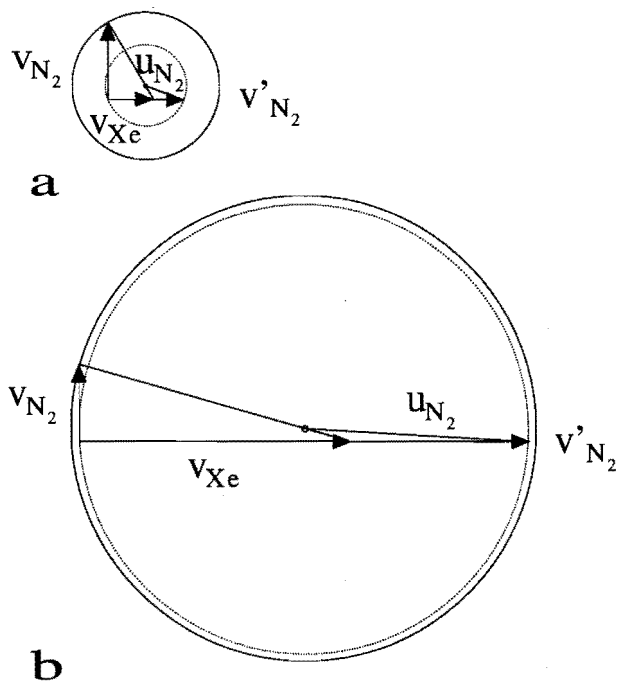


Figure 1: Newton diagram of the collision process at an energy $E = 100$ meV (a) and $E = 1000$ meV (b), typical for the thermal and the superthermal energy range, respectively. Both the elastic (solid line) and the inelastic scattering sphere (dashed line) are indicated. The N_2 secondary beam velocity is $v_{N_2} = 790$ m/s. The velocity v'_{N_2} of the $N_2(B^3\Pi_g, v'=5)$ molecules scattered in the direction of the primary beam, as used for the calculation of the lifetime correction factor, is also indicated.

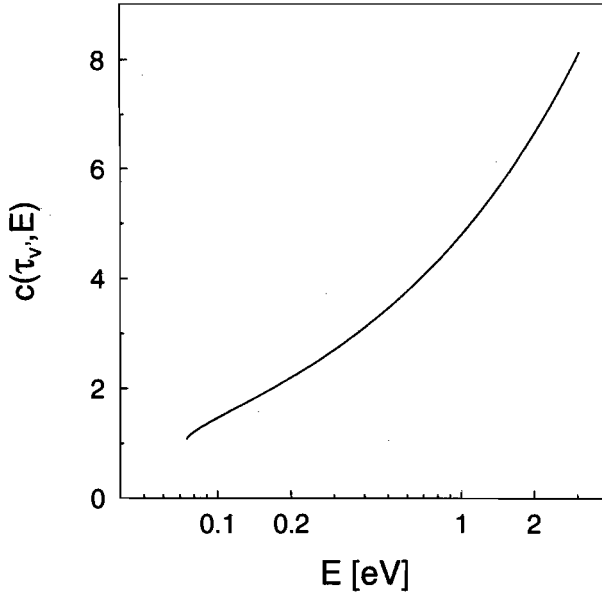


Figure 2: The intensity correction factor $c(\tau_{v'}, E)$ for calculation of the cross section.

Because the correction factor scales with v'_{N_2} , we expect only a small influence of the specific shape of the differential cross section.

However, differential cross section measurements will finally have to decide if these assumptions are justified. The experimental effort to obtain these data is huge and it is not to be expected that these will be available in short term.

Figure 3 shows the cross section $Q^{v'=5}$ obtained from the experimental signals after correction according to equation (3) and (6). The energy range covered by the three different metastable atom sources is indicated by a horizontal bar. Rather satisfying is the smooth connection of the data points of the three different beam sources without using any scaling. The data obtained with the seeded TMS source in the energy range $150 < E[\text{meV}] < 200$ are not used due to the presence of He^* metastables in the primary beam in this energy range. From a threshold of $E = 59.4 \text{ meV}$ we observe a step rise, a flat top with two maxima at $E \simeq 200 \text{ meV}$ and $E \simeq 500 \text{ meV}$, respectively, and a decrease beyond the second maximum. At $E \simeq 1000 \text{ meV}$ we observe an additional cut-off, i.e. a discontinuity in the first derivative.

4 Multiple curve crossings

For reaction (2) model potential calculations [7] show that only for an approach of the collision partners parallel to the N_2 axis the exit channel $v'=5$ can be reached.

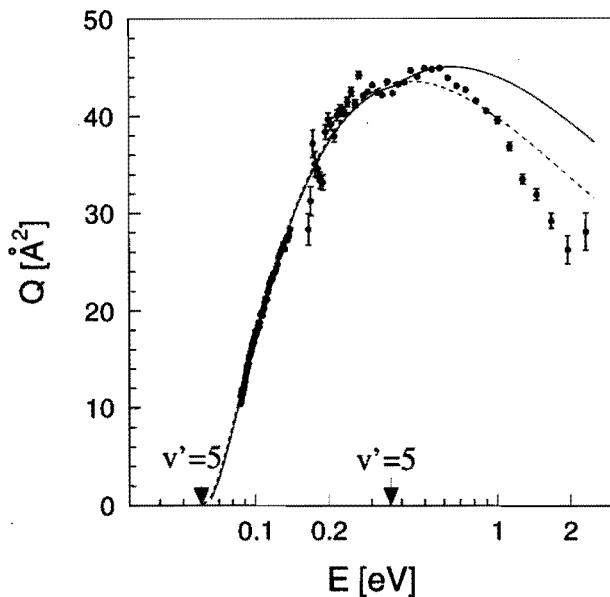


Figure 3: Absolute cross section $Q^{v'=5}$ for the vibrational excitation of $N_2(B \ ^3\Pi_g, v'=5)$ in a collision of $Xe^*(^3P_2)$ with $N_2(X)$ as a function of the collision energy E . The energy range covered by the three different metastable atom sources - thermal (TMS), seeded thermal (SEED) and superthermal (HCA) - is indicated by a horizontal bar.

Due to the spatially quite diffuse (6s) orbital of the $Xe(^3P, 5p^56s)$ atom, the entrance channel is already repulsive for internuclear distances where the potential of the exit channel is still rather flat. As a result, the entrance potential crosses the endothermal $v' = 5$ exit channel twice before reaching the additional, exothermal exit channels with $v' \leq 4$. In Fig. 4 the relevant potentials of reaction (2) are depicted for the parallel approach, i.e. with the N_2 axis parallel to the relative velocity vector. The anisotropy due to the $(5p^5)$ core of the $Xe(^3P)$ atom is not taken into account. If the crossings are considered as a sequence of independent, nonadiabatic events, they can be treated within the Landau-Zener theory.

For a diabatic crossing the probability $p(b)$ is given by [22]

$$p(b) = \exp(-v_x/v_{rad}(b)), \quad (7)$$

with v_{rad} the radial velocity at the crossing point R_x and v_x the reference velocity determined by the difference in slopes ΔF_x of the intersecting diabatic potential curves and the diabatic coupling matrix element H_x , equal to

$$v_x = \frac{2\pi|H_x|^2}{\hbar|\Delta F_x|}. \quad (8)$$

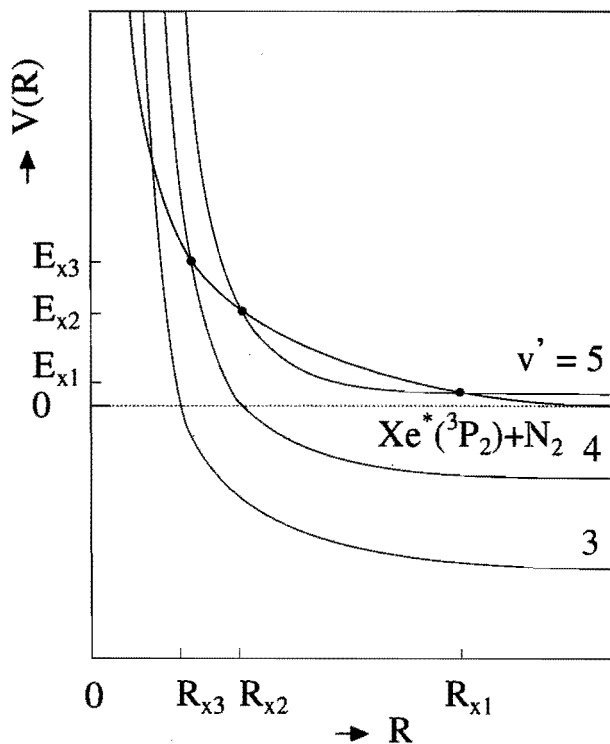


Figure 4: Schematic potential curves for the system $\text{Xe}^*(^3\text{P}_2)+\text{N}_2$. This situation corresponds to a parallel orientation of the intramolecular N_2 axis with respect to the relative velocity. Each curve crossing is characterized by the parameters $E_{x,i}$, $R_{x,i}$ (indicated in the figure) and the characteristic velocity $v_{x,i}$. The entrance potential represents the V_{22} potential of Aquilanti [7].

For a single curve crossing, the total excitation probability P_s at a fixed impact parameter b is

$$P_s(b) = 2p(1-p). \quad (9)$$

For a double curve crossing the result is,

$$P_d(b) = \mathcal{F} \left[p_1(1-p_1) \left[(1-p_2)^2 + p_2^2 \right] + p_2(1-p_2) \left[(1-p_1)^2 + p_1^2 \right] \right]. \quad (10)$$

In this equation the subscripts 1 and 2 refer to the crossings for decreasing internuclear distance respectively. In this case of a twofold crossing we have $\mathcal{F} = \mathcal{F}_d = 2$; for $p_2 = 0$ equation (9) and (10) are the same. However, for the case of a triple crossing, according to the situation depicted in Fig. 4 the factor \mathcal{F} is equal to

$$\mathcal{F}_t = 1 + (1-p_3)^2 + p_3^2. \quad (11)$$

For each model, the cross section for excitation of $N_2(B)$ is calculated by integration of Eqs. (9) and (10) over the impact parameter b ,

$$Q(E) = \frac{1}{3} \int_0^{b_{max}} P(b) 2\pi b \, db, \quad (12)$$

where b is limited to a value b_{max} for which the curve crossing can be reached. This parameter depends not only on the crossing point R_x , but also on the threshold energy E_x of the crossing point with respect to the initial asymptotic energy. The factor $\frac{1}{3}$ takes into account that only for a parallel approach of the colliding partners excitation of $N_2(B, v'=5)$ can occur [7].

5 Analysis of cross section

The theoretical curve crossing parameters in Table 1 are determined from the V_{22} potential of the alternative model of Aquilanti [7]. Where he uses a more isotropic potential and a strongly anisotropic switching function. This choice is made on the basis of electronic symmetry : the major contributions to the excitation process are shown to come from homogeneous $\Pi - \Pi$ crossings.

Using the models for multiple curve-crossings (section 4) we have analysed the experimental cross sections with a least squares method, with the crossing parameters E_x , R_x and v_x as free parameters. First we have used a model with only a single curve crossing (1). The parameters are given in Table 1 ; the resulting curve is shown in Fig. 5, together with the experimental data. The low energy part of the cross section is described rather well, and we do expect that the value of the threshold energy and the characteristic velocity are realistic.

Comparison of the experimental value of the threshold energy $E_{x,1} = 59.4$ meV with the calculated endothermicity $|\Delta E| = 59$ meV (Eq. 2) shows that the exit potential

Table 1: Parameters for the three curve crossings, as determined from a least squares curve fit with the model functions described in section 4. The deviations are given between parentheses. For crossings (2) and (3) the value of the crossing radius is fixed by the condition $R_{x,2}/R_{x,1} = 0.81$ and $R_{x,3}/R_{x,1} = 0.77$ as given by Aquilanti [7]; only the threshold energy and the reference velocity have been treated as a free parameter. For crossing (2) a full least squares analysis has been performed; for crossing (3) the parameters are only optimized by visual comparison with the data.

Crossing number	Energy (meV)	this work			model
		single	double	triple	potential [7] ^a
#1	$E_{x,1}$ [meV]	86 - 334	86 - 580	86 - 1004	46
	$R_{x,1}$ [Å]	59.4 (0.7)	59.6 (0.6)	59.6 ^b	4.34
	$v_{x,1}$ [m/s]	6.12 (0.02)	6.12 (0.02)	6.12 ^b	-
#2	$E_{x,2}$ [meV]	491 (16)	485 (13)	485 ^b	-
	$R_{x,2}$ [Å]		396 (38)	396 ^b	255.8
	$v_{x,2}$ [m/s]		4.96 ^b	4.97 ^b	3.51
#3	$E_{x,3}$ [meV]		148 (78)	150 ^b	-
	$R_{x,3}$ [Å]			510 (30) ^c	336.1
	$v_{x,3}$ [m/s]			4.71 ^b	3.35
				1000 (200) ^c	-

^a Determined from the V_{22} potential of the alternative model of Aquilanti [7].

Where he uses a more isotropic potential and a strongly anisotropic switching function.

^b These parameters have been fixed to these values and thus do not have an error bar.

^c Estimated error bar.

is still very flat at the crossing radius, which is in general agreement with the large experimental value $R_{x,1} = 6.12$ Å. The threshold energy $E_{x,1} = 46$ meV predicted by the exit potential of Aquilanti et al. [7] is lower than the endothermicity, indicating that their potential is slightly attractive at this distance. This difference is in general agreement with their smaller value $R_{x,1} = 4.34$ Å for the crossing radius.

In the region near the maximum and beyond the agreement is rather poor : it is clear that a single curve crossing cannot describe our experimental results. The next step is using a model function with two curve crossings labelled (1) and (2) with increasing value of the threshold energy, i.e. with decreasing value of the crossing radius R_x (Fig. 4). At low energies the results, plotted in Fig. 5, are indistinguishable from the previous analysis. However, the flat top structure near the maximum (with the suggestion of a double peaked nature) is described rather accurately. The cross section in this energy range remains at a constant value due to the contribution of the second crossing with a higher value of the threshold energy : an extra possibility for reaching the exit channel is opened. The crossing parameters are listed in Table 1. For

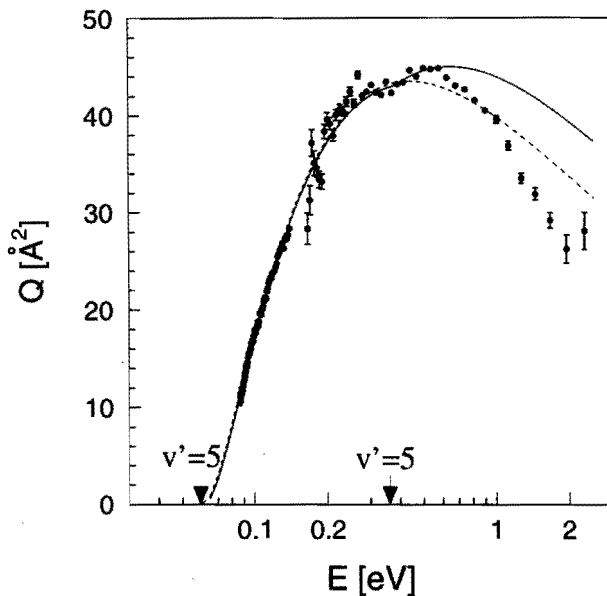


Figure 5: Experimental data of the cross section for the vibrational excitation of $\text{N}_2(\text{B}^3\Pi_g, v'=5)$, together with the model cross sections for the single (dotted line) and double (full line) curve crossing described in section 4 with the parameters given in Table 1. Arrows indicate the threshold energy for the first and second crossing of the $v' = 5$ state.

crossing (1) the values are in good agreement with the single crossing values, as can be expected. Due to the small collision energy range where crossing (2) contributes to the cross section, we observe a large correlation of the characteristic velocity $v_{x,2}$ with the crossing radius $R_{x,2}$. Only the value of the threshold $E_{x,2}$ is determined rather accurately. For this reason we have fixed the value of the second crossing by demanding that $R_{x,2}/R_{x,1} = 0.81$ as follows from the potential curves of Aquilanti et al. [7]. The resulting experimental value $v_{x,2} = 150$ m/s for the characteristic velocity, which is a factor three smaller than $v_{x,1}$, reflects the larger value of $|\Delta F_x|$ expected for a crossing with the steeper repulsive branch of the exit potential.

For a collision energy $E \geq 500$ meV we still observe a large discrepancy which is not incorporated in our model with two curve crossings. The most likely explanation of these discrepancies is the loss of flux due to the excitation of the vibrational levels $v' = 4$ and $v' = 3$. The rather soft repulsive branch of the entrance potential will cross the the steep repulsive branch of the lower lying vibrational states (Fig. 4), with increasing threshold values for decreasing vibrational state numbers v' . We have investigated this possibility by adding a third curve crossing (3). For this third crossing we have fixed the crossing radius by demanding $R_{x,3}/R_{x,1} = 0.77$ as follows from the potential of

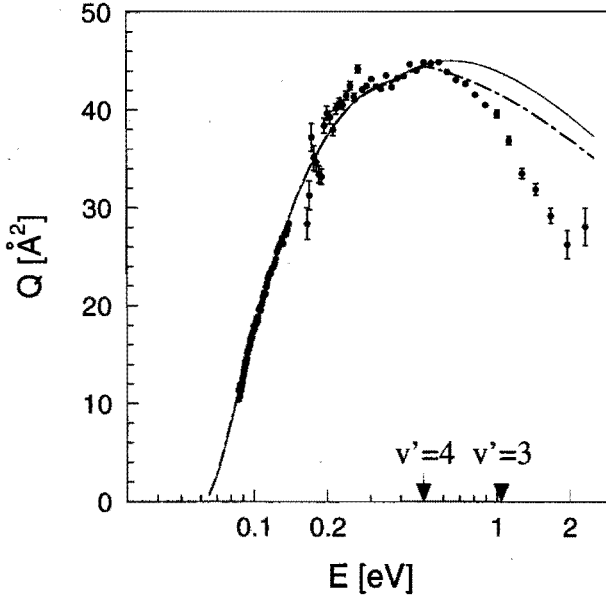


Figure 6: Experimental data of the cross section for the vibrational distribution of $N_2(B^3\Pi_g, v'=5)$, together with the results of the model cross sections for the double (full line) and the triple (dashed line) curve crossing described in section 4. Arrows indicate the threshold energy for the $v' = 4$ and $v' = 3$ vibrational levels.

Aquilanti et al. [7]. Both the threshold energy $E_{x,3}$ and the characteristic velocity $v_{x,3}$ have not been treated as a free parameter in a full least squares analysis, but have only been chosen by hand to obtain a reasonable agreement between model function and data points. The error bars are estimated values, where the agreement starts to deviate in a clearly visible fashion. The results are given in Table 1 and Fig. 6. We observe a realistic value $E_{x,3} > E_{x,2}$. The resulting curve gives an acceptable description for $500 \leq E [\text{meV}] \leq 1000$; for $E \geq 1000$ meV we again observe a sharp cut-off in the cross section, which we attribute to excitation to the even lower lying $v' = 3$ state.

As observed in Table 1, the experimental value of the crossing radius $R_{x,1}$ is larger than calculated by Aquilanti et al. Looking at Eq.(3) we see that the detection efficiencies for both the Xe^* beam and the photons determine the absolute value of the cross section. For the photon counting system we are pretty confident of our value for the detection efficiency. For the metastable atoms our estimate of the detection efficiency is much less accurate. Moreover, it also depends on the cleanliness of the metal surface and its previous history. The value of $R_{x,1}^2$ directly scales with the absolute value of the measured cross section $Q_{v'}$ and thus with η_{det} . If we accept the theoretical values of the crossing radii as a more accurate calibration of the metastable atom detection

efficiency and thus of the absolute value of the cross section, we have to apply an extra correction factor equal to $(R_{x,1})^2_{theor}/(R_{x,1})^2_{expt} = 0.50$ to the experimental $Q^{v'}$ values.

The absolute data of Böhle et al. [4], resulting in an effective cross section $(Q^{v'=5})_{eff} = 6.5 \text{ \AA}^2$ with an estimated error of 50 %, have been obtained in a beam-gascell configuration at an average energy of $\langle E \rangle = 50 \text{ meV}$. In view of the experimental value of the threshold energy $E_{x,1} = 59.4 \text{ meV}$, the total yield in this experiment is due to collisions from atoms in the high-energy tail of the collision energy distribution. The real cross section is thus at least a factor two larger, of the order of $Q^{v'=5} \geq 13 \text{ \AA}^2$. We can only conclude that both experimental absolute values are in fair agreement within their error bars. This leads us to the conclusion that the experimentally obtained value for $R_{x,1}$ is correct.

The experimental values of the threshold energies $E_{x,i}$, that do not depend on the absolute value of the cross section, are all larger than the calculated results. The ratio's $(E_{x,i})_{expt}/(E_{x,i})_{theor} = 1.29, 1.55$ and 1.52 for $(i) = 1, 2,$ and $3,$ respectively, indicate a steeper repulsive branch of the entrance potential. This observation is in general agreement with a larger value of $R_{x,1}$ and a threshold energy $E_{x,1}$ equal to the endothermicity $|\Delta E|$ of the process.

Finally, one can wonder if the cut-offs observed can also be caused by an effect of the energy dependence of the shape of the inelastic differential cross section, through the intensity correction factor. In our opinion the discontinuous character of the cut-offs largely excludes this possibility.

6 Concluding remarks

The energy dependence of electronic excitation of the $N_2(B^3\Pi_g, v'=5)$ vibrational state for $Xe^*(^3P_2)+N_2$ collisions has been determined in a crossed beam experiment. The wide energy range covered, from 86 to 2000 meV, reveals the dynamics of this process in terms of Landau-Zener model functions. We have shown both the existence of a double curve crossing of entrance and exit channels and, for higher energies, the role of excitation to lowerlying vibrational states $v' \leq 4$ as a loss mechanism. Both from the large value of the crossing radius $R_{x,1}$ and from the large values of the the threshold energies $E_{x,i}$, as compared to the potentials of Aquilanti et al. [7], we can conclude that the entrance channel of this system is more repulsive for large internuclear distances.

References

- [1] D. Stedman and D. Setser, *J. Chem. Phys.* **52**, 3957 (1970).
- [2] T. Nguyen, N. Sadeghi, and J. Pebay-Peyroula, *Chem. Phys. Letters* **29**, 242 (1974).

-
- [3] J. B. Bruno and J. Krenos, *Chem. Phys. Letters* **74**, 430 (1980).
- [4] W. Böhle, H. Geisen, T. Krümpelmann, and C. Ottinger, *Chem. Phys.* **133**, 313 (1989).
- [5] T. Krümpelmann and C. Ottinger, *Chem. Phys.* **140**, 142 (1987).
- [6] T. Krümpelmann, C. Nyeland, and C. Ottinger, in *Book of Abstracts*, edited by J. Geddes, H. Gilbody, A. Kingston, C. Latimer, and H. Walters (North Holland, Amsterdam, 1988), p. 695.
- [7] V. Aquilanti, R. Candori, F. Pirani, T. Krümpelmann, and C. Ottinger, *Chem. Phys.* **142**, 47 (1990).
- [8] E. Vredenbregt, W. Boom, R. van Gerwen, and H. Beijerinck, *Chem. Phys.* **145**, 267 (1990).
- [9] M. Verheijen, H. Beijerinck, L. van Moll, J. Driessen, and N. Verster, *J. Phys. E* **17**, 904 (1984).
- [10] P. Theuws, H. Beijerinck, N. Verster, and D. Schram, *J. Phys. E* **15**, 573 (1982).
- [11] H. Beijerinck and N. Verster, *Physica C* **111**, 327 (1981).
- [12] W. Borst, *Rev. Sci. Instr.* **42**, 1543 (1971).
- [13] P. Theuws, Ph.D. thesis, Eindhoven University of Technology, The Netherlands, (1981).
- [14] E. van Nijnatten, Internal Report VDF/NO 92-15, Eindhoven University of Technology, The Netherlands (unpublished).
- [15] N. van Asten, private communication.
- [16] J. Emck, J. Voskamp, and A. van der Wal, *Op. Syst. Rev.* **23**, 33 (1989).
- [17] A. Lofthus and P. Krupenie, *J. Phys. Chem. Ref. Data.* **6**, 226 (1977).
- [18] E. van Vliembergen, E. Vredenbregt, G. Kaashoek, J. Jaspar, M. van Lanen, M. Janssens, M. Verheijen, and H. Beijerinck, *Chem. Phys.* **114**, 117 (1987).
- [19] R. van Gerwen, E. Vredenbregt, E. Kerstel, and H. Beijerinck, *Chem. Phys.* **118**, 407 (1987).
- [20] E. Kerstel, M. Janssens, K. van Leeuwen, and H. Beijerinck, *Chem. Phys.* **121**, 211 (1988).

- [21] E. Eyler and F. Pipkin, *J. Chem. Phys.* **79**, 3654 (1983).
- [22] E. Nikitin and S. Umanskii, *Theory of Slow Atomic Collisions* (Springer, Berlin, 1984).

Chapter VI

Excitation transfer of $\text{Kr}\{4p^5 5p; ^3D_3\}$ in collisions with N_2 molecules

T.G. Aardema, N.A.A.J. van Asten, J.P.J. Driessen
and H.C.W. Beijerinck

*Physics Department, Eindhoven University of Technology,
P.O. Box 513, 5600 MB Eindhoven, The Netherlands*

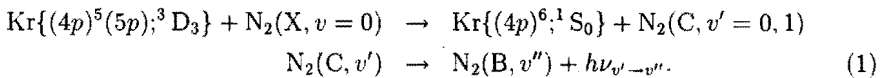
Abstract

Cross sections for the excitation of the $v' = 0$ and 1 vibrational levels of the electronically excited $\text{N}_2(\text{C}, v')$ product state have been measured, for collision energies in the range $85 \leq E(\text{meV}) \leq 115$, using the short-lived laser-excited $\text{Kr}\{(4p)^5 5p; ^3D_3\}$ atoms as projectile. The cross sections $Q_{v'} = 10.0 \text{ \AA}^2$ for $v' = 0$ and 7.2 \AA^2 for $v' = 1$ for this slightly exothermic process are interpreted in terms of a Landau Zener model, with the ionic $\text{Kr}^+ + \text{N}_2^-$ state as an intermediate which crosses both the initial and final state. The crossing parameters are in good agreement with the results obtained for the similar but strongly endothermic process for the $\text{Kr}\{(4p)^5 5s; ^3P_0, ^3P_2\} + \text{N}_2$ systems, investigated by Vredenbregt et al. [Chem. Phys. 145, 267 (1990)] in the superthermal energy range.

1 Introduction

Model potential calculations exist for the electronically excited rare gas ground-state plus rare gas systems, with $\text{Ne}\{(2p)^5 3p\} + \text{He}$ as an example of a system that has been investigated in full detail both theoretically [1, 2] and experimentally [3, 4, 5]. As yet, the complexity of excited atom-molecule systems is almost prohibitive for large scale calculations of the interaction potentials, couplings and scattering cross sections. The model potentials of Aquilanti et al. [6] for the $\text{Xe}^*\{(5p)^5 6s\} + \text{N}_2$ system are a first approach to understand the dynamics of the processes involved [7, 8, 9]. Considering the amount of experimental data, the metastable rare gas - N_2 and CO systems are developing into benchmark systems for future ab-initio theoretical treatments. The available data include electron energy distributions [10, 11, 12, 13] and state selected integral cross sections [14, 15, 16, 17] for Penning and associative ionization, differential and integral elastic scattering cross sections [18, 19, 20] for selected systems, and electronic, vibrational, rotational and fine-structure state distributions of final states involved in the excitation transfer process [7, 18, 21, 22, 23, 24, 25].

To investigate the role of both kinetic energy and electronic energy in the process of excitation transfer in collisions of electronically excited rare gas-molecule systems, we have studied the process



Throughout this paper we will use the shorthand notation Kr^{**} for the short-lived, laser excited $\text{Kr}\{(4p)^5 5p;^3D_3\}$ initial state, whereas the notation Kr^* will be used to refer to the metastable $\text{Kr}\{(4p)^5 5s;^3P_{0,2}\}$. The initial state lies 170 meV above the $\text{N}_2(C, v'=1)$ energy level, resulting in an exothermic reaction for the $v'=0$ and 1 final states. The endothermicity of the $\text{N}_2(C, v'=2)$ final state is 70 meV. The final product $\text{N}_2(C, v')$ states are detected by analysing the fluorescence due to the radiative decay to the $\text{N}_2(B)$ state (1).

In contrast, the metastable $\text{Kr}^*(^3P_2)$ and $\text{Kr}^*(^3P_0)$ states of the $\{(4p)^5 5s\}$ multiplet lie well below the $\text{N}_2(C, v'=0..3)$ energy levels, resulting in a strongly endothermic process with a threshold energy of 1.12 eV and 0.47 eV, respectively. Only in the superthermal range of collision energies do we observe this process, as shown by Tabayashi et al. [21], Van Gerwen et al. [18] and by Vredendregt et al. [24]. The latter data have been interpreted in terms of a coupling of initial and final state by the Coulomb potential of the intermediate $\text{Kr}^+ + \text{N}_2^-$ ionic state.

A schematic potential energy diagram for the $\text{Kr}^{*(*)} + \text{N}_2$ systems is given in Fig. 1, based on the correct asymptotic energies. For the intermediate ionic state $\text{Kr}^+ + \text{N}_2^-$ a pure Coulomb curve is used. Only the rather flat, long range part of the covalent potentials is shown, as relevant for the curve crossings involved. For collisions with the

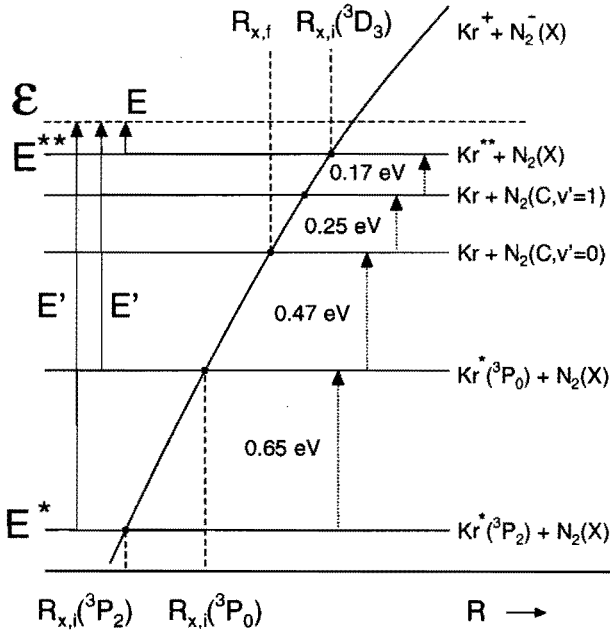


Figure 1: Schematic potential energy diagram of the $\text{Kr}^{(*)} + \text{N}_2$ system. Only the flat, long range part of the covalent state potentials is shown; for the intermediate $\text{Ar}^{+} + \text{N}_2^{-}$ ionic state a pure Coulomb potential is used.

same total energy \mathcal{E} , as indicated in Fig. 1, the available kinetic energy E for the initial $\text{Kr}^{**} + \text{N}_2$ and $\text{Kr}^{*} + \text{N}_2$ systems is quite different, with $E = (\mathcal{E} - E^{**}) \ll (\mathcal{E} - E^*) = E'$. Comparison of the Kr^{**} and the Kr^{*} systems in the thermal and superthermal range of kinetic energy, respectively, can therefore shed new light on the reaction dynamics and the coupling potentials involved.

In section 2 we discuss those aspects of the experimental setup, which are relevant for the interpretation of the absolute values of the cross sections. The process of laser excitation, however, which determines the fraction of krypton atoms in the short lived Kr^{**} initial state, is discussed in more detail. In section 3 the measured cross sections are presented, including their decomposition in terms of pure vibrational state excitation cross sections. In section 4 we discuss an interpretation in terms of a simple Landau Zener model, using semi-empirical coupling potentials as input. Also, the results are compared to the $\text{Kr}^{*} + \text{N}_2$ experiments. Finally, in section 5, we discuss the insight obtained.

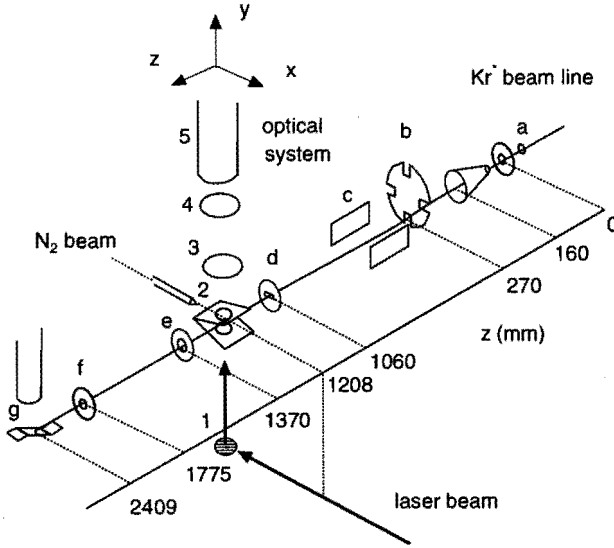


Figure 2: Schematic view of the crossed beam apparatus: a) thermal metastable atom source; b) mechanical TOF chopper; c) deflection plates; d) 3×7 mm collimator; e) 0.3 mm diameter collimator; f) 0.1 mm diameter collimator; g) metastable atom detector: metal plate + 14-stage Cu-Be electron multiplier. Optical system and laser beam: 1) 45° flat mirror for deflection of laser beam into y -direction; 2) wedge-shaped skimmer body with two quartz windows; 3) double lens system for focussing; 4) bandpass interference filter; 5) photomultiplier. The supersonic secondary beam consists of a $80 \mu\text{m}$ diameter nozzle and skimmer body with a 2.49 mm wide vertical skimmer slit.

2 Experimental setup

2.1 Crossed beam apparatus

Using a crossed beam apparatus we have investigated the process of Eq. (1). The experimental apparatus has been described by Van Vliembergen et al. [23], Van Gerwen et al. [18] and Vredendregt et al. [24] We only discuss the features that are important for the interpretation of the experiments in this paper. A schematic view of the apparatus is given in Fig. 2. A differentially pumped beam of metastable Kr^* atoms, originating from a discharge excited supersonic expansion at room temperature, is crossed at right angles with a supersonic secondary beam of N_2 molecules. A cryo-expansion chamber is used for pumping the secondary beam, resulting in close to ideal performance of the supersonic expansion and a well defined density-length product [26]. The solid angle acceptance of the scattering center for the Kr^* beam is $\Omega_{sc} = 18.7 \cdot 10^{-6}$ sr, as determined by a $3 \times 7 \text{ mm}^2$ aperture (Fig. 2).

In the scattering centre the Kr^* atoms are excited by a diode laser beam, aligned in the y -direction perpendicular to both the primary beam and the secondary beam. Collision induced fluorescence, produced in the scattering center, is collected at right angles to both molecular beams with an optical system with a large solid angle acceptance. The light is dispersed by bandpass interference filters and subsequently detected with a photomultiplier. At a wavelength of 335 nm the total detection efficiency is equal to $\eta_{\text{opt}} = 3.6 \cdot 10^{-3}$ [24], including the solid angle acceptance, the transmission of the lenses and the quantum efficiency of the photomultiplier. The transmission of the bandpass filters ranges typically from $T_{\text{filter}} = 0.2$ to 0.4, resulting in an overall efficiency $\approx 10^{-3}$ for the detection of all fluorescence photons in the various $\Delta v = v' - v''$ band.

At a distance $l_{sc} = 938$ mm upstream of the scattering center, the primary beam is chopped by a mechanical chopper in order to resolve the collision energy dependence of the product formation with the single-burst time-of-flight method. The velocity distribution in the primary beam is measured with a metastable atom detector (solid angle acceptance $\Omega_m = 2.49 \cdot 10^{-9}$ sr as determined by a separate collimator with a 0.1 mm diameter, Fig. 2). The detector consists of a stainless steel plate and an electron multiplier and is situated downstream of the scattering centre at a distance $l_{\text{TOF}} = 2139$ mm from the chopper wheel. To determine the absolute value of the Kr^* flux in the scattering center, we use the detector efficiency $\eta_m = 0.064$ as found by Theuws et al.[27]

Both the photomultiplier and the metastable atom detector are operated in pulse mode. A multichannel counting device, interfaced to a computer, accumulates the data.

2.2 Laser excitation

The $\text{Kr}^*(^3\text{P}_2) \leftrightarrow \text{Kr}^{**}(^3\text{D}_3)$ closed level transition at $\lambda = 811$ nm has a linewidth $\Gamma/2\pi \equiv \Delta\nu_a = 5.6$ MHz. For an ideal two-level system the fraction ^{exc}f of all atoms that is in the excited state equals

$$^{exc}f(s) = \frac{s}{2(1+s)} \quad (2)$$

with s the saturation parameter. For a linear polarization the stationary state distribution over the magnetic substates $|J = 3, m\rangle$ is $20/42$ ($m = 0$), $10/42$ ($m = \pm 1$), $1/42$ ($m = \pm 2$) and 0 ($m = \pm 3$) with respect to the polarization vector, which is aligned parallel to the primary beam velocity. At a collision energy $E = 100$ meV the angle between \mathbf{v}_1 and the relative velocity g is equal to ≈ 1 rad. This results in a near isotropic population distribution in the collision frame: 0.110 ($m = 0$), 0.116 ($m = \pm 1$), 0.195 ($m = \pm 2$) and 0.134 ($m = \pm 3$).

The shortlived Kr^{**} atoms are produced in the scattering center using a 100 mW SDL diode laser [28]. The linewidth of the laser is estimated at $\Delta\nu_l \approx 15$ MHz. It is

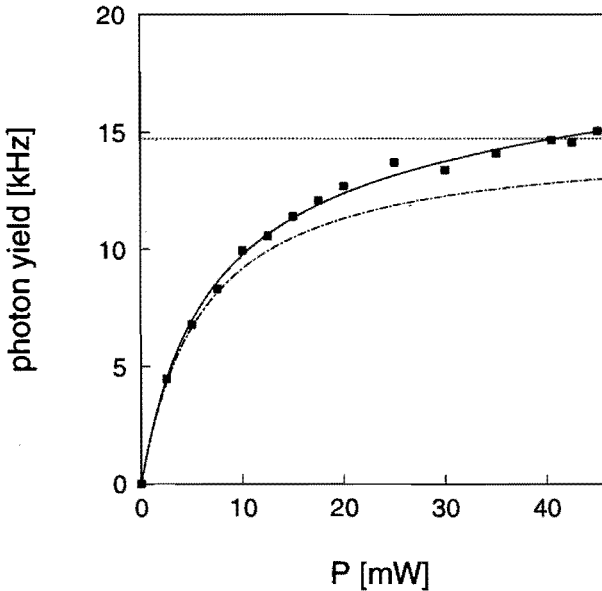


Figure 3: Saturation curve of the collision induced fluorescence signal, measured with the $\Delta\nu = -1$ filter. The solid line is the result of a least squares analysis with the model function of Eq. (3). The dash-dot line is the contribution of the ^{84}Kr isotope on which the laser frequency is tuned, with the dashed line indicating the saturation level for this contribution for $s \rightarrow \infty$. A laser power $P_{0,\text{expt}} = 6.05$ mW corresponds to $s = 1$. All cross section measurements have been performed at a power of $P = 40$ mW, *i.e.*, $s \approx 7$.

stabilized on the maximum of the absorption profile of a gas discharge, using a modulation width $\Delta\nu_{\text{lock-in}} = 10$ MHz. The calculated saturation intensity for excitation with a linearly polarized laser beam is $I_{0,\text{ideal}} = 24.5 \mu\text{Wmm}^{-2}$, assuming a stationary state distribution of the magnetic substates and a linewidth of the laser $\Delta\nu_l \ll \Gamma/2\pi$. This saturation intensity corresponds to an on-resonance saturation parameter $s = 1$. Taking into account the finite linewidth of the laser, the saturation intensity is increased by a factor $(\Delta\nu_l + \Delta\nu_a)/\Delta\nu_a \approx 3.7$, resulting in $I_{0,l} \approx 91 \mu\text{Wmm}^{-2}$.

The beam profile is determined by a rectangular collimator with dimensions of $A_l = (\Delta x \times \Delta z)_l = 6.0 \times 6.0 \text{ mm}^2$. The calculated laser power corresponding to a saturation parameter $s = 1$ thus is $P_{0,\text{ideal}} = A_l I_{0,\text{ideal}} = 3.26$ mW. The dimensions of the scattering center in the collision plain are $(\Delta x \times \Delta z)_{sc} = 7.7 \times 6.0 \text{ mm}^2$, *i.e.*, a fraction $6/7.7 = 0.78$ of the Kr^* beam is not illuminated by the laser beam. The effective solid angle thus is $\Omega'_{sc} = 14.6 \cdot 10^{-6}$ sr.

The fraction of Kr^* atoms in the atomic beam contributing to the excited-state density of Kr^{**} in the scattering center has been determined experimentally, using two

different methods. First, we have measured the saturation curve \dot{N}_{ph} of the collision induced fluorescence in the scattering center, which is a direct measure for the excited state population. The result is given in Fig. 3. The main contribution stems from the ^{84}Kr isotope on which the laser frequency is stabilized, with a relative abundance of $^{84}f = 0.57$. The extra population at high powers is due to the isotopes ^{82}Kr and ^{86}Kr (relative abundance $^{82}f = 0.116$ and $^{86}f = 0.173$, respectively) with isotopic shifts $\Delta\nu_{82} = -65$ MHz and 69 MHz, respectively, which are excited off-resonance with an effective saturation parameter $s' \approx s/20$.

The data in Fig. 3 have been analysed with the model function

$$\dot{N}_{ph}(P) = \dot{N}_{ph,sat} \left[{}^{84}f \frac{s}{2(1+s)} + ({}^{82}f + {}^{86}f) \frac{(s/20)}{2(1+(s/20))} \right] \quad (3)$$

with $s = P/P_{0,expt}$ and $P_{0,expt}$ the laser power corresponding to $s = 1$. A least squares analysis results in $P_{0,expt} = 6.05$ mW, which is in reasonable agreement with the calculated ideal value. At a power of 40 mW this results in a saturation parameter $s \approx 7$. The excited state population of the ^{82}Kr and ^{86}Kr isotopes is then equal to $^{exc}f(s' = 0.35) = 0.13$, as compared to $^{exc}f(s = 7) = 0.43$ for the ^{84}Kr isotope.

Second, we have measured the loss of Kr^* atoms which are deflected by the laser beam. With the combination of two collimators downstream of the scattering center, with diameters of 0.3 mm and 0.1 mm at positions 162 mm and 567 mm beyond the secondary beam, respectively, the transverse momentum transfer by the radiation pressure results in a loss of detected atoms. At a beam velocity $v_1 = 535$ m/s and a recoil velocity $v_{recoil} = 6 \cdot 10^{-3}$ m/s, the recoil of 44 photons is sufficient for atoms to be blocked by the second collimator. With a transit time of $t_{transit} = 11 \mu\text{s}$ through the laser beam, the maximum number of absorption/spontaneous emission cycles is of the order of 166 for $s = 7$ at $P = 40$ mW. The fractional loss curve of the atomic beam signal is shown in Fig. 4. The value for $P = 40$ mW is 0.46, in good agreement with the calculated product 0.47 of the population $^{84}f = 0.57$ for the ^{84}Kr isotope and a statistical fraction of $^2f = 5/6 = 0.83$ of metastable atoms in the $^3\text{P}_2$ state. The other isotopes are not excited often enough to be stopped by the second collimator, due to the much smaller value of s' .

The aperture in front of the scattering centre results in a small divergence $\Delta v_{\perp,FWHM} = v_1 \theta_{FWHM} = 6.6 \cdot 10^{-3} v_1$ of the atomic Kr^* beam. The corresponding Doppler width for the laser transition, $\Delta\nu_D = k \Delta v_{\perp,FWHM}$, is estimated at $\Delta\nu_D = 4.9$ MHz for $v_1 = 600 \text{ ms}^{-1}$. At high relative velocities, *i.e.*, at high values of v_1 , the excited state population will be slightly smaller due to larger Doppler width. However, these population changes are minor: on the order of a few percent. The data have not been corrected for this effect.

The cross section data have been analysed with the assumption that a fraction

$$**f = {}^2f [^{exc}f(s) {}^{84}f + ^{exc}f(s')({}^{82}f + {}^{86}f)] = 0.235 \quad (4)$$

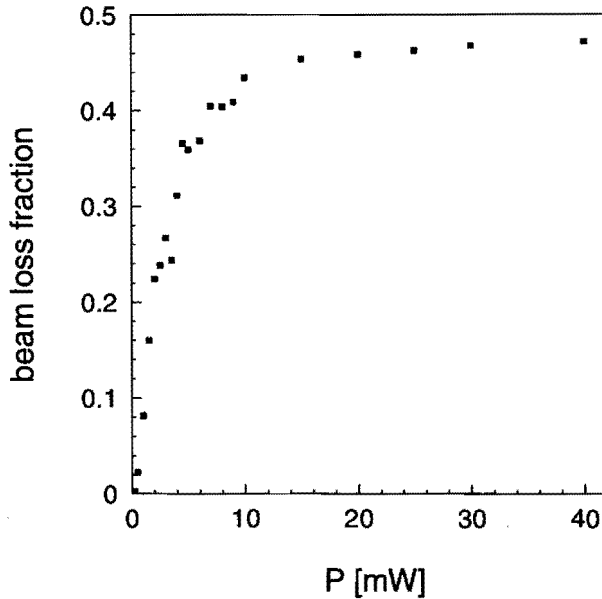


Figure 4: Fractional loss of beam atoms as a function of the laser power, due to the transverse momentum transfer by the laser excitation in the scattering center.

of the atomic beam of Kr^* atoms is in the excited Kr^{**} state in the scattering center.

3 Results and data analysis

Because the vibrational frequencies of the B and C states of N_2 differ only by a small amount, the transitions originating from different vibrational levels v' and terminating on vibrational levels $v'' = v' - \Delta v$, nearly coincide for a constant value of Δv . Because good spectral separation does exist between the Δv sequences, their integral intensities can be determined in a straightforward way using bandpass interference filters. The measured TOF spectra of the fluorescence photons and the metastable atoms (transformed to the position of the scattering center) are represented by $N_{ph,i}$ and $N_{m,i}$, respectively, with i the time channel index. The analysis to convert these spectra into absolute values of the effective cross sections $Q_{\Delta v}^{eff}$ is described by Van Vliembergen [23]. The result is

$$Q_{\Delta v}^{eff}(E_i) = \frac{1}{f} \frac{N_{ph,i}}{N_{m,i}} \frac{\eta_m}{\eta_{opt}} \frac{\Omega_m}{\Omega'_{sc}} \frac{Q_{el}}{1 - \exp[-(n_2 l) Q_{el} g_i / v_{1,i}]}, \quad (5)$$

with the parameters as defined in section 2. The transmission of the bandpass filters is not incorporated in the detection efficiency η_{opt} of the optical system; in the analysis

Table 1: Transmission $T_{\Delta v}^{v'}$ of the bandpass interference filters at the wavelength of the bandhead of the $v' \rightarrow v''$ transition. The error in the values given is estimated at $\Delta T = 0.005$.

v'	$\Delta v = -1$	$\Delta v = 0$	$\Delta v = 1$
0	0.420	0.210	
1	0.430	0.250	0.225

$Q_{\Delta v}^{eff}$ we have to take into account these transmission data. The relative velocity is $g = (v_1^2 + v_2^2)^{1/2}$. Both $v_2 = 790$ m/s and the density-length product $\langle n_2 l \rangle = 9.6 \cdot 10^{16}$ m⁻² of the secondary beam can be calculated accurately using the theory of supersonic expansions. For the integral elastic cross section Q_{el} excluding small angle scattering, we use a value $Q_{el} = 200 \text{ \AA}^2$. The effective cross section $Q_{\Delta v}^{eff}$ is rather insensitive to the exact value of Q_{el} .

The effective cross sections $Q_{\Delta v}^{eff}$ are linear combinations of the pure state inelastic cross sections $Q_{v'}$ for the excitation of the $N_2(C, v')$ vibrational states, as given by

$$Q_{\Delta v}^{eff} = \sum_{v' \geq \max(\Delta v, 0)} T_{\Delta v}^{v'} M_{v', v''} Q_{v'} \quad (6)$$

with $v'' = v' - \Delta v$. The coefficients $M_{v', v''}$ are the optical branching ratio's for the radiative decay $N_2(C, v') \rightarrow N_2(B, v'')$ (Eq. (1)), as calculated from the Einstein coefficients tabulated by Lofthus and Krupenie [29].

The parameter $T_{\Delta v}^{v'}$ is the transmission of the Δv -bandpass interference filter at the wavelength $\lambda(v', v'')$ corresponding to the $v' \rightarrow v''$ transition. The values for the filter transmission for $\Delta v = -1, 0$ and 1 have been carefully (re)calibrated for these experiments. The experimental results are listed in Table 1. The transmission for $\Delta v = 0$ and 1 differ from the values given by Vredenbregt et al. [24]; the transmission has decreased in time due to a deterioration of the filter coating, resulting in a white 'fog' on its surface.

Cross section measurements have been performed for filters with $\Delta v = -1, 0, 1$ and 2 . The results are shown in Fig. 5. The scatter of the data is due to the statistical accuracy in the TOF spectrum of the collision induced fluorescence. Because no significant signal for $Q_{\Delta v=2}^{eff}$ is detected (not shown in Fig. 5), we deduce that all cross sections $Q_{v'}$ for $v' \geq 2$ can be neglected in our analysis. For the $v' = 0$ and $v' = 1$ final states, only the $\Delta v = -1, 0$ and 1 effective cross sections $Q_{\Delta v}^{eff}$ are relevant. The final set of equations is then

$$\begin{aligned} Q_{\Delta v=-1}^{eff} &= 0.086 Q_{v'=1} + 0.136 Q_{v'=0} \\ Q_{\Delta v=0}^{eff} &= 0.0048 Q_{v'=1} + 0.107 Q_{v'=0} \\ Q_{\Delta v=1}^{eff} &= 0.113 Q_{v'=1}. \end{aligned} \quad (7)$$

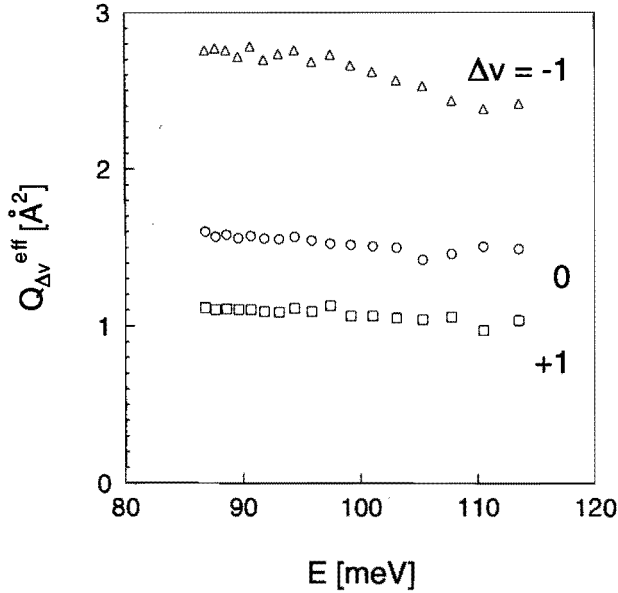


Figure 5: Experimental results for the absolute value of the effective cross sections $Q_{\Delta v}^{eff}$, as measured with the filters for $\Delta v = -1, 0$, and 1 as a function of the collision energy E .

Note that $Q_{\Delta v=0}^{eff}$ and $Q_{\Delta v=1}^{eff}$ closely relate to the pure state cross sections $Q_{v'=0}$ and $Q_{v'=1}$.

We solve the set of equations in Eq. (7) for the two parameters $Q_{v'=0}$ and $Q_{v'=1}$ using a least squares method. The results for $Q_{v'=0}$ and $Q_{v'=1}$ are shown in Fig. 6 as a function of the collision energy E . The error bars represent the uncertainty in the individual data points, as determined by the least squares method. The energy range is limited, due to the dominant influence of the velocity $v_2 = 790$ m/s of the N_2 secondary beam as compared to the range $440 < v_1(\text{m/s}) < 600$ of Kr velocities. We observe a slight decrease in cross section with increasing collision energy, similar for both $v' = 0$ and $v' = 1$, with a total decrease of the order of 10% from $E = 85$ meV to $E = 115$ meV.

4 Model analysis

The energy diagram of the collision process is given in Fig. 1. The initial kinetic energy $E \approx 100$ meV is indicated as well. At this energy both the $v' = 0$ and $v' = 1$ final vibrational states can be reached in an exothermic process; the $v' = 2$ state, with an endothermicity of 70 meV, is just accessible. Following Van Vliembergen et al. [23]

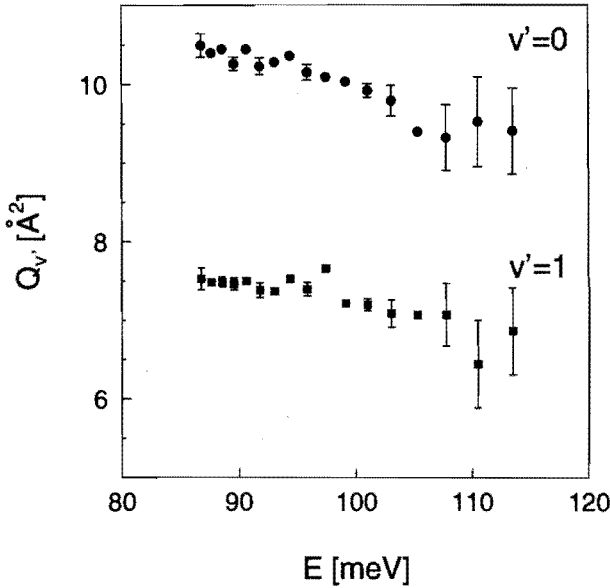


Figure 6: Experimental results for the absolute value of the pure final state cross sections $Q_{v'}$ for $v' = 0$ and $v' = 1$, as a function of the collision energy E .

the covalent $\text{Kr}^*(^3\text{P}_0, ^3\text{P}_2) + \text{N}_2$ potentials are represented by the $\text{Ne}^* + \text{Ar}$ potential of Gregor and Siska [30]; this type of potential gives a good description of elastic scattering data [18]. Only the rather flat, long range part of the covalent potentials is shown, as relevant for the curve crossings involved. A potential diagram including the repulsive branch can be found in the paper of Van Vliembergen et al. [23]. For the intermediate ionic state $\text{Kr}^+ + \text{N}_2^-$ a pure Coulomb curve is assumed.

For the $\text{Kr}^{**} + \text{N}_2$ system we can use the $\text{Ne}^{**} + \text{Ar}$ potential of Bussert et al. [31, 32] as a reference, with a well depth of $\epsilon \approx 40$ to 70 meV (depending on the specific Ω state, with Ω the absolute value of the magnetic quantum number of the total electronic angular momentum with respect to the internuclear axis) at an internuclear distance $R_m = 2.8 \text{ \AA}$. In view of these numbers, a *direct* crossing of the attractive branch of the initial potential with the lower lying final states is rather unlikely.

Therefore the starting point of our analysis is the intermediate state model, which has been successfully applied for understanding the excitation transfer cross sections for the Ar^* , $\text{Kr}^* + \text{N}_2$ systems [24]. In this model the ionic $\text{Ar}^+, \text{Kr}^* + \text{N}_2^-$ state serves as an intermediate with a curve crossing with both the initial and the final state potential. The crossing points R_x are assumed to be located at an internuclear distance where the covalent initial and final state potentials are still flat.

Each curve crossing is characterized by three parameters: the location of the cross-

ing R_x , the energy E_x of the crossing point with respect to asymptotic energy of the initial state $\text{Kr}^{**} + \text{N}_2$, and a reference velocity v_x . This characteristic velocity determines the probability p to pass a crossing diabatically according to the Landau Zener formula [33, 34]

$$p = \exp(-v_x/v_{\text{rad}}) \quad (8)$$

$$v_{\text{rad}} = \left\{ \frac{2}{\mu} [E - E_\phi - E_x] \right\}^{1/2} \quad (9)$$

$$E_\phi = E (b/R_x)^2, \quad (10)$$

with v_{rad} the radial velocity at the crossing point, b the impact parameter, μ the reduced mass and E_ϕ the centrifugal potential. The reference velocity is related to the diabatic coupling matrix element H_x and the difference in slopes $|\Delta F|_x$ of the intersecting diabatic potential curves as given by

$$v_x = \frac{2\pi H_x^2}{\hbar |\Delta F|_x}. \quad (11)$$

A net transition at a crossing occurs when it is passed once diabatically and once adiabatically, *i.e.*, $2p(1-p)$.

Looking at the data in Fig. 6, it is clear that it is impossible to determine all crossing parameters without any a priori information. On all of them, however, information is already available. To derive an estimate of the value of v_x , we investigate the behavior of the coupling matrix element H_x as a function of the internuclear distance R . We expect an exponential decrease of H_x as function of R [35],

$$H_x(R_x) \sim \exp(-\alpha R_x), \quad (12)$$

as determined by the overlap of the wave functions of the covalent and the ionic intermediate state. In Table 2 the value of $H_{x,i}$ for the initial state crossing of the $\text{Kr}^*(^3\text{P}_2)$ and $\text{Kr}^*(^3\text{P}_0) + \text{N}_2(\text{X})$ systems is given, calculated with the experimental value of $v_{x,i}$ of Vredendregt et al. [24] and the Coulomb potential estimate for $|\Delta F|_{x,\text{Coul}}$ as input. By extrapolation with Eq. (12) we find the value of H_x of the $\text{Kr}(^1\text{S}_0) + \text{N}_2(\text{C})$ and $\text{Kr}^{**}(^3\text{D}_3) + \text{N}_2$ curve crossings. Again by using the estimated value of $|\Delta F|_{x,\text{Coul}}$, we find the corresponding reference velocities v_x for the initial and final states of the process of Eq. (1). The results are given in Table 2.

The value of $E_{x,i}$ for the initial state is assumed to be equal to zero, *i.e.*, $E_{x,i} = 0$ meV; for the final state the value of $E_{x,f}$ is determined by the asymptotic exothermicity of the process, *i.e.*, $E_{x,f} = -410$ meV for $v' = 0$.

For the final state crossing radius $R_{x,f}$ of the $\text{Kr}^{**} + \text{N}_2$ system, we use the average value of the *final* state crossing radius $R_{x,f}(\text{N}_2(\text{C})) = 3.9 \text{ \AA}$ for the $\text{Kr}^*(^3\text{P}_{0,2}) + \text{N}_2(\text{X})$ systems (Table 3) as a starting point. The latter has been taken from the model analysis of the experimental results of Vredendregt et al. [24]. Taking into account

Table 2: Landau Zener coupling matrix elements for the crossing of the four covalent potential curves with the ionic intermediate state potential.

curve crossing	Coulomb potential		Experimental data	
	$R_{x,Coul}$ [Å]	$ \Delta F _{x,Coul}$ [eV/Å]	v_x [ms ⁻¹]	H_x [meV]
Kr*(³ P ₂) + N ₂ (X) ^a	2.5	2.4	7400	136
Kr*(³ P ₀) + N ₂ (X) ^a	2.8	1.9	2200	66
Kr(¹ S ₀) + N ₂ (C, $v' = 0$)	3.0	1.7	960 ^c	41 ^b
Kr**(³ D ₃) + N ₂ (X)	3.2	1.5	405 ^c	25 ^b

^a Vredendregt et al. [24]

^b Estimated by using Eq. (12) with $R_{x,Coul}$ as input.

^c Calculated with Eq. (11) and $|\Delta F|_{x,Coul}$ as input.

Table 3: Landau Zener parameters for the initial state crossings of the Kr* + N₂ and Kr** + N₂ systems and the final state Kr(¹S₀) + N₂(C, $v' = 0$) system with the ionic intermediate state potential, as determined from the experimental data in this paper and by Vredendregt et al.[24].

system	Initial state			Final state		
	$E_{x,i}$ [eV]	$R_{x,i}$ [Å]	$v_{x,i}$ [ms ⁻¹]	$E_{x,f}$ [eV]	$R_{x,f}$ [Å]	$v_{x,f}$ [ms ⁻¹]
Kr*(³ P ₂)+N ₂ (X)	0		7400	1.12	3.7	
Kr*(³ P ₀)+N ₂ (X)	0		2200	0.47	4.1	
Kr**(³ D ₃)+N ₂ (X)	0	4.2		-0.41		713

that the initial Kr** + N₂(X) state lies approximately 0.4 eV above the final Kr(¹S₀) + N₂(C) state, we estimate $R_{x,f} \approx 4.2\text{Å}$ based on the R^{-1} dependence of the ionic intermediate potential.

Using the estimated values of v_x for the initial and final state, a simple model of the reaction dynamics of the Kr** + N₂ system emerges (Fig. 7). For the initial state crossing with the ionic curve, the maximum value of the radial energy is $E_{rad,i} = E \approx 100$ meV, corresponding to an initial asymptotic collision velocity $v_i = 958$ m/s. With increasing impact parameter the radial velocity decreases below this value, with $v_{rad,i} = 0$ for $b = R_{x,i}$. The condition $v_{rad,i} \approx v_{x,i}$ thus holds, with approximately equal chances for a diabatic or an adiabatic passage.

At the final state curve crossing the situation is different: a diabatic passage is strongly preferred. For a transition to the final state to occur, an adiabatic passage is required, either on the way in or on the way out (Fig. 7). The cross section Q_f for reaching the final state is in good approximation given by

$$Q_f = \pi R_x^2 2p_f(1 - p_f) \left[\frac{(1 - p_i)}{(1 - \epsilon)} \right], \quad (13)$$

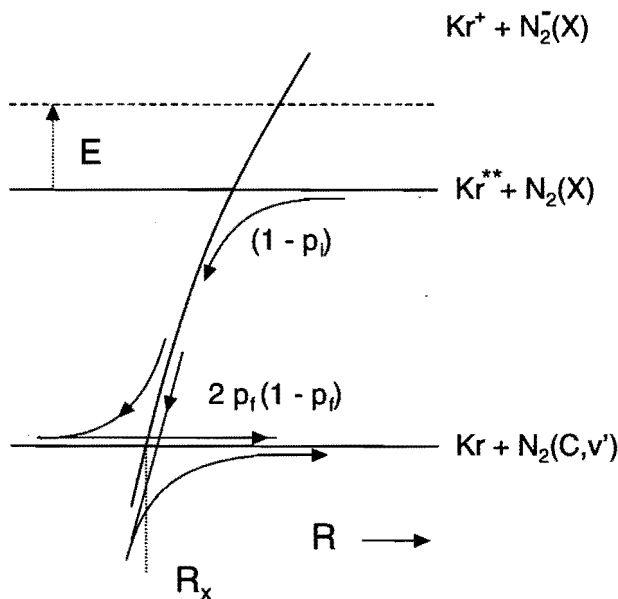


Figure 7: Schematic view of the reaction path of the $\text{Kr}^{**} + \text{N}_2$ system on the initial and final state potentials for an inelastic collision. A single final state potential has been assumed.

$$\epsilon = p_i[1 - p_f(1 - p_f)],$$

with p_i and p_f the effective probability for a diabatic passage of the initial and final state curve crossing, respectively. The factor $(1 + \epsilon + \epsilon^2 + \dots) = (1 - \epsilon)^{-1}$ corrects for the flux that stays on the ionic curve for an increasing number of passages. This flux is reflected back and forth through the curve crossing grid because the ion-pair has insufficient energy to dissociate.

For the initial state crossing both the adiabatic crossing probability $(1 - p_i)$ and the recycling probability $(1 - \epsilon)^{-1}$ do depend strongly on the impact parameter b of the initial trajectory. Their product, however, varies from a value of 0.7 for $b = 0$ to 0.86 for $b = 0.9 R_{x,i}$, calculated with the estimated values of v_x given in Table 2. For the evaluation of Eq. (13) we use a fixed value of 0.77 for this product, corresponding to $b = R_{x,i}/2^{1/2}$.

The radial velocity $v_{\text{rad},f}$ at the final state crossing, and thus the probability p_f , only depends slightly on the impact parameter. An initial trajectory with $b \leq R_{x,i}$ will reach the final state crossing with only a small centrifugal energy $E_{\phi,f} = E(b/R_{x,f})^2 \leq E(R_{x,i}/R_{x,f})^2 = 1.2 E \ll E - E_{x,f}$, resulting in a radial energy at the final state crossing in the range $(-E_{x,f} - 0.2 E) \leq E_{\text{rad}} \leq (-E_{x,f} + E)$. We thus approximate p_f

by the value for $b = 0$.

Inserting the value $Q_{f,expt} = Q_{v'=0} + Q_{v'=1} = 17.2\text{\AA}^2$ and using $R_{x,i} = 4.2\text{\AA}$ from Table 3, we solve Eq. (13) for p_f ; the resulting reference velocity is $v_{x,f} = 713$ m/s. This value for $v_{x,i}$ is consistent with the previous estimate $v_{x,f} \approx 960$ m/s, based on the $H_x(R)$ behavior (Table 2).

This result for Q_f has been checked by performing the full integration over the impact parameter, as described by Vredenbregt et al. [24]. Using $v_{x,i} = 405$ m/s as input, we find $v_{x,f} = 750$ m/s. The previous discussion, however, gives more insight in the collision process than the “black box” calculation.

This approach does not explain the branching of the cross section over the vibrational states $v' = 0$ and 1. To reach the $v' = 0$ final state we have to cross both the $v' = 1$ and $v' = 0$ levels diabatically, with an adiabatic passage on the way out. The Landau Zener probability to reach the $v' = 0$ final state is then proportional to p_f^2 , resulting in a cross section that is always smaller than the $v' = 1$ cross section, in contradiction with the experimental evidence. This same discrepancy has also been reported for the transfer of excitation for the systems $\text{Ar}^*, \text{Kr}^* + \text{N}_2$. Clearly, a model approach assuming separated crossings for the two final states ($v'=0,1$) is not valid for these systems.

The branching of the cross section over the $v' = 0$ and 1 vibrational states can alternatively be interpreted in terms of Franck Condon factors $F_{v'}$ for the transition of the $\text{N}_2(\text{X}, v = 0)$ ground state to the $\text{N}_2(\text{C}, v')$ excited state, taking into account their modification due to the bond stretching of the N_2^- intermediate state [36, 37]. The final expression for the excitation transfer cross section then is given by

$$Q_{v'} = F_{v'} Q_f, \quad (14)$$

with Q_f given by Eq. (13). For the $\text{Kr}^{**} + \text{N}_2$ we find

$$Q_{v'=0}/Q_{v'=1} = 1.4, \quad (15)$$

a much smaller value than found experimentally for the $\text{Kr}^*(^3\text{P}_2, ^3\text{P}_0) + \text{N}_2$ systems, with $Q_{v'=0}/Q_{v'=1} \approx 3$ [24].

5 Concluding remarks

For the $\text{Ar}^* + \text{N}_2$ system the ionic intermediate state is essential for explaining the observed velocity dependence of the excitation transfer cross sections. A direct coupling predicts results that are in stark contrast with the experimental evidence, as discussed by Vredenbregt et al. [24].

For the $\text{Kr}^* + \text{N}_2$ Vredenbregt et al. [24] observe an excitation cross section with a strong threshold effect, leveling off to a value of the order of $Q_{tot} \approx 10\text{\AA}^2$ at an energy

$(E' - E_{x,f}) \approx 0.5$ eV. We refer to Fig. 1 for our discussion. For a transition to the final state, a diabatic passage of the initial state crossing is required, either on the way in or on the way out. Because the radial kinetic energy is large, $E' \approx 1.2$ eV for the $\text{Kr}^*(^3\text{P}_2)$ state, the corresponding radial velocity $v_{\text{rad},i} \approx 3500$ m/s is well matched to the characteristic velocity $v_{x,i} = 7400$ m/s of the initial state crossing. The Landau Zener probability is on the order of $2p_i(1 - p_i) \approx 0.25$.

At the final state curve crossing, on the other hand, the large value of the centrifugal energy $E_{\phi,f} = E'(b/R)^2$ will result in very low values of the radial energy $E_{\text{rad},f} = (E' - E_{x,f}) - E_{\phi,f}$. Even for the low value $v_{x,f} \approx 900$ m/s of this final state crossing, as we have learned in this paper, the adiabatic passage will be favored for the largest impact parameters $b \leq b_{\text{max}}$ that can still reach this crossing. This assumption, as made by Vredendregt et al. [24] in the analysis of the experimental results, is still fully justified.

As reported by Vredendregt et al. [24], for the $\text{Kr}^*(^3\text{P}_0, ^3\text{P}_2) + \text{N}_2$ systems there is no obvious preference for the direct or intermediate model: the data are equally well described by a suitable curve fit. This is due to the limited information present in the experimental cross sections, both because the collision energy is never far from threshold and because the contributions for $\text{Kr}^*(^3\text{P}_0)$ and $\text{Kr}^*(^3\text{P}_2)$ overlap.

We have shown that the intermediate state model gives a very satisfactory description of the observed cross section magnitude for the $\text{Kr}^{**} + \text{N}_2$ system. The results for the crossing parameters are consistent with the values of the intermediate state model for the $\text{Kr}^*(^3\text{P}_0, ^3\text{P}_2) + \text{N}_2$ systems, as derived by Vredendregt et al. [24] from his experimental data. However, we still do not have a decisive answer on the uniqueness of the model used.

Acknowledgements

The authors would like to thank E.J.D. Vredendregt for many helpful discussions while writing the final paper.

References

- [1] D. Hennecart, Ph.D. thesis, Université de Caen, France, (1982).
- [2] D. Hennecart and F. Masnou-Seeuws, *J. Phys. B* **18**, 657 (1985).
- [3] M. Manders, J. Driessen, H. Beijerinck, and B. Verhaar, *Phys. Rev. Lett.* **57**, 2427 (1986).
- [4] M. Manders, W. van Hoek, G. S. E.J.D. Vredendregt, H. Beijerinck, and B. Verhaar, *Phys. Rev. A* **39**, 4467 (1989).

-
- [5] W. Boom, S. OpdeBeek, R. van Galen, F. Huijsmans, H. Beijerinck, and B. Verhaar, *Phys. Rev. A* **49**, 4660 (1994).
- [6] V. Aquilanti, R. Candori, F. Pirani, T. Krümpelmann, and C. Ottinger, *Chem. Phys.* **142**, 47 (1990).
- [7] T. Krümpelmann and C. Ottinger, *Chem. Phys.* **140**, 142 (1987).
- [8] T. Krümpelmann, C. Nyeland, and C. Ottinger, in *Book of Abstracts*, edited by J. Geddes, H. Gilbody, A. Kingston, C. Latimer, and H. Walters (North Holland, Amsterdam, 1988), p. 695.
- [9] T. Aardema, E. van Nijnatten, and H. Beijerinck, *Chem. Phys.* **184**, 273 (1994).
- [10] F. Tuffin, A. le Nadan, and J. Peresse, *J. Phys (Paris)* **46**, 181 (1985).
- [11] Y. Harada, K. Ohno, and H. Mutoh, *J. Chem. Phys.* **79**, 3251 (1983).
- [12] H. Hotop, J. Lorenzen, and A. Zastrow, *J. Electron Spectry.* **23**, 347 (1981).
- [13] A. Niehaus, in *Advances in Chemical Physics, Vol.45*, edited by J. McGowan (Wiley, New York, 1982), p. 399.
- [14] J. Kroon, A. Cottaar, and H. Beijerinck, *Chem. Phys.* **103**, 119 (1986).
- [15] M. Verheijen and H. Beijerinck, *Chem. Phys.* **102**, 255 (1986).
- [16] L. Appoloni, B. Brunetti, F. Vecchiocattivi, and G. Volpi, *J. Phys. Chem.* **92**, 918 (1988).
- [17] F. van de Berg, J. Schonenberg, and H. Beijerinck, *Chem. Phys.* **115**, 359 (1987).
- [18] R. van Gerwen, E. Vredenburg, E. Kerstel, and H. Beijerinck, *Chem. Phys.* **118**, 407 (1987).
- [19] D. Winicur and J. Fraites, *J. Chem. Phys.* **61**, 1584 (1974).
- [20] E. Kerstel, M. Janssens, K. van Leeuwen, and H. Beijerinck, *Chem. Phys.* **121**, 211 (1988).
- [21] K. Tabayashi and K. Shobatake, *J. Chem. Phys.* **84**, 4919 (1986).
- [22] L.-Y. C. Chiu, T. Krümpelmann, and C. Ottinger, *Chem. Phys. Letters* **151**, 220 (1988).
- [23] E. van Vliembergen, E. Vredenburg, G. Kaashoek, J. Jaspar, M. van Lanen, M. Janssens, M. Verheijen, and H. Beijerinck, *Chem. Phys.* **114**, 117 (1987).

-
- [24] E. Vredenburg, W. Boom, R. van Gerwen, and H. Beijerinck, *Chem. Phys.* **145**, 267 (1990).
- [25] See references cited by Vredenburg et. al, *Chem. Phys.* **145**, 267 (1990).
- [26] H. Beijerinck and N. Verster, *Physica C* **111**, 327 (1981).
- [27] P. Theuws, H. Beijerinck, N. Verster, and D. Schram, *J. Phys. E* **15**, 573 (1982).
- [28] Spectra Diode Labs, type SDL-5410-C.
- [29] A. Lofthus and P. Krupenie, *J. Phys. Chem. Ref. Data.* **6**, 226 (1977).
- [30] R. Gregor and P. Siska, *Chem. Phys.* **74**, 1078 (1981).
- [31] W. Bussert, T. Bregel, R. Allan, M. Ruf, and H. Hotop, *Z. Phys. A* **320**, 105 (1985).
- [32] W. Bussert, T. Bregel, J. Ganz, K. Harth, A. Siegel, M. Ruf, H. Hotop, and H. Morgner, *J. Phys. (Paris) Colloq.* **C1 199**, 199 (1985).
- [33] E. Nikitin, in *Chemische Elementar Prozesse*, edited by H. Hartmann and J. Heidelberg (Springer Verlag, Berlin, 1968).
- [34] E. Nikitin and S. Umanskii, *Theory of Slow Atomic Collisions* (Springer, Berlin, 1984).
- [35] R. Olson, F. Smith, and E. Bauer, *Appl. Optics* **10**, 1848 (1971).
- [36] E. Gislason, A. Kleyn, and J. Los, *Chem. Phys.* **67**, 252 (1979).
- [37] E. Gislason, A. Kleyn, and J. Los, *Chem. Phys.* **59**, 91 (1981).

Summary

This thesis mainly deals with a novel technique to slow an atomic beam by using monochromatic isotropic light. The remainder concerns inelastic collisions of electronically excited atoms, resulting in electronic and rovibronic excitation of the target molecule.

For slowing a beam of atoms several laser cooling techniques are available. A new and promising technique is slowing by isotropic, monochromatic radiation, detuned to the red side of the atomic transition. The Doppler effect of the atom is compensated for by the angle between the atomic beam axis and the incident photons.

To investigate this technique, we use an optical cavity made of Spectralon to create an isotropic radiation field. The material Spectralon has a high reflectance $\mathcal{R} \approx 0.99$ and behaves as an ideal isotropic reflector. Therefore, low input powers can be used to create intense light fields. Disadvantages, however, are that the reflectance \mathcal{R} strongly depends on the cavity geometry and that it can be downgraded by contamination of the material itself. Small changes in the reflectance do not only cause large changes in the absolute light intensity, but will also modify the distribution of the light in the cavity. Consequently, the efficiency of slowing can be strongly influenced by these effects. Taking the ideal reflectance value as a basis, we have calculated the slowing effect by numerical Monte-Carlo simulations. Simultaneously, we have investigated the slowing process experimentally.

In a time-of-flight apparatus consisting of a 1D position-resolving detector, both the axial deceleration and the transverse diffusion of a cold beam of metastable neon atoms have been determined. Two cavity geometries have been used: a cylindrical and a spherical cavity with an interaction length on the order of 50 mm. A typical power input is 10 to 30 mW. The axial deceleration results in a peak of slow atoms at the resonance velocity, $v_s = -\delta/k$, as determined by the negative detuning δ of the laser frequency. The number of atoms captured in this peak is determined by the capture range, *i.e.* the maximum deceleration which has been realized.

Transverse diffusion, *i.e.* an increase in velocity spread perpendicular to the beam axis, results in an increase in beam divergence and thus in a loss of beam quality. Diffusion due to spontaneous emission is the price we have to pay for axial slowing and cannot be avoided. The extra contribution due to absorption-stimulated emission cycles is characteristic for isotropic slowing and should be minimized. For large saturation parameters this effect becomes significant. In the case of a cylindrical cavity, the peaked structure of the intensity distribution automatically induces a relatively large contribution of stimulated emission to the transverse diffusion. In contrast, the spherical cavity with a flat intensity distribution is less affected.

Both cavities have been investigated experimentally. Within the capture range no differences have been observed, whereas for larger velocities a better performance of the spherical cavity has been realized. As is shown, the best approach to minimize the transverse diffusion and maximize the capture range is to increase the length of the cavity and to distribute the power as evenly as possible.

A Monte Carlo method is used to calculate the intensity distribution in the optical cavity and to simulate the slowing process. From these calculations, more insight can be gained into this technique. Comparison with the experimental results shows that the calculations overestimate the slowing effect and, consequently, the transverse diffusion. The non-ideal behavior of Spectralon is the most likely explanation for this effect.

Although there is slight difference between model and experiment, calculations have shown that the technique of isotropic light slowing can be applied successfully as a 'post-Zeeman' slower for atoms in the Kelvin range of energies. For initial velocities near $v=100 \text{ ms}^{-1}$ for Ne^* , as observed at the exit of a Zeeman slower, isotropic slowing is very efficient. Finally, the possibility of the compression of a velocity distribution in the Kelvin range, *i.e.* laser cooling, is demonstrated.

The second part of this thesis concerns inelastic collisions of electrically excited rare gas atoms in metastable $\text{Xe}^*(6s;^3P_2)$ and shortlived $\text{Kr}^{**}(5p;^3D_3)$ states, with ground state $\text{N}_2(\text{X}, v=0)$ molecules as a target. The final state is a ground state rare gas atom and an excited N_2 molecule in a specific electronic (B or C) and vibrational state v' . These processes have been investigated by measuring the collision energy dependence of the vibrationally resolved total cross section for the final state production in a broad range of thermal and superthermal collision energies, using a crossed beam apparatus based on the time-of-flight technique.

The $\text{Xe}^*(6s;^3P_2)+\text{N}_2(\text{X})$ system is an example of a direct crossing between the initial and final state potentials, with a highly selective character for the final state. The experimental results imply the possible existence of even a double crossing for the endothermic $\text{Xe}(^1S_0)+\text{N}_2(\text{B}, v'=5)$ final state. At higher collision energies the lower lying vibrational states $v' \leq 4$ are accessible through crossings in the repulsive branch of the potential, resulting in a loss of flux in the resonant channel $v'=5$. An analysis of the experiments with a Landau-Zener model indicates that the initial state potential is more repulsive for large internuclear distances than predicted by model potential calculations.

Finally, thermal energy collisions of laser-excited $\text{Kr}^{**}(5p;^3D_3)$ atoms with $\text{N}_2(\text{X})$ are reported. In this experiment the photon energy of 1.5 eV serves as additional potential energy compared to the metastable $\text{Kr}^*(5s;^3P_2)$ state. The observed final states are the $v'=0$ and $v'=1$ vibrational levels of the $\text{N}_2(\text{C}, v')$ state. The strongly endothermic process for $\text{Kr}^*(5s;^3P_2)$, with a threshold energy of 1.1 eV, is now visible as an exothermic process for collisions with $\text{Kr}^{**}(5p;^3D_3)$. This allows us to investigate the influence of both potential and kinetic energy as a mediator for reaching the exit channels. The experiments, again analyzed with a Landau-Zener model, provide strong evidence for the role of the ionic $\text{Kr}^+ + \text{N}_2^-$ intermediate state potential for the coupling of the initial and final state. The parameters derived from this model analysis are fully consistent with the previous data for the metastable atom collisions.

Samenvatting

Dit proefschrift behandelt hoofdzakelijk een nieuwe techniek om atomen af te remmen in een monochromatisch isotroop lichtveld. Verder wordt ingegaan op inelastische botsingen van elektronisch geëxciteerde atomen, welke resulteren in elektronische en rovbationele excitatie van de molecuul-botsingspartner.

Om een atoombundel af te remmen zijn verschillende laserkoel-technieken beschikbaar. Een vrij nieuwe en veelbelovende techniek is het afremmen door middel van monochromatisch isotroop licht, welk rood verstemd is ten opzichte van de atomaire overgang. Het Doppler-effect van de atoom wordt gecompenseerd door de hoek tussen de atomaire bundelas en de inkomende fotonen.

Teneinde deze techniek te bestuderen, wordt een optische trilhaute van Spectralon gebruikt om een isotroop lichtveld te creëren. Spectralon heeft een hoge reflectiviteit $\mathcal{R} \approx 0.99$ en gedraagt zich als een ideale isotrope reflector. Hierdoor kunnen lage laser- vermogens worden gebruikt om intense lichtvelden te creëren. Een nadeel is echter dat de reflectiviteit \mathcal{R} sterk afhangt van de gebruikte geometrie van de optische trilhaute en dat deze aanzienlijk verminderd kan worden door vervuiling van het materiaal zelf. Door een kleine verandering in de reflectiviteit, verandert niet alleen de absolute lichtintensiteit, maar ook de intensiteitsverdeling in de trilhaute. Dit zal de efficiency van het afremmen sterk beïnvloeden. Uitgaande van de ideale reflectiviteitswaarde, wordt de afremming berekend met behulp van numerieke Monte-Carlo simulaties. Tegelijkertijd wordt het afremmingsproces experimenteel onderzocht.

In een 'time-of-flight' opstelling bestaande uit een 1-dimensionale plaatsgevoelige detector, zijn de afremmingen bestudeerd voor de axiale en loodrechte richting ten opzichte van een koude bundel van metastabiele neon atomen. Twee trilhaute-geometrieën zijn gebruikt, namelijk een cilindrische en een sferische met een interactielengte in de orde van 50 mm. Een karakteristiek inkoppelvermogen in dit verband is 10 tot 30 mW. De axiale vertraging resulteert in een piek van langzame atomen met een resonantiesnelheid, $v_s = -\delta/k$, die wordt bepaald door de negatieve verstemming δ , van de laserfrequentie. Het aantal ingevangen atomen in deze piek is afhankelijk van de 'capture range', die wordt gedefinieerd als de maximaal realiseerbare vertraging.

Transversale diffusie, te definiëren als een toename van de loodrechte snelheids-spreiding ten opzichte van de bundelas, resulteert in een grotere bundeldivergentie en dus in een verminderde bundelkwaliteit. Diffusie ten gevolge van spontane emissie is de prijs die betaald moet worden voor axiaal afremmen en kan niet worden vermeden. De bijdrage in transversale diffusie door absorptie-gestimuleerde emissie cycli is kenmerkend voor isotroop afremmen en moet worden geminimaliseerd. Voor grote verzadigingsparameters wordt dit effect nog sterker. Bij de cilindrische trilhaute resulteert de gepiekte intensiteitsverdeling automatisch in een relatief grote bijdrage van absorptie-gestimuleerde emissie in de transversale diffusie. Bij de vlakke verdeling van

de sferische trilhaolte is er echter nauwelijks sprake van enig effect.

Beide trilhaolten zijn experimenteel bestudeerd. Terwijl binnen de capture range geen verschillen zijn waargenomen, is er voor grotere snelheden een verbetering gerealiseerd in het afremeffect voor de sferische trilhaolte. Zoals aangetoond is de beste aanpak om de transversale diffusie te minimaliseren en de capture range te maximaliseren, de lengte van de trilhaolte te vergroten en het vermogen zo gelijkmatig mogelijk te verdelen.

Ter berekening van de intensiteitsverdeling in de optische trilhaolte en om het afremproces te simuleren is een Monte Carlo methode gebruikt. Met deze berekening kan meer inzicht worden verkregen in de hierboven beschreven techniek. Vergelijking met de experimentele resultaten toont aan dat het afremeffect, en dus ook de transversale diffusie, wordt overschat in de berekeningen. Dit kan waarschijnlijk worden verklaard uit het feit dat het gedrag van Spectralon niet optimaal is.

Ondanks het kleine verschil tussen theorie en experiment, hebben berekeningen aangetoond dat deze techniek met succes kan worden toegepast als een 'Post-Zeeman slower'. Voor beginsnelheden rond $v=100 \text{ ms}^{-1}$, zoals waargenomen bij de uitgang van een 'Zeeman slower', is de techniek zeer efficiënt. Tot slot is de mogelijkheid aangetoond om de snelheidsverdeling te comprimeren in het Kelvin-gebied (laserkoelen).

Het tweede deel van dit proefschrift betreft inelastische botsingen van elektronisch geëxciteerde edelgasatomen in metastabiele $\text{Xe}^*(6s;^3\text{P}_2)$ en kortlevende $\text{Kr}^{**}(5p;^3\text{D}_3)$ toestanden met grondtoestand $\text{N}_2(\text{X}, v=0)$ moleculen als doelwit. De eindtoestand is een grondtoestand-edelgasatoom en een geëxciteerd N_2 molecuul in een specifiek elektronische (B of C) en vibrationele toestand v' . Deze processen zijn bestudeerd door de botsingsenergie-afhankelijkheid te meten van de vibrationeel opgeloste totale werkzame doorsnede van de eindtoestand. Dit is gemeten in een breed thermisch en superthermisch botsingsenergiegebied, waarbij gebruik is gemaakt van een bundelmachine gebaseerd op de 'time-of-flight' techniek.

Het $\text{Xe}^*(6s;^3\text{P}_2)+\text{N}_2(\text{X})$ systeem is een voorbeeld van een directe kruising tussen potentialen van in- en uitgangstoestand, met een hoog selectief karakter voor de eindtoestand. De experimentele resultaten impliceren het mogelijke bestaan van een dubbele potentiaalkruising voor de endothermische $\text{Xe}(^1\text{S}_0)+\text{N}_2(\text{B}, v'=5)$ eindtoestand. Bij hogere botsingsenergieën worden de lager gelegen vibrationele toestanden $v' \leq 4$ toegankelijk door kruisingen in de repulsieve potentiaalvlak. Dit resulteert in een fluxverlies in het resonante $v' = 5$ kanaal. Analyse van de experimenten met het Landau-Zener model toont aan dat voor grotere internucleaire afstanden de ingangspotentiaal repulsiever is dan voorspeld door model potentiaal-berekeningen.

Tenslotte worden thermische energie-botsingen van laser-geëxciteerde $\text{Kr}^{**}(5p;^3\text{D}_3)$ atomen met $\text{N}_2(\text{X})$ gepresenteerd. In het experiment dient de foton-energie van 1.5 eV als extra potentiële energie vergeleken met de metastabiele $\text{Kr}^*(5s;^3\text{P}_2)$ toestand. De waargenomen eindtoestanden zijn de $v' = 0$ en $v' = 1$ vibrationele niveaus van de

$N_2(C, v')$ toestand. Het sterk endothermische proces voor $Kr^*(5s; ^3P_2)$ met een drempelenergie van 1.1 eV is nu zichtbaar als een exotherm proces voor botsingen met $Kr^{**}(5p; ^3D_3)$. Dit stelt ons in staat om de invloed te bestuderen van zowel de potentiële als de kinetische energie als middel om de uitgangskanalen te bereiken. De experimenten, welke opnieuw zijn bestudeerd aan de hand van het Landau-Zener model, leveren een sterke aanwijzing voor de bijdrage van de ionogene $Kr^+ + N_2^-$ tussentoestandspotentialaam aan de koppeling van de begin- en eindtoestand. De parameters afgeleid van deze model-analyse, stemmen volledig overeen met eerdere data over metastabiele atoombotsingen.

Dankwoord

Tot slot wil ik iedereen bedanken voor zijn of haar bijdrage aan het tot stand komen van dit proefschrift. Een aantal van hen wil ik in het bijzonder vermelden.

In de eerste plaats wil ik mijn promotor Herman Beijerinck bedanken voor zijn inzet. Daarnaast wil ik mijn copromotor, Jan Driessen, noemen die gedurende de afgelopen vier jaar een zeer gewaardeerd aanspreekpunt werd.

Verder wil ik de afstudeerders Erika van Nijnatten, Roel Knops, Sander Peters, Collin van Asten en Roel Vanneer alsmede de stagiair Sjoerd Nijsten hartelijk bedanken voor hun bijdrage. Hun prestaties en enthousiasme heb ik als zeer positief ervaren.

Natuurlijk wil ik ook mijn dank uitspreken voor de technische ondersteuning van Louis van Moll en Rien de Koning. De discussies met hen en hun praktische oplossingen waren zeer leerzaam.

Tenslotte wil ik Inge, familie en vrienden hartelijk bedanken voor hun steun gedurende de afgelopen vier jaar. Zonder jullie was dit alles niet mogelijk geweest.

Curriculum vitae

19 maart 1966	geboren te Eindhoven
1978 - 1983	eindexamen HAVO, Eindhovens Protestants Lyceum.
1983 - 1985	eindexamen Atheneum-B, Eindhovens Protestants Lyceum.
1985 - 1991	Studie Technische Natuurkunde Technische Universiteit Eindhoven.
1991 - 1995	Onderzoeker in Opleiding bij de Stichting FOM, werkgroep AQ-E, Atomaire en Optische Wisselwerkingen, Technische Universiteit Eindhoven.

STELLINGEN

behorende bij het proefschrift

Laser Manipulation of Metastable Neon by Isotropic Light

1. Afremming van een atoombundel in een isotroop lichtveld is het meest geschikt voor translatie-energieën in het bereik van 0.1-10 Kelvin.

Dit proefschrift, hoofdstuk II

2. Gestimuleerde emissie speelt, anders dan in een gericht lichtveld, een belangrijke rol in een isotroop lichtveld bij de ruimtelijke opblazing van een atoombundel.

Dit proefschrift, hoofdstuk III

3. Voor het meten van een flowcurve van een vloeistof met een sterk pseudoplastisch gedrag is een apparaat gebaseerd op een kegel-plaatgeometrie te verkiezen boven een Couette-geometrie.

H.T.M. van den Ende en A.M. van der Vorst, persoonlijk onderhoud

4. Loslopende fotonen bestaan niet.

K.A.H. van Leeuwen, persoonlijk onderhoud

5. De fase-verandering van een coherente superpositie van atomaire toestanden, zoals die optreedt tijdens een botsingsproces van geëxciteerde atomen, heeft in een retardatie-plaat zijn optisch analoog.

J.P.J. Driessen en S.S. Op de Beek, persoonlijk onderhoud

6. Gebruik van het Engels als voertaal op wetenschappelijke vergaderingen met in meerderheid Nederlandse deelnemers, zoals de najaarsvergadering van de sectie AQ van de Nederlandse Natuurkundige Vereniging, bevordert de verwording van de Engelse taal tot Nederlands dialect.

7. Het overhevelen van produktiecapaciteit van rijke landen naar lage-lonen landen onder menswaardige en milieuvriendelijke voorwaarden - is een uitstekende vorm van ontwikkelingshulp.

8. De viering van de nationale bevrijdingsdag op 5 mei heeft alleen zin als daarbij gekeken wordt naar de genocides van onze tijd.
9. De popularisering van de term 'broeikas-effect', waarmee een autonoom proces wordt gesuggereerd, verhult de nadelige invloed van direct menselijk handelen op de natuurlijke omgeving.